Search for direct scalar top pair production in final states with two tau leptons in pp collisions at $\sqrt{s} = 8$ TeV with the ATLAS Detector at the Large Hadron Collider

by

Ewan Chin Hill
B.Sc., University of Waterloo, 2008
M.Sc., University of Victoria, 2011

A Dissertation Submitted in Partial Fulfillment of the
Requirements for the Degree of

DOCTOR OF PHILOSOPHY

in the Department of Physics and Astronomy

Search for direct scalar top pair production in final states with two tau leptons in pp collisions at $\sqrt{s} = 8$ TeV with the ATLAS Detector at the Large Hadron Collider

by

Ewan Chin Hill
B.Sc., University of Waterloo, 2008
M.Sc., University of Victoria, 2011

Supervisory Committee

Dr. Isabel Trigger, Co-Supervisor
(Department of Physics and Astronomy & TRIUMF)

Dr. Robert Kowalewski, Co-Supervisor
(Department of Physics and Astronomy)

Dr. Randall Sobie, Departmental Member
(Department of Physics and Astronomy)

Dr. Adam Monahan, Outside Member
(School of Earth and Ocean Sciences)

Supervisory Committee

Dr. Isabel Trigger, Co-Supervisor
(Department of Physics and Astronomy & TRIUMF)

Dr. Robert Kowalewski, Co-Supervisor
(Department of Physics and Astronomy)

Dr. Randall Sobie, Departmental Member
(Department of Physics and Astronomy)

Dr. Adam Monahan, Outside Member
(School of Earth and Ocean Sciences)

ABSTRACT

The ATLAS Experiment at the CERN Large Hadron Collider is a particle physics experiment to study fundamental particles and their interactions at very high energies. Supersymmetry is a theory of new physics beyond the Standard Model of particle physics. A search for directly produced pairs of the supersymmetric partner of the top quark was performed using 20 fb^{-1} of proton–proton collision data at a centre of mass energy of 8 TeV taken in 2012. The search targeted a model where the supersymmetric partner of the top quark ("scalar top") decays via the supersymmetric partner of the tau lepton ("scalar tau") into the supersymmetric partner of the graviton ("gravitino"). Scalar top candidates were searched for in pp collision events with either two hadronically decaying taus, two light leptons (electrons or muons), or one hadronically decaying tau and one light lepton. The numbers of events passing the analysis selection criteria agree with the Standard Model expectations. Exclusion limits at the 95% confidence level were set as a function of the scalar top and scalar tau masses. Depending on the scalar tau mass, ranging from the 87 GeV limit set by the LEP experiments to a few GeV below the scalar top mass, lower limits between 490 GeV and 640 GeV were placed on the scalar top mass within the model considered.

Contents

List of Tables

List of Figures

ACKNOWLEDGEMENTS

Many thanks to Tommaso Lari, Chiara Rizzi, and the rest of the stop-stau team, as well as TRIUMF, UVic, and my other ATLAS collaborators for all their hard work, advice, support and insight. Thanks to Gina Lupino for being awesome and making me laugh. Cheers to the Potent Potables for all their answers to everything and to the Chapters book club for all our many discussions. Thank you to everyone at Romer's for their friendship, motivation, and pleasant distractions. Thanks to TRIUMF Communications and ATLAS Outreach for being the best. Danke to Ingrid, Randy, and LOoW for bring our worlds together. Thanks to Juliana Cherston for bringing the beats. Thank you to Hayley Thompson for the many laughs, entertaining stories, and great days. Thank you to QI for making life quite interesting and Time Team for bringing discoveries home. Thank you to all my friends and many thanks to my family for life, the universe, and everything. Special thanks go to my supervisor, Isabel Trigger. She has been *amazing*.

DEDICATION

For all my family.

Chapter 1

Introduction

Humanity has been studying the natural world for centuries, from the smallest of particles to galaxies and the universe itself. The science of particle physics is the study of subatomic particles and their interactions. Through humanity trying to understand the fundamental building blocks of nature, scientists have developed the Standard Model [1, 2, 3]. The Standard Model is the most accurate and complete description of the subject so far, and many parts of the model have been tested over the decades using a variety of different experiments. But yet, there are still some mysteries in the universe that the Standard Model does not address.

One of the open questions in the field of particle physics is the fine tuning problem in the Standard Model. In the Standard Model, some parameters related to the Higgs boson mass are required to have very precise values (to one part in 10^{28}) and are said to be very finely-tuned [4]. Another open question is the nature of dark matter. Astrophysical observations have shown that 85% of the mass of the universe is not made of the ordinary matter described by the Standard Model. It is postulated that this missing 85% of the mass of the universe is made up of as yet undiscovered elementary particles, which are referred to as "dark matter".

There are many different theories for physics beyond the Standard Model that can explain one or more of the open questions in particle physics. Supersymmetry is one such theory. It helps to resolve the fine-tuning problem and also contains particles that are natural dark matter candidates.

The ATLAS experiment at the LHC[1] at CERN[2] has an ambitious physics program including a range of searches for supersymmetry and the main goal of finding and

[1]Large Hadron Collider.
[2]The European Organisation for Nuclear Research.

studying the Higgs boson. The Higgs mechanism in the Standard Model generates the masses of the gauge bosons through electroweak symmetry breaking and predicts the existence of the Higgs boson. The Higgs boson was the last particle in the Standard Model left to be observed and it was discovered at the LHC in 2012 [5, 6]. A lot of different searches for Supersymmetry are performed. There are many new parameters within supersymmetry so searches for it cannot be performed by a single general analysis. Individual analyses are often optimised for specific supersymmetry models and final states. One important particle in supersymmetry is the "scalar top" (a spin-0 particle that is related to the top quark) because in supersymmetry it plays the largest role in addressing the fine-tuning problem. There are several different ATLAS searches for the scalar top because it could decay in several different ways.

One supersymmetric model being studied by ATLAS involves the production of a pair of scalar tops that each decay to a tau lepton, a jet (a collection of nearby particles) from the decay of a b-hadron, and missing transverse momentum. The missing transverse momentum in these events arises from several undetected neutrinos and the stable and neutral lightest supersymmetric particle (a dark matter candidate). The decay of a tau lepton can produce either one charged lepton, or one or more hadrons. The decay of two tau leptons thus follows one of three possible channels: one leptonically decaying tau and one hadronically decaying tau, two leptonically decaying taus, or two hadronically decaying taus. The discovery of new physics in the search for this model would be a major milestone in particle physics and might provide valuable data to help resolve the fine-tuning problem and the nature of dark matter.

This dissertation describes the ATLAS search for pair-produced scalar tops that decay to two tau leptons and large amounts of missing transverse momentum, with a focus on the channel including one hadronically decaying tau and one leptonically decaying tau. In Chapter 2 the theories of the Standard Model and supersymmetry will be presented followed by descriptions of the LHC and the ATLAS detector in Chapter 3. In Chapters 4 and 5 the data collection and reconstruction will be explained along with a description of the simulated events. The analysis itself will be described in Chapter 6 and the systematic uncertainties in Chapter 7. The results will then be presented in Chapter 8 before they are statistically interpreted in Chapter 9. The concluding remarks will finally be presented in Chapter 10.

Chapter 2

The Standard Model of particle physics and physics beyond the Standard Model

2.1 The Standard Model

The Standard Model (SM) of particle physics is currently the best known description of all the known fundamental particles and the electromagnetic, weak, and strong interactions. It is a theoretical framework that combines quantum chromodynamics and the electroweak model, which are two models that separately described the strong interaction, and the electromagnetic and weak interactions. The Standard Model has been successful in predicting the existence of several particles that were later discovered. The last particle discovered that is required as part of the Standard Model is the Higgs boson [5, 6].

All the particles in the Standard Model are summarised in Figure 2.1. They can be categorised as either fermions, which have half-integer spin, or bosons, which have integer spin. All the matter that we interact with in our day-to-day lives is made up of fermions. Bosons are the force carriers because all the fundamental interactions between two fermions require the exchange of a boson. Figure 2.2 summarises the allowed interactions in the Standard Model. The bosons of quantum chromodynamics and the electroweak model all have spin-1 (vector bosons). The Higgs boson, however, is the only known spin-0 fundamental particle (a scalar boson). The gluon, photon, W bosons, and Z boson are all gauge bosons [9].

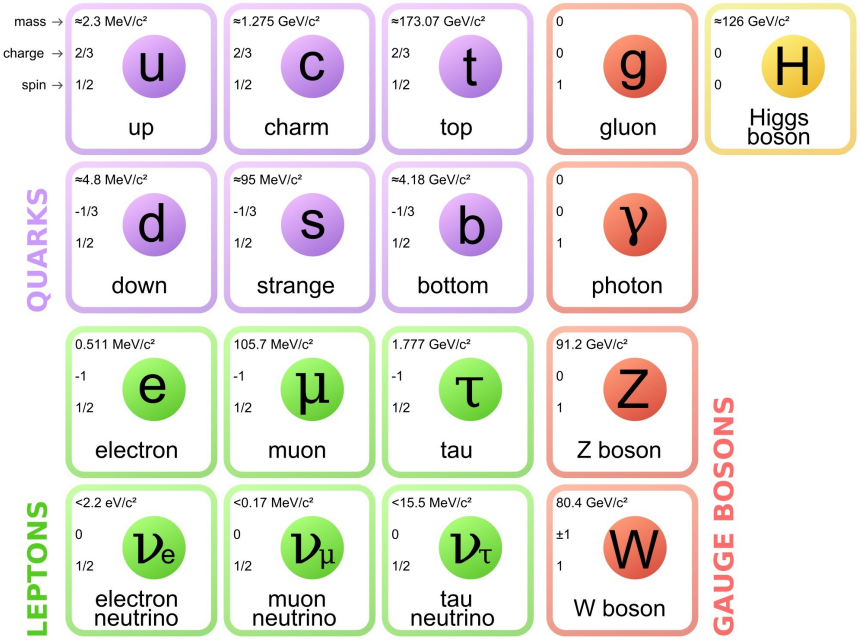

Figure 2.1: Standard Model particles [7]

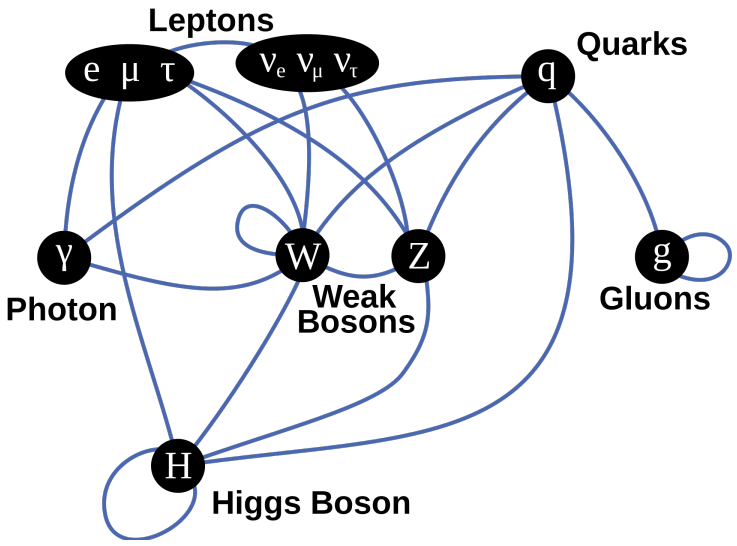

Figure 2.2: Diagram of the allowed interactions in the Standard Model [8].

There are two types of elementary fermions (f) in the Standard Model: leptons and quarks (q). Both the leptons and quarks come in three generations. Each generation includes a pair, or doublet, of particles and the two particles in the pair differ from one another by an integer electric charge. In the case of the leptons the charged fermion of each pair has an electric charge of -1 while the neutral fermion (the neutrino) has

an electric charge of zero. The quark pairs each include a quark of electric charge 2/3 and a quark of electric charge $-1/3$.

Every charged fermion in the Standard Model has an anti-matter partner with the opposite electric charge. In this document, when required, the anti-particle is indicated using a bar over the particle symbol (e.g. $t\bar{t}$) or the electric charge is indicated explicitly using a superscript (e.g. e^+e^-). Particles symbols without a charge superscript may be used to refer to either just the matter particles or to both the particles of the different possible charges (e.g. $t \to Wb$ refers to both $t \to W^+b$ and $\bar{t} \to W^-\bar{b}$). More particle charge notation will be introduced in Section 2.3.4.

The term "charged leptons" (L) will be used to refer to all three of the electrically charged leptons ($L = e$ or μ or τ) while the term "light charged leptons" (ℓ) will be used to refer just to electrons and muons ($\ell = e$ or μ). These separate terms are useful as a tau lepton has a short lifetime and can decay into an electron or muon (or hadrons), which can be directly detected. Using this terminology, the final state after a leptonic tau decay can be said to include a light charged lepton, ℓ, while a particle decay that produces a charged lepton, L, implies the creation of an electron or a muon or a tau lepton.

2.1.1 Quantum electrodynamics

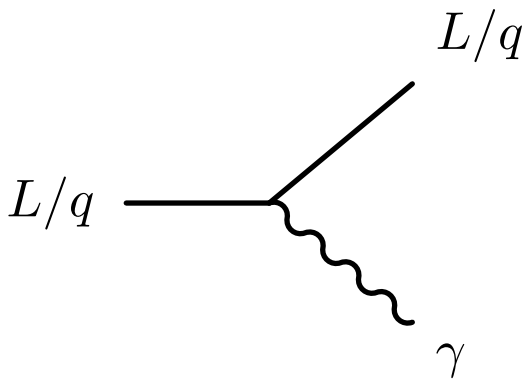

Figure 2.3: QED interaction

Quantum Electrodynamics (QED) is the theory describing the fundamental interaction of electrically charged particles through the exchange of photons. The fundamental interaction vertex of QED is shown in Figure 2.3. This vertex describes the QED process of a charged fermion either radiating or absorbing a photon. This vertex

also describes the creation or annihilation of two electrically charged fermions. Only particles carrying electric charge can interact with the photon.

2.1.2 Quantum chromodynamics

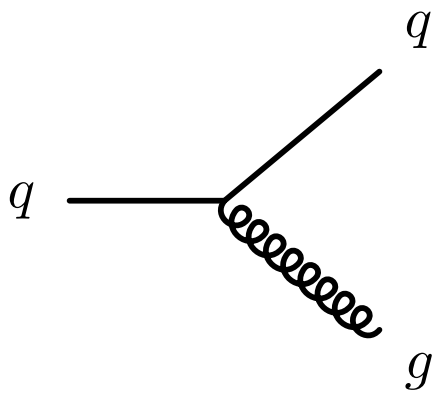

Figure 2.4: One of the QCD interactions

Quantum Chromodynamics (QCD) is the theory that describes the strong interaction of any particle carrying a strong or colour charge, through the exchange of gluons. One of the fundamental interaction vertices of QCD is shown in Figure 2.4. This vertex shows the QCD process of a quark radiating or absorbing a gluon. It also shows the process of a quark-antiquark pair being created or destroyed. Only particles carrying colour charge can interact with gluons. Gluons themselves carry colour charge and (unlike the photon) are therefore able to self-interact. There are eight different gluons that each carry a different combination of the three possible colour charges. Like the photon, gluons are massless and have no electric charge.

2.1.3 Weak interactions

The weak interaction is mediated through the exchange of a W^+ boson or a W^- boson or a Z boson. The $W^\pm$ bosons are electrically charged with a mass of 80.4 GeV while the Z boson is electrically neutral with a mass of 91.2 GeV [10] [1]. Two of the vertices of the weak interaction are shown in Figure 2.5. The Z boson interaction is similar to the QED interaction whereby a fermion can radiate or absorb a Z boson.

[1] In this dissertation natural units with $\hbar = c = 1$ are used so that momentum and mass are given in GeV.

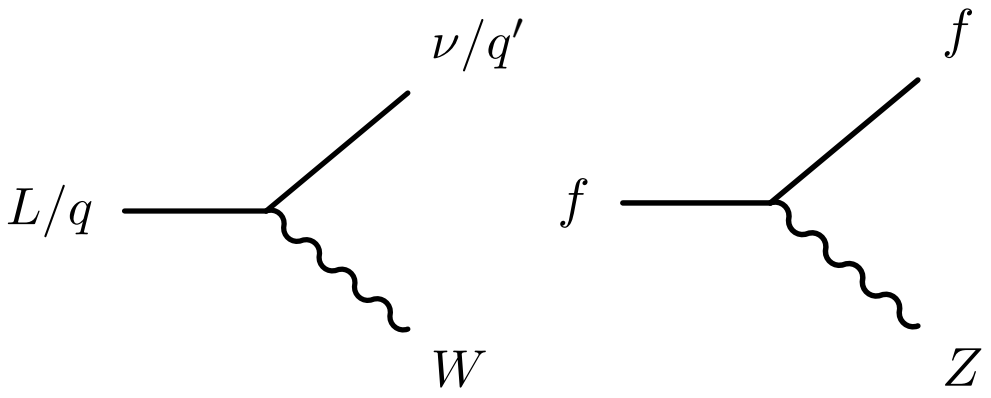

(a) W interaction (b) Z interaction

Figure 2.5: Weak interactions.

Two same-flavour fermions can also be created or annihilated. Interactions via the W bosons can be different from those of the other bosons because $W^{\pm}$ bosons are charged and necessarily imply a vertex where the two fermions change flavour, as shown in Figure 2.6. A crucial difference between the electromagnetic interaction and the weak interaction is that the electromagnetic interaction only takes place between fermions with non-zero electric charge while the weak interaction can take place between all fermions, thus allowing interactions like $Z \to \nu\bar{\nu}$. The W and Z bosons can also interact with each other and with the Higgs boson.

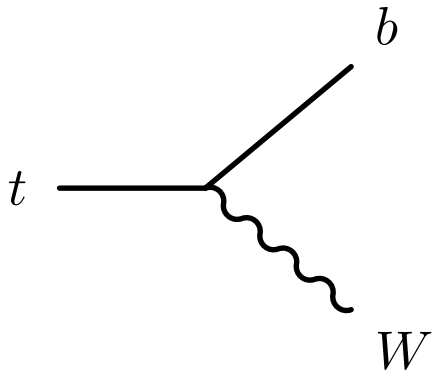

Figure 2.6: Decay of a top quark into a W boson and a bottom quark.

2.1.4 Particle masses

In the Standard Model, the masses of the W and Z bosons are acquired through electroweak symmetry breaking and their interactions with the Higgs field [10, 11]. The measured masses of the particles are shown in Figure 2.1. The top quark is the heaviest particle in the Standard Model at $\sim$ 173 GeV, while the gluons and the photon are massless. The measured mass of a particle is different from its bare mass because the mass that can be measured includes loop corrections (discussed further in Sections 2.2 and 2.3.1). In the Standard Model neutrinos were originally considered to be massless. However, the discovery of neutrino oscillations [12, 13, 14] implies that the neutrinos do have mass (albeit very small) and so they should interact with the Higgs boson. Neutrino oscillations and masses can always be neglected at collider experiments.

2.1.5 Bosons

Gluons and W bosons are able to self-interact but the photon and the Z boson cannot. The Z boson and the photon are, however, able to interact with the W boson. The Higgs boson interacts with all the fermions and bosons that have mass, including itself, since it is by interacting with the Higgs field that the particles obtain their masses.

2.1.6 Particle hadronisation and decay

In Chapter 3, a description of how different particles are detected will be given. To understand the general layout of a detector it is important to understand what particles will be directly detected. The particles that are directly detected may have been created from another particle decaying or from a particle hadronising as described in the following paragraphs.

Collectively, quarks and gluons are referred to as partons. Partons carry colour charge and participate in QCD interactions, but only color-neutral combinations of partons, hadrons, can propagate freely. The process by which these colour-neutral combinations are formed, hadronisation, is not understood in detail. The number of quarks in a hadron is used to categorise these composite particles e.g. baryons have three quarks, and mesons have a quark and an anti-quark.

The top quark, being more massive than the W boson, nearly always decays to a

bottom quark and a W boson as shown in Figure 2.6. Every quark will hadronise before it decays, with the exception of the top quark, which has a lifetime that is shorter than the amount of time required for hadronisation to take place. The hadronisation of the original parton results in a relatively narrow collection of hadrons called a jet.

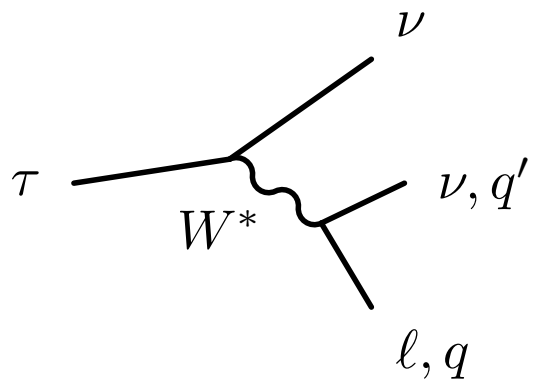

Figure 2.7: Tau-lepton decays

While muons can and do decay, in the context of this ATLAS search they can be considered effectively stable. The tau lepton is comparatively heavy and will decay very quickly (lifetime $\sim 10^{-13}$ s) into neutrino(s) and an electron or muon, or quarks, as shown in Figure 2.7. A tau lepton that decays hadronically will be referred to as τ_{had}. In the context of this ATLAS search the decay length of a tau lepton is small but measurable ($c\tau = 87\ \mu$m). The decays of a tau lepton are categorised as either leptonic or hadronic depending on the types of particles produced. Neutrinos only interact via the weak interaction and are the only particles in the Standard Model that will normally escape ATLAS undetected. Any particle that escapes the detector undetected is referred to as an invisible particle and the presence of one or more invisible particles is inferred by measuring the residual momentum in a conservation of momentum calculation performed using momenta projected into the transverse plane (missing transverse momentum). The magnitude of the missing transverse momentum is referred to as the missing transverse energy, $E_{\text{T}}^{\text{miss}}$.

The W and Z bosons have short lifetimes ($\sim 10^{-25}$ sec). The leptonic and hadronic decays of the W boson are shown in Figure 2.8. The photon is massless and stable. The gluons are also massless but they carry the colour charge and so hadronise.

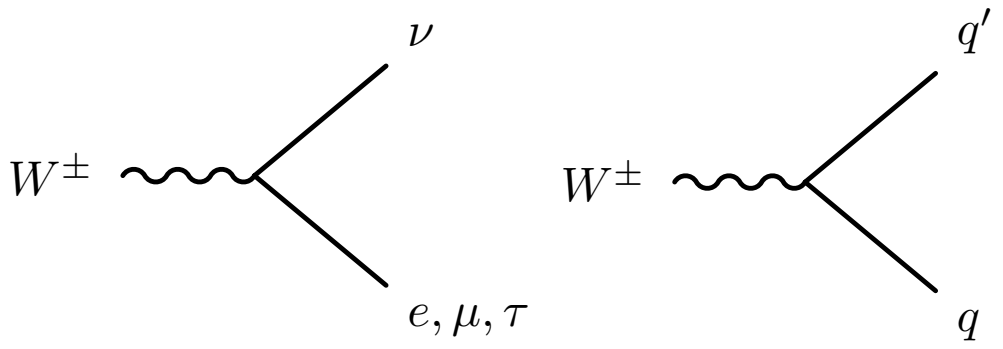

(a) Leptonic W decay (b) Hadronic W decay

Figure 2.8: Leptonic and hadronic W decays.

2.2 Open questions in particle physics

The Standard Model has been very successful at describing all the known particles and their interactions as discussed in Section 2.1. There are still several open questions in particle physics. Some of those questions, which are beyond the scope of this document, include: "what are the masses of neutrinos and are they their own antiparticles (Majorana particles) [15]?", "what is the quantum theory of gravity [16]?", "why is there a matter-anti-matter asymmetry to the universe [17]?", and "why are there three generations of leptons and quarks [18]?". Two open questions being studied at ATLAS include the nature of dark matter [19, 20, 21], and the fine-tuning problem [11, 22, 23, 24, 25].

Cosmological studies have found problems in describing the physics of galaxies. The results of fits to the cosmic microwave background data indicate that about 85% of the mass in the observable universe is composed of non-baryonic matter that interacts gravitationally but not electromagnetically (we do not know about its short-distance interactions) [26, 27]. This matter is referred to as dark matter. Unfortunately, there are no particles in the Standard Model that are viable candidates to make up the large mass of dark matter. Some extensions to the Standard Model introduce new particles that could constitute dark matter.

The fine-tuning problem is related to the mass of the Higgs boson ($\sim$ 125 GeV [28]). The mass of the Higgs boson is composed of the bare mass value and loop corrections. The bare mass is the mass that can be inserted directly into the equations that define the model (the Lagrangian). The mass measured in experiments is the bare mass with all the loop corrections to it. The lowest-order loop corrections to

the Higgs mass from fermions are shown in Figure 2.9 (left) and the largest overall correction is from a top-quark loop. Unless there is extremely precise cancellation between the Higgs boson bare mass (value unknown and not calculable within the SM) and the large loop corrections to it, which may be of the order of the Planck mass ($\sim 10^{19}$ GeV), then one would expect the Higgs boson's measured mass also to be large. Some extensions to the Standard Model cancel the loop corrections to the bare mass with additional corrections of the opposite sign to greatly reduce the requirement for fine-tuning. The level of fine-tuning deemed "acceptable" is subjective but most people consider the levels of fine-tuning in the Standard Model (roughly to one part in 10^{32} assuming a momentum scale cut-off at the Planck mass [29]) to be unappealing.

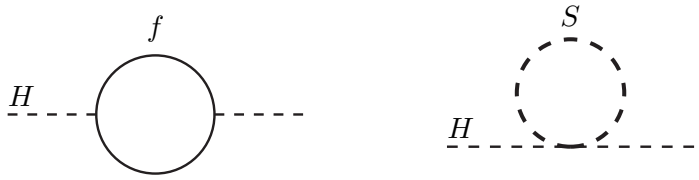

Figure 2.9: Higgs-mass corrections [30]. On the left are the first-order loop corrections from a fermion to the mass of the Higgs boson squared and on the right are the first-order loop corrections from a new scalar particle.

2.3 Supersymmetry

Supersymmetry is a theory of physics beyond the Standard Model that provides solutions to some of the open questions in particle physics [31, 32, 33, 34, 35, 36, 37, 38, 39]. It solves the fine-tuning problem and introduces new particles, some of which are dark matter candidates. These new particles could have masses discoverable at the LHC [11, 30].

The Standard Model contains various symmetries, and theories of physics beyond the Standard Model often introduce new ones. A "supersymmetry" is a symmetry that relates fermions and bosons. Supersymmetric extensions of the Standard Model introduce new partner particles to those in the Standard Model that differ from them by half a unit of spin: all the spin-1 bosons of the Standard Model have spin-1/2 superpartners, and all the spin-1/2 Standard Model particles have spin-0 superpartners. The new partner particles will be referred to as supersymmetric particles and

are denoted by putting a tilde over the symbol for the particle. The Higgs sector will be discussed in Section 2.3.2.

If supersymmetry were an unbroken symmetry then the supersymmetric particles would have the same masses as their Standard Model counterparts. Since no supersymmetric particles have been discovered with the same masses as their Standard Model partners, if supersymmetry exists it must be a broken symmetry. In practical terms, the symmetry must be broken in such a way that the supersymmetric particles would have thus far escaped detection by the existing experiments. This means for most supersymmetric particles that they would have to have very large masses. There are a variety of ways in which supersymmetry can be broken and so there are a variety of different supersymmetric models.

2.3.1 Supersymmetry and the open questions in particle physics

Most supersymmetric theories naturally include a dark matter candidate. A dark matter candidate must be stable (or at least have a very long lifetime) so often the "lightest supersymmetric particle" (LSP) is a dark matter candidate (the other supersymmetric particles will eventually decay into the LSP). The dark matter candidate must also be electrically neutral to ensure that it does not interact electromagnetically.

The largest loop corrections to the Higgs boson mass come from the top quark. In supersymmetry the loop corrections involving the supersymmetric particles naturally cancel out the loop corrections involving their Standard Model partners. The top quark has a supersymmetric partner called the scalar top, $\tilde{t}$, or "stop" that is important because it cancels out the dominant top-quark corrections to the Higgs mass (see Figure 2.9 - right). If supersymmetry were an unbroken symmetry then the loop corrections to the Higgs boson mass from the top quark would be exactly cancelled by those of the scalar top. Since supersymmetry has to be broken, the two will not exactly cancel each other, but as long as the mass of the scalar top is not too large there can still be sufficient cancellation to reduce the fine-tuning to acceptable levels.

2.3.2 Minimal Supersymmetric Standard Model

The Minimal Supersymmetric Standard Model (MSSM) is a theory of physics beyond the Standard Model that realises supersymmetry. It is the minimal phenomenologically viable extension to the Standard Model [30]. The MSSM includes

all the phenomenologically viable ways to break supersymmetry in the most general way and so while the MSSM may be minimal in terms of the number of new particles and new interactions consistent with phenomenology [40], it has over 100 free parameters [30], most of which are related to supersymmetry breaking rather than supersymmetry itself. The naming conventions for the various bosons and fermions in supersymmetry are given in Table 2.1.

Table 2.1: Summary of the naming conventions for supersymmetry and the particle/field superpartners. The neutralinos and charginos are the result of the mixing of the neutral and charged gauginos and higgsinos respectively.

Fermions	Bosons
fermion	sfermion
lepton	slepton (or scalar lepton)
tau lepton	scalar tau (or stau or tau slepton)
neutrino	sneutrino (or scalar neutrino)
quark	squark (or scalar quark)
top quark	scalar top (or stop or top squark)
higgsino	higgs boson
gluino	gluon
gaugino	gauge boson
gravitino	graviton
neutralino (after mixing)	-
chargino (after mixing)	-

The MSSM does not just include new supersymmetric partner particles but it also requires two Higgs doublets rather than just one. In electroweak symmetry breaking a gauge transformation can reduce the four degrees of freedom of the single SM Higgs doublet to just one [41, 42, 43, 44, 45, 46]. The remaining one degree of freedom is the Standard Model Higgs boson. The Nambu-Goldstone bosons associated with the other three degrees of freedom are "eaten" by the now massive W and Z bosons [47]. In supersymmetry the eight degrees of freedom of the two scalar Higgs doublets get reduced to five, resulting in two electrically charged and three electrically neutral Higgs bosons. In the fermion sector, there is no analogue to the Higgs mechanism that requires that there be a fermionic partner to the photon that is also massless. Since the partners of the electroweak gauge bosons and Higgs bosons carry the same quantum numbers, the observed mass eigenstates can be mixtures. These mass eigenstates are called neutralinos and charginos.

Many models of supersymmetry, including the MSSM, also require conservation of R-parity. R-parity is a multiplicative quantum number with values of -1 for the supersymmetric particles and $+1$ for the SM partners. The conservation of R-parity implies that all interaction vertices are only allowed to contain an even number of supersymmetric particles. This implies that the supersymmetric particles will be produced in pairs at the LHC. R-parity conservation implies that the MSSM is phenomenologically viable by forbidding interactions that could result in proton decay, which is not observed in nature [30]. R-parity also ensures that the LSP is absolutely stable, which helps to ensure that the LSP is a viable dark matter candidate. Often in the MSSM (although not in this analysis) the lightest neutralino is taken to be the LSP and a dark matter candidate.

2.3.3 Gauge Mediated Supersymmetry Breaking

Gauge Mediated Supersymmetry Breaking (GMSB) is an extension of the MSSM [48, 49, 50, 51, 52, 53]. In this model there are two sectors of particles: the visible sector, which contains the MSSM particles (the SM particles and their superpartners), and a hidden sector, which contains a collection of new particles that are not part of the MSSM. The supersymmetry breaking occurs in the hidden sector. These particles in the hidden sector only have very small or no couplings to the visible sector. The supersymmetry breaking is communicated from the hidden sector to the visible sector through some new messenger particles. The two sectors and the messengers are shown in Figure 2.10.

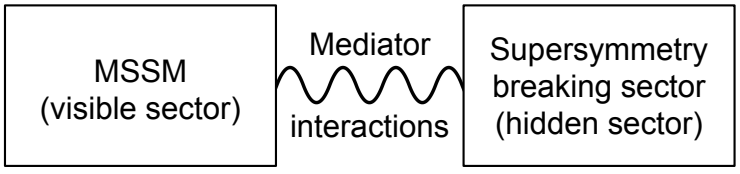

Figure 2.10: Supersymmetry sectors. The mediator interactions connect the hidden sector to the visible sector.

GMSB is one of several models where messenger particles are used to communicate the SUSY breaking from the hidden sector to the visible sector. In GMSB, gauge interactions are responsible for passing the effects of supersymmetry breaking to the visible sector. There are several messenger particle pairs (fermion and boson superpartner pairs) that couple to the hidden sector, where supersymmetry is broken.

The breaking causes the fermion messenger particles to have different masses from the boson messenger particles. The messenger particles couple to the gauge bosons and their superpartners in the visible sector. It is through loop corrections involving the messenger particles that the gauge boson superpartners obtain different masses from the gauge bosons. It is through loop diagrams involving the gauge boson superpartners that the visible sector scalars obtain different masses from their partners. The result is that the supersymmetric particles in the visible sector have different masses from their Standard Model partners. In the simplest versions of GMSB, the masses of the visible sector particles depend on just five parameters [54].

An additional part of GMSB is the important role of the graviton and the gravitino, $\tilde{G}$. All known fundamental interactions are mediated by one or more messenger particles and so the graviton is theorised to be the mediator of gravity. While a complete theory of quantum gravity does not exist, extensions to the Standard Model have been created that include gravity and are valid as effective field theories for energies well below the Planck scale [55, 16]. These models include a massless spin-2 graviton. In theories of supersymmetry that include gravity, the gravitino is the superpartner of the graviton and is a spin-3/2 particle. In GMSB the gravitino is the LSP [10, 56]. In a similar way to how the gauge bosons "eat" the three scalar bosons after the spontaneous electroweak symmetry breaking, the gravitino "eats" a spin-1/2 particle after the spontaneous breaking of supersymmetry. Through "eating" the spin-1/2 particle the gravitino picks up a mass and new couplings to the Standard Model particles and their superpartners. The new couplings can be much larger than the original couplings, which enhances the effective couplings of the gravitino.

2.3.4 A simplified model of scalar tops and scalar taus

This work is a search for the production of pairs of oppositely charged scalar tops, $\tilde{t}\tilde{t}^*$, where each scalar top decays into a scalar tau and subsequently into a gravitino (the LSP in this model) as shown in Figure 2.11. The scalar top has an electric charge of 2/3 like the top quark and the charge conjugate of the scalar top, $\tilde{t}^*$, has an electric charge of $-2/3$. Each scalar top undergoes a 3-body decay to produce a b quark, a neutrino, and a scalar tau. The scalar tau, or "stau", is the supersymmetric partner to the tau lepton. The scalar tau decays to produce a tau lepton and a gravitino. The final state includes two b-jets (from the hadronised b quarks), two tau leptons (where each tau lepton decays either hadronically or leptonically), and missing energy (from

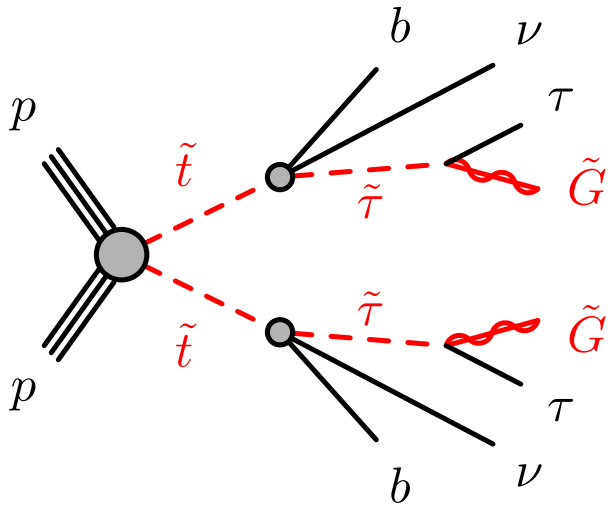

Figure 2.11: Scalar top production and decay [57]

the gravitinos and neutrinos). In this model the masses of the scalar top and the scalar tau are unknown while the mass of the gravitino is very small (negligible). It is assumed that the scalar top is heavier than the scalar tau. The three-body decay of the scalar top can be understood as the decay of the scalar top into a b quark and a virtual chargino, which then decays into a neutrino and a scalar tau. The scalar top undergoes a 3-body decay because the chargino is heavier than the scalar top. The 3-body scalar top decay is analogous to the 3-body decay of the tau lepton shown in Figure 2.7.

In supersymmetry the superpartners of the left-handed and right-handed fermions can mix to form mass eigenstates. The lighter of the two scalar tops is denoted $\tilde{t}_1$ and is referred to as the scalar top in the following. Likewise, the lighter of the two scalar tau eigenstates is denoted $\tilde{\tau}_1$ and referred to as the scalar tau.

This model is a simplified model. All the supersymmetric particles not explicitly shown in Figure 2.11 are assumed to be very heavy and can be ignored. The branching ratio for each of the supersymmetric particle decays is assumed to be 100%. It is also assumed that the scalar taus and gravitinos are only produced through the decay of the scalar tops. Studying a simplified model makes the analysis less dependent on the the details of specific models. The information gathered from studying several different simplified models can then be combined together to get a better understanding of the larger picture [58]. An alternative to using a simplified model can involve scanning through the various model parameters of the phase space.

Studying this simplified model contributes towards the larger work of the search for scalar tops and supersymmetry, the search for physics beyond the Standard Model, and the search for solutions to the open questions in particle physics. This search contributes towards a better understanding of the fine-tuning problem since it is a search for scalar tops. It may also contribute towards a better understanding of dark matter with the gravitino potentially being a component of dark matter. Other searches for pair-produced scalar tops at the LHC [59, 60, 61, 62, 63, 64, 65] focus on MSSM-based models (rather than a GMSB model) and typically still simplified models. They also look at a variety of different decays (that do not involve a scalar tau), and they isolate different final states (by vetoing hadronically decaying taus).

For a particle in a model to be a valiable dark matter candidate, several properties of the model must agree with cosmological observations [66]. The properties of this simplified model may or may not all agree with the cosmological observations but exact agreement is not explicitly required because we are studying a simplified model. In general simplified models can be used to investigate the generic properties of SUSY models, including their ability to produce dark matter candidates that satisfy cosmological constraints.

2.4 Calculating cross-sections

Cross-sections cannot currently be calculated exactly. Feynman diagrams help physicists break down the calculation of the cross-section of a particular process by expanding the calculation into an infinite series using perturbation theory. One or more Feynman diagrams are associated to a process at a particular order in the expansion. The strong production cross-sections are expanded in orders of α_S. The larger the number of vertices within a Feynman diagram, the higher the order of the process. The left diagram in Figure 2.9 shows an example where the Higgs boson has a higher order loop correction. See Chapter 5 for details on the order of the expansions used for the different processes of this analysis.

Chapter 3

The ATLAS detector and the LHC

ATLAS is a multipurpose experiment built at the CERN LHC to study the fundamental particles of nature and their interactions at the smallest scales. Producing the rare interactions that the ATLAS collaboration wants to study requires extremely high energies and the Large Hadron Collider is the world's highest energy particle accelerator. It was built in the pre-existing tunnel that once housed the Large Electron Positron collider (LEP). The LHC is the same radius as LEP; however, it can accelerate two proton beams, instead of an electron beam and a positron beam. By accelerating bunches of protons in circles it can take them up to high energies and when colliding particles at high enough energies, new heavy particles can be created. These particles or their decay products can be detected by ATLAS. The descriptions of the detector in this chapter depict its state up to and including the year 2012, the time period of interest for this work. In 2015 the LHC started colliding protons at a centre of mass energy of 13 TeV, or equivalently 6.5 TeV per beam.

3.1 The Large Hadron Collider

The LHC at CERN is a particle accelerator that was designed to test the Standard Model, study the Higgs boson, and search for new physics beyond the Standard Model. The LHC enables the experiments to study particle physics in unexplored regions of phase space by simultaneously providing high collision energies and large luminosities to study rare processes. The LHC has a design energy of 7 TeV per beam and has collided protons and lead ions. These high energies are reached by the use of powerful superconducting magnets and accelerator cavities. Accelerator cavities use

large electric fields to accelerate particles and group them into bunches rather than having a constant stream of particles. The oscillating electric fields accomplish this by either accelerating or decelerating the particles that deviate from the mean expected energy of the bunch. The LHC beams have a nominal bunch spacing of 24.95 ns [67], which translates to a nominal bunch crossing rate of 40.08 MHz. The magnets bend the trajectories of the particles in the beams for a variety of purposes including the steering of the particles around the 27 km circumference, and the focusing of the beams into smaller cross-sectional areas.

In each bunch crossing there can be multiple proton–proton collisions but analyses focus on only one proton–proton collision in each bunch crossing. Additional proton–proton interactions in the same ("in-time") and nearby ("out-of-time") bunch crossings are called pile-up. In ATLAS a bunch crossing defines an event. For the experiments to study rare events a large number of proton–proton collisions is required. A trade-off exists between the number of proton–proton collisions per bunch crossing and the complexity of an event with regards to the accurate reconstruction and measurement of the physics processes that have taken place. The LHC beam crossing settings are tuned to give the different experiments different mean numbers of proton–proton collisions per bunch crossing. In accelerator physics luminosity is used as a measure of the interaction rate in the accelerator. The number of expected events, N, is the product of the cross-section of the process(es) of interest, σ, and the time integral over the instantaneous luminosity, $\mathcal{L}$: $N = \sigma \times \int \mathcal{L}\,(t)\,\mathrm{d}t$ [10]. The integral of the instantaneous luminosity is called the integrated luminosity and is typically measured in units of fb^{-1}.

3.2 The ATLAS detector

ATLAS is located in a cavern $\sim$ 100 m underground and is approximately 44 m long and 25 m in diameter as shown in Figure 3.1. The detector includes a cylindrical region around the beam called the barrel and disk-like end-caps on each end. In the ATLAS coordinate system both the x and y axes are in the plane orthogonal to the beam pipe with the x-axis pointing towards the centre of the LHC ring and the y-axis pointing upwards. The z-axis points along the LHC beam pipe and this right-handed coordinate system is centred on the centre of the detector. The radius (in polar coordinates) is $r = \sqrt{x^2 + y^2}$. The angle ϕ (in polar coordinates) is the azimuthal angle measured from the x-axis and θ is the polar angle (in spherical

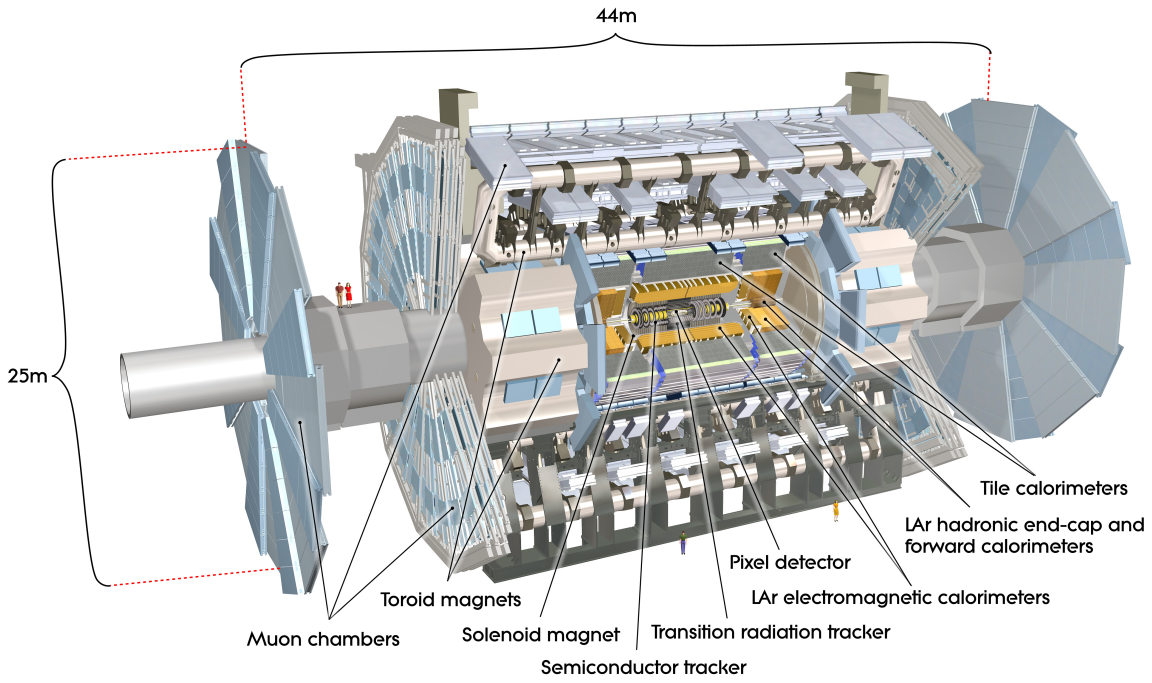

Figure 3.1: Cutaway diagram of ATLAS showing the major components of the detector [68].

coordinates) measured from the z-axis. In hadron colliders $\eta = -\ln\left(\tan\left(\frac{\theta}{2}\right)\right)$ is used instead of θ where η is called the pseudorapidity. This variable is preferred because at a hadron collider the distribution of particles in a detector is approximately flat as a function of pseudorapidity [10]. Pseudorapidity is an approximation of rapidity $y = \frac{1}{2}\ln\left(\frac{E+p_z}{E-p_z}\right)$ when $|p| \gg m$ and is useful because the difference between the rapidity values of two particles is invariant under a Lorentz boost along the z-axis. When $|p| \gg m$, pseudorapidity differences are approximately Lorentz invariant. In hadron collider physics a particle's momentum and energy are often studied in the transverse plane, where they are referred to as the transverse momentum, p_{T}, and transverse energy, E_{T}. The transverse momentum is calculated as $p_{\mathrm{T}} = \sqrt{p_x^2 + p_y^2}$ and the transverse energy is defined as $E_{\mathrm{T}} \equiv E\sin\theta = E/\cosh\eta$. This is often done because while the two colliding beams have the same energy, the partons within each of the colliding protons can have widely varying shares of the momentum. As a result of this, the momenta of the colliding partons in the $\pm z$ direction before the collision are unknown. However, the colliding partons have approximately zero momentum in the transverse direction and so the transverse momenta of all final-state particles

must sum to zero.

The ATLAS detector is built in roughly cylindrical layers, each designed to identify and measure different types of charged and neutral particles [1]. The inner detector is the closest to the beam pipe and is used to make high-precision measurements of the tracks of the charged particles as they travel outwards from the collision point. Surrounding the inner detector are the two calorimeters that are used to measure the energies of the particles. The innermost calorimeter is the electromagnetic calorimeter. It measures the energies of particles that lose most of their energy through electromagnetic interactions. Surrounding the electromagnetic calorimeter is the hadronic calorimeter. It is designed to measure the energies of the particles that can interact via the strong interaction. Surrounding the calorimeters is the muon spectrometer. High energy muons are the only known charged particles able to traverse the whole detector without decaying or losing a large fraction of their energy, so the muon spectrometer is the outermost and largest layer of ATLAS. It is designed to perform charged particle tracking. The last major component of ATLAS is the magnet system. The purpose of the magnets is to curve the trajectories of charged particles to determine their charges and momenta.

Some detector components are made to perform precise and accurate measurements while others produce fast measurements. Fast measurements are required for triggering (to be discussed in Chapter 4), which is the process of determining which events should be saved to disk.

3.2.1 Detector layers and purposes

Particle physics collider experiments are built in layers around the interaction point. The ordering of these layers is important to properly detect, measure, and identify the particles. The fundamental particles in the Standard Model have lifetimes of various durations; some can be detected directly while others decay promptly and only their decay products are detected. Table 3.1 and Figure 3.2 show how various fundamental and composite particles in the Standard Model are detected by ATLAS.

[1] All instances of the terms charged and neutral refer to the electric charge unless specified otherwise

Table 3.1: Summary of how the fundamental and composite particles in the Standard Model are reconstructed. See Chapter 2.1 for a more detailed description of the physics of the Standard Model and Section 4.2 for a more detailed description of how light charged leptons, jets, and the missing transverse momentum are reconstructed. Here "q" refers to one of the light quarks: u, d, c, or s.

Particle	Reconstruction methods
e	Directly detected : Inner detector track + energy deposit in the electromagnetic calorimeter
μ	Directly detected: Inner detector track + (usually) small energy deposits in the calorimeters + muon spectrometer track
τ	Decays promptly: $\tau \to e\nu\nu$, or $\tau \to \mu\nu\nu$, or $\tau \to$ 1-3 charged hadrons + ≥ 0 neutral hadrons + ν (like a jet). Origin of the tau decay slightly displaced from the location of the pp interaction point.
Photon	Directly detected: Energy deposit in the electromagnetic calorimeter + no inner detector track.
All neutrinos	Escape ATLAS undetected: Their presence is inferred by looking at the missing transverse momentum in the event.
gluons, and u, d, c, and s quarks	Hadronise and detected as jets: Energy deposits in the calorimeters + several inner detector tracks.
t quark	Decays promptly: $t \to bW$
b quark	Hadronises and detected as a jet: Energy deposits in the calorimeters + several inner detector tracks. The origin of the weakly-decaying b hadron decay within the jet is slightly displaced from that of the pp interaction point.
W boson	Decays promptly. $W \to \ell\nu$, or qq'
Z boson	Decays promptly. $Z \to \ell^+\ell^-$, or $\nu\nu$, or $q\bar{q}$
Higgs boson	Decays promptly: Discovered through the decay channels: $\gamma\gamma$, WW, and ZZ. Other decay channels are also possible and even preferred, e.g. $b\bar{b}$.

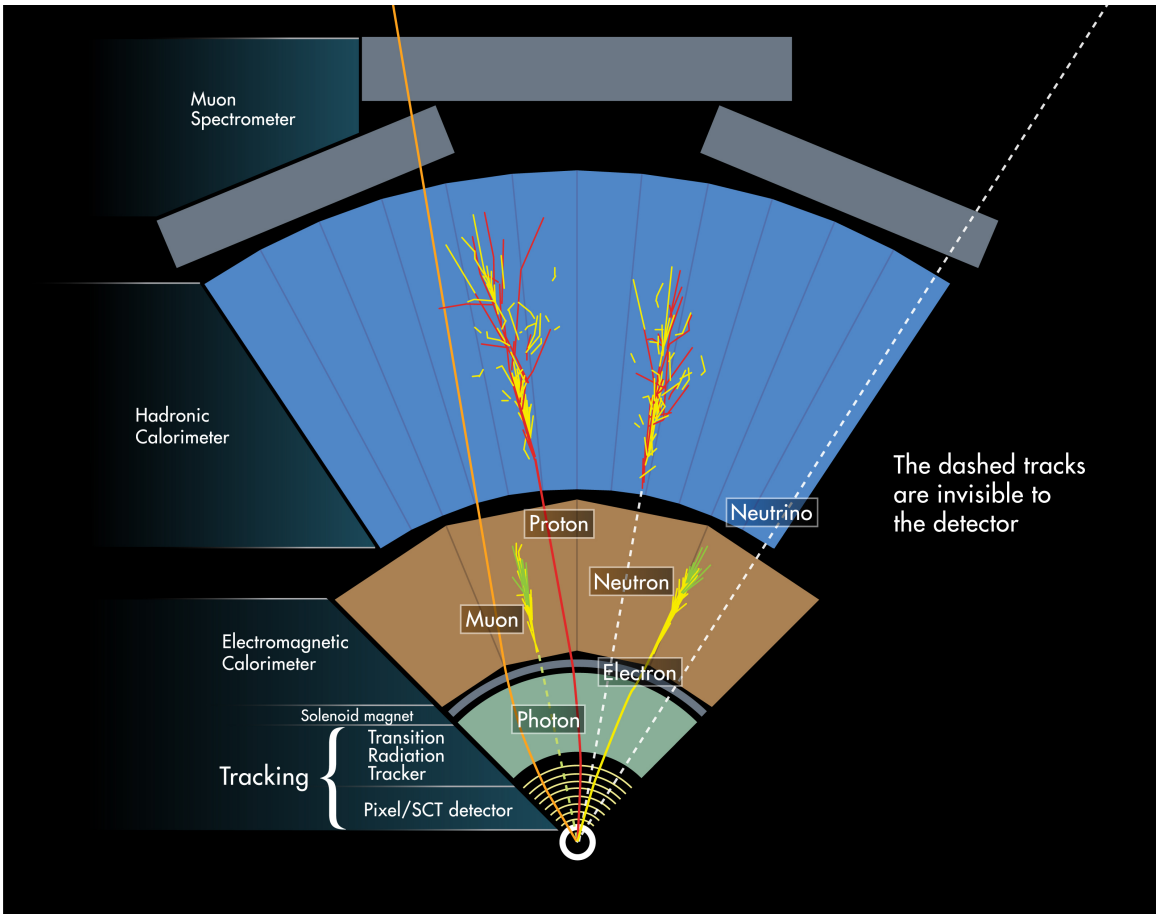

Figure 3.2: Cutaway diagram of ATLAS showing how different particles interact with the detector [69]. The diagram incorrectly depicts the interaction of hadrons in the electromagnetic calorimeter as they start their showering in the electromagnetic calorimeter.

3.3 Inner detector and solenoid magnet

The inner detector is the tracker used to measure the momenta and trajectories of all the charged particles in an event. It is approximately cylindrical in shape and is immersed in a 2 T axial magnetic field generated by a solenoid [68]. The solenoid bends the charged particle tracks in the r-ϕ plane. The detector was designed to be able to cope with a high rate of up to 1000 particles (from the collision point) passing through its acceptance region of $|\eta| < 2.5$ every 25 ns [68]. The detector also requires good momentum resolution and vertex resolution. To achieve these the inner detector of ATLAS has a fine detector granularity constructed with silicon pixel and strip detectors close to the beam pipe. These silicon detectors make up the

Pixel detector and the SemiConductor Tracker (SCT). Farther away from the beam pipe straw tubes make up the Transition Radiation Tracker (TRT). The systematic uncertainties related to tracks reconstructed in the inner detector will be discussed in Chapter 7.

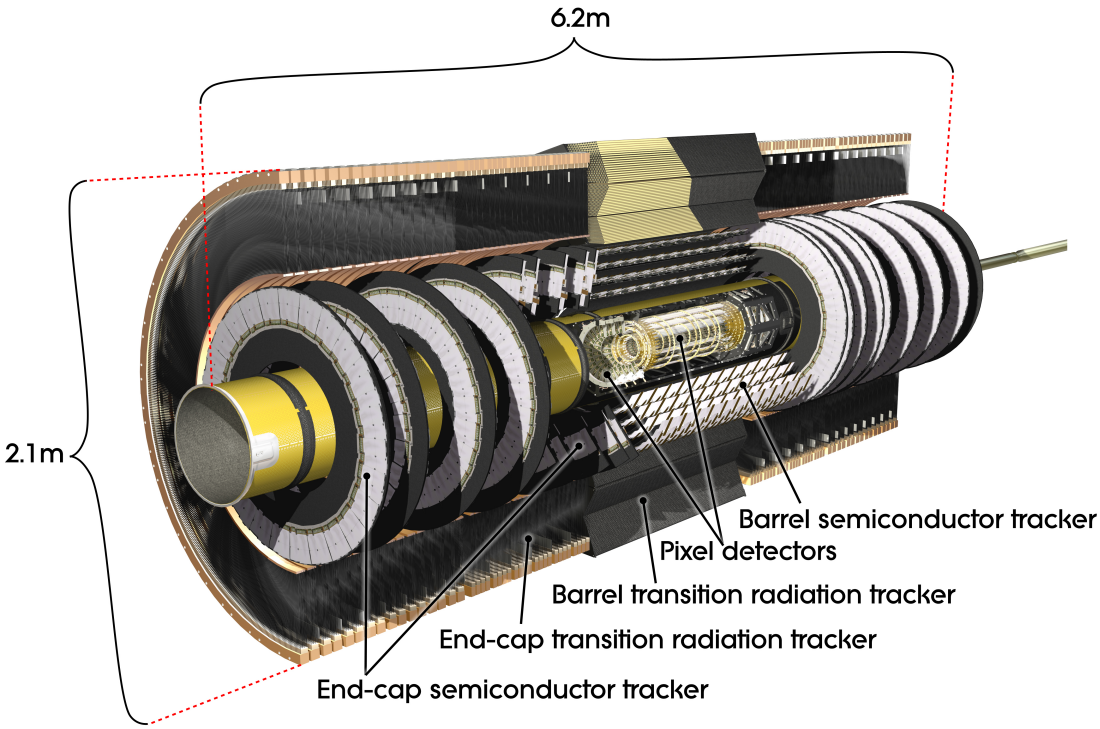

Figure 3.3: Cutaway diagram of the ATLAS inner detector showing its major components [68].

3.3.1 Pixel and SCT

The precision tracking detectors, pixel and SCT (microstrips), are arranged in concentric cylinders in the barrel region and in disks in the end-cap regions as shown in Figures 3.3 and 3.4. They are made up of silicon detectors that cover the full inner detector η range of $|\eta| < 2.5$. The sensors are reverse-biased diodes and when a charged particle passes through one of these semiconductor detectors, a small current is measured.

Within the barrel, these detectors are arranged into three pixel layers and four SCT layers. In the end-cap regions they are arranged into three pixel disks and nine SCT disks. The high-precision tracking is achieved using spatial points from the pixel

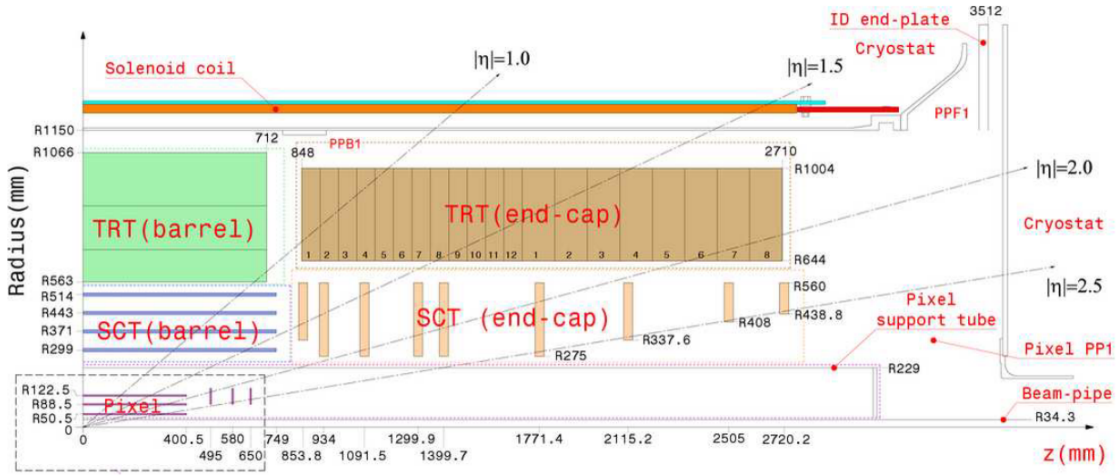

Figure 3.4: Plot of the ATLAS inner detector showing its dimensions [68].

layers. The high-precision tracking from the SCTs in both the barrel and the end-cap regions is achieved using two planes of silicon microstrip sensors placed back-to-back in each layer. The two planes of sensors are parallel but the SCT strips in the planes are at an angle of 40 mrad to each other. This stereo angle allows the SCTs to measure the z coordinate in the barrel and the r coordinate in the end-cap region. The small size of the stereo angle focuses the precision measurement capabilities of the strip on the coordinates important to the bending directions of the charged particles for accurate momentum measurements. For a typical track in the barrel region, there are three pixel hits and eight SCT hits.

3.3.2 Transition radiation tracker

Unlike the pixel and SCT, the TRT only covers the region of $|\eta| < 2.0$. The TRT straw tubes are small-diameter drift tubes that are aligned parallel to the beam axis in the barrel region and radially in wheels in the end-cap regions. On the walls of the tube there is a cathode and along the axis of the tube is an anode wire. The tube contains a gas mixture that ionises when a charged particle passes through the detector, the resulting charges are collected on the electrodes, and the signal is read out on the anode wire. Within the barrel the straw tubes are arranged into 73 layers and in the end-caps they are arranged into 20 wheels with 8 straw layers per wheel. A typical track in the barrel region is shown in Figure 3.5. There is a total of approximately 36 hits along a typical track in the barrel region. The drift tubes provide track measurements of $r - \phi$ in the barrel and $z - \phi$ in the end-cap regions.

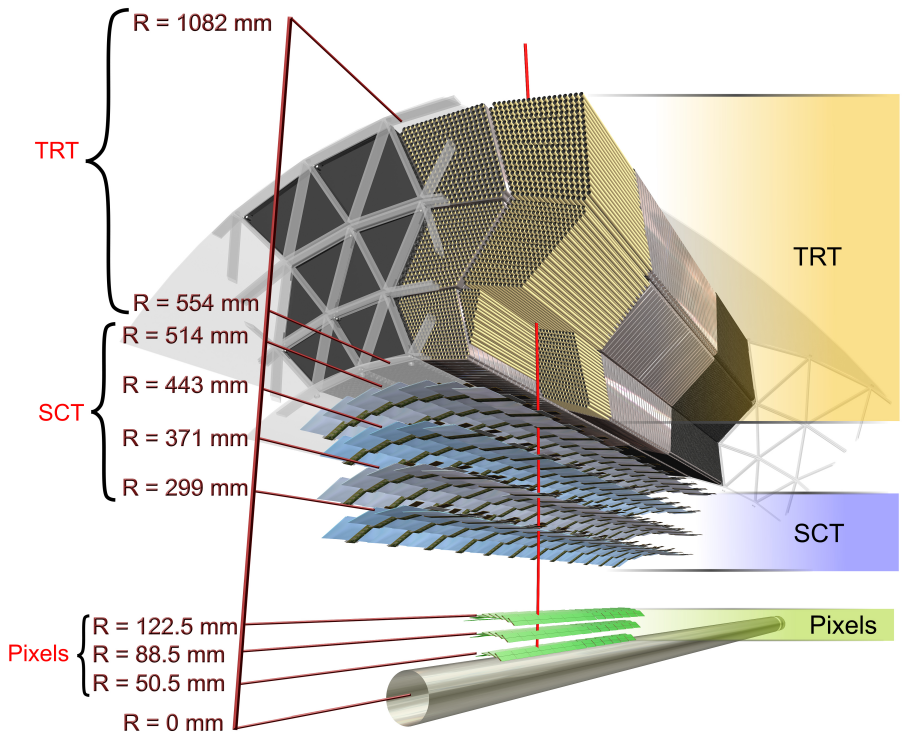

Figure 3.5: Cutaway diagram of the ATLAS inner detector showing the trajectory of a charged track through the barrel [68].

The transition radiation from the traversing particles is used for particle identification. This is particularly useful for distinguishing electrons from pions.

3.3.3 Solenoid magnet

The ATLAS superconducting solenoid produces a magnetic field to bend the tracks of charged particles. It is located between the inner detector and the calorimeters in the cryostat with the calorimeters. Since the EM calorimeter is situated immediately outside the solenoid, the magnet's windings are made to minimise as much as possible the number of interactions with traversing particles [70]. The solenoid assembly contributes approximately 0.66 radiation lengths for a particle traversing it at normal incidence [68]. When running with the nominal operational current the magnet produces a field of 2 T at the centre of the detector.

3.4 Calorimeters

The ATLAS calorimeters (see Figure 3.6) are used to measure the energy of the particles produced in collisions. The detector has excellent electromagnetic (EM) calorimetry for measurements of electrons and photons, and nearly full coverage for the hadronic calorimetry for accurate jet reconstruction and missing energy measurements [68]. The calorimeters are designed to ensure that particle showers are contained to limit leakage into the muon spectrometer.

The calorimeters cover the η range of $|\eta| < 4.9$. The depths of the calorimeters are important to maximise containment. In the electromagnetic calorimeter there are > 22 radiation lengths (X_0) of active material in the barrel region and $> 24X_0$ of active material in the end-caps. In the hadronic calorimeter there are approximately 9.7 interaction lengths (λ) of active calorimeter in the barrel region and approximately 10 interaction lengths of active calorimeter in the end-caps (see Figure 3.7). Figure 3.7 also shows that in front of the hadronic calorimeters there are approximately two interaction lengths of material, including the instrumented EM calorimeter. In the η region of the EM calorimeter that matches the inner detector coverage there is a fine granularity to give precision measurements of electrons and photons. The hadronic calorimeters have nearly full coverage for accurate missing energy measurements and are symmetric around the beam axis for uniform resolution.

The ATLAS calorimeters are sampling calorimeters, composed of alternating layers of absorbers and active media. Sampling calorimeters are designed such that the energy measured by the active layers is proportional to the total energy. As a particle passes through a sampling calorimeter it interacts with a high-density material, the absorber, and creates a shower of particles that then pass through the active medium, which measures some of the energy of the particles. Electromagnetic and hadronic showers in the ATLAS calorimeters are nearly completely contained in their volume, while only a fraction of the deposited energy is sampled in repeated measurements along the calorimeter depth. The thickness of the layers is optimised to provide good longitudinal sampling of the shower profile. If the shower is contained, then a sampling calorimeter calibrated for the various responses of the electromagnetically and hadronically interacting particles can measure the initial energy of the original particle. The liquid-argon calorimeters are so named because they use liquid argon (LAr) as the active medium. In this type of calorimeter, the liquid argon ionises as a charged particle passes through it and the charges are picked up on electrodes to

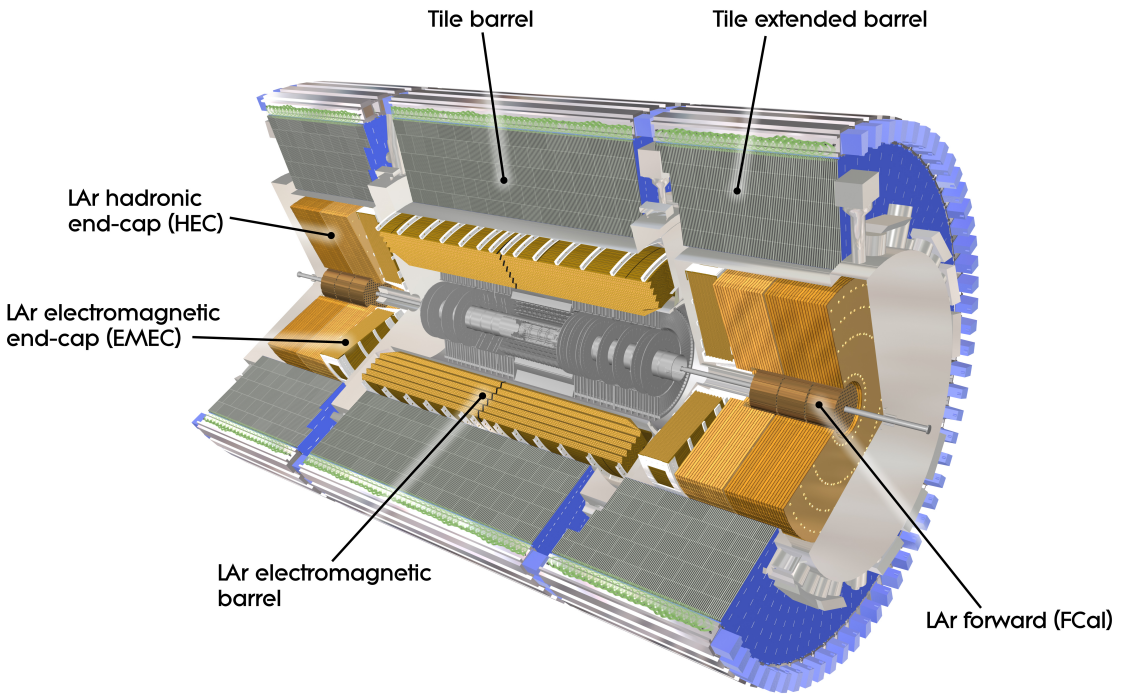

Figure 3.6: Cutaway diagram of the ATLAS calorimeters showing the major components [68].

give an energy measurement. The tile calorimeter uses scintillator tiles as the active medium. These radiate ultraviolet photons when ionising radiation passes through them and the light is collected to give an energy measurement.

The overall calorimeter system is composed of several sub-detectors. Both the electromagnetic and hadronic calorimeters are built with separate barrel calorimeter, end-cap calorimeters, and forward calorimeters. The hadronic calorimeter also has extended barrels that surround the end-caps and forward calorimeters. The electromagnetic calorimeters are all liquid-argon calorimeters and the hadronic calorimeters are made up of tile calorimeters in the barrel and liquid argon calorimeters in the end-caps and the forward regions. In summary, the ATLAS calorimeter system is made up of the EM barrel, the EM end-caps, the tile barrel, the tile extended barrels, the hadronic end-caps, and the forward calorimeters as shown in Figure 3.6.

The systematic uncertainties related to energy deposits reconstructed in the calorimeters will be discussed in Chapter 7.

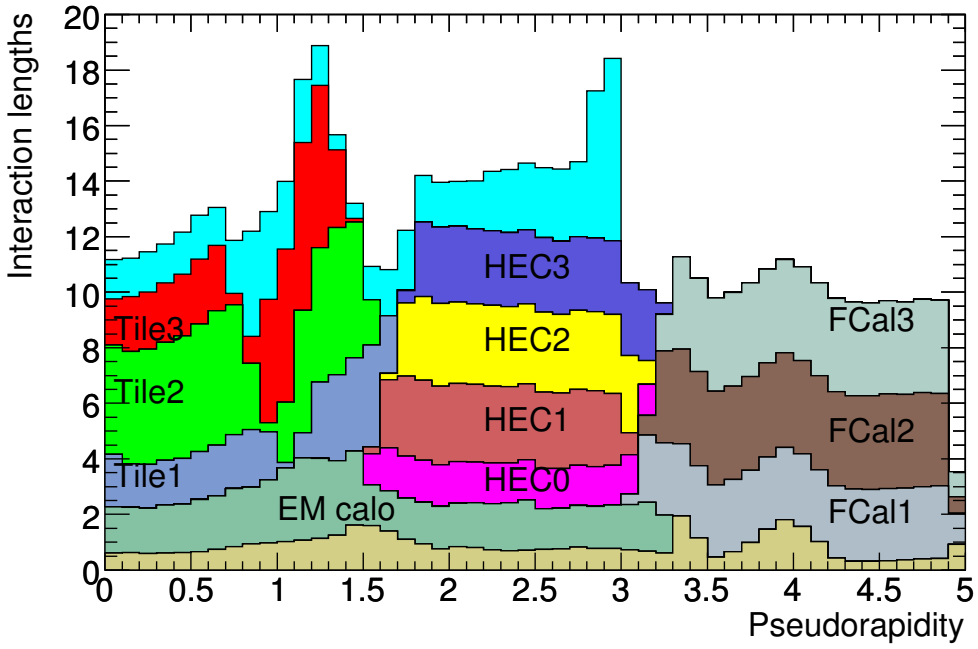

Figure 3.7: The designed cumulative amount of material in units of interaction length in front of and inside the various calorimeters as a function of $|\eta|$. For completeness the total amount of material in front of the EM calorimeter is shown (beige) as well as the total amount of material in front of the first active layer of the muon spectrometer (cyan) [68]. These values increased after 2012 when an insertable layer of pixels was added to the inner detector but the data analysis in this work corresponds to the configuration shown here.

3.4.1 Electromagnetic calorimeter

The electromagnetic calorimeter consists of the barrel ($|\eta| < 1.475$) and the end-caps ($1.375 < |\eta| < 3.2$). All of these are liquid-argon calorimeters and use an accordion-fold geometry that provides full ϕ coverage as shown in Figure 3.8. The absorbers are lead and follow the folds of the accordion shape while the electrodes are placed in the gaps between the sheets in a bath of liquid argon.

These calorimeters are segmented into three layers so that the energy can be measured at three depths in the EM showers. The EM calorimeter is also supplemented with a presampler located outside the solenoid magnet and immediately in front of the EM calorimeter. It measures the energy lost by incident particles before they reach the calorimeter [71] giving a total of four sampling layers.

The calorimeter layers are made up of cells of a constant $\Delta\eta \times \Delta\phi$ where the

granularity of the EM calorimeter cells varies as a function of η and depth. The reconstruction of photons and electrons includes corrections to account for the biases introduced by the granularity of the EM calorimeter cells. The first layer has a granularity of $\Delta\eta \times \Delta\phi = 0.25/8 \times 0.1$ for $|\eta| < 1.4$. The calorimeter layers closer to the beam pipe have smaller cells in $\Delta\eta$ to give better position and direction measurements. The second (and thickest) layer collects the largest fraction of the energy of an electromagnetic shower, and the third layer targets the tail of the shower and therefore has a coarser granularity in $\Delta\eta$ (see Figure 3.9).

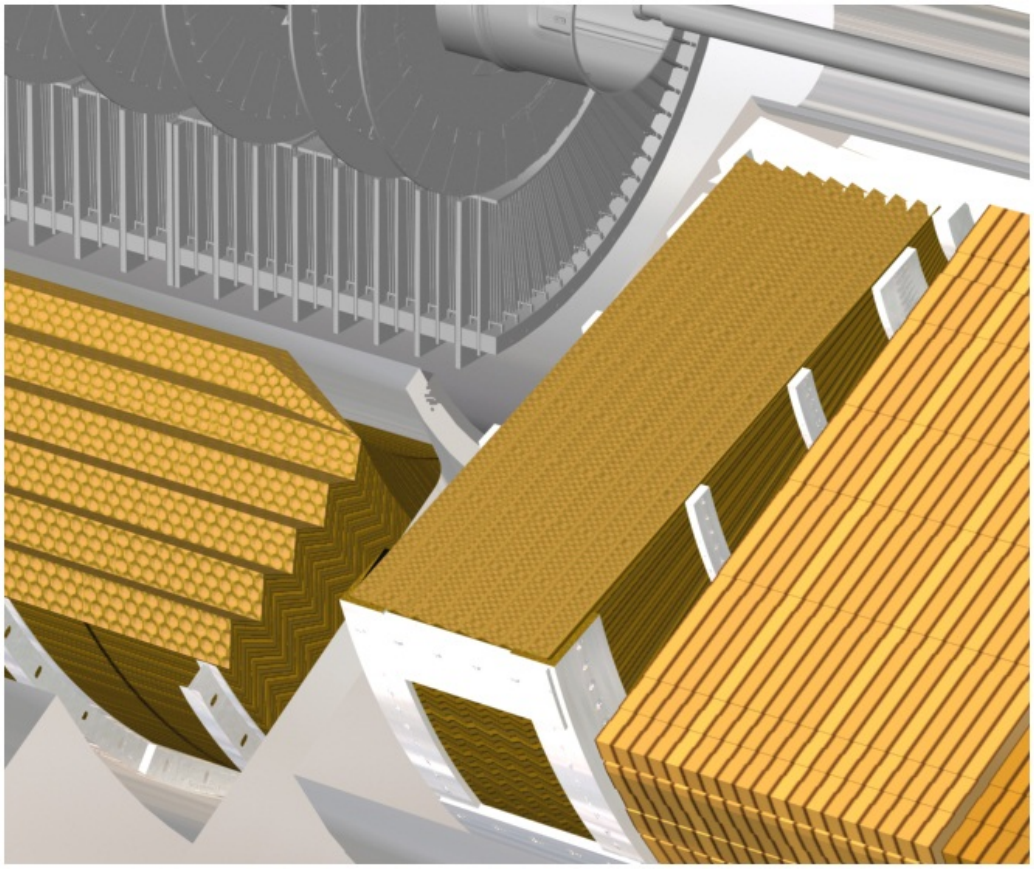

Figure 3.8: Part of the liquid argon calorimeters showing the accordion geometry of both the barrel and the end-caps [68].

The forward calorimeter also has a module for electromagnetic calorimetry and will be discussed in Section 3.4.3.

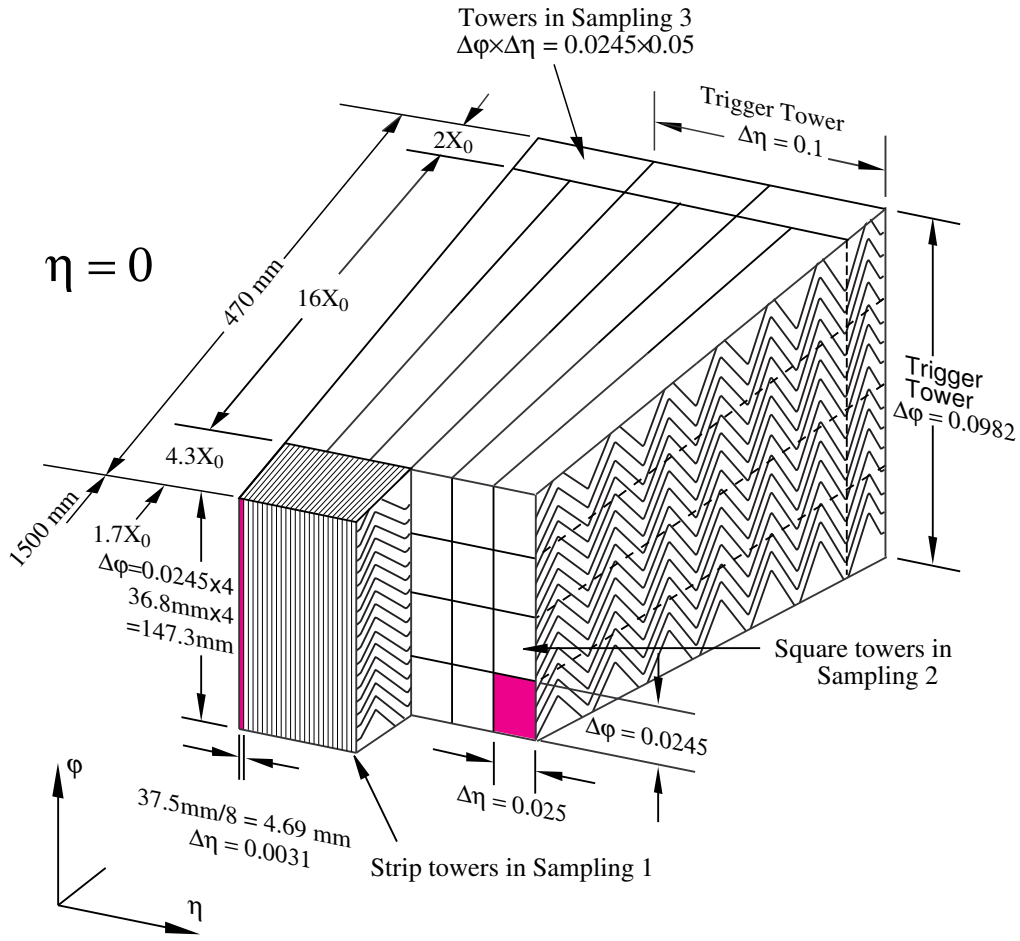

Figure 3.9: A sketch of the electromagnetic calorimeter cell geometry in the barrel region for layers 1, 2, and 3 [68].

3.4.2 Hadronic calorimeter

There are three detectors in ATLAS that perform hadronic calorimetry including the tile calorimeter, the hadronic end-cap calorimeter, and the forward calorimeter. The forward calorimeter will be discussed in Section 3.4.3.

Tile calorimeter

The tile calorimeter is located directly outside the envelope of the EM calorimeter. It is built as a barrel ($|\eta| < 1.0$) and extended-barrel ($0.8 < |\eta| < 1.7$). Unlike the EM calorimeter it uses steel as the absorber and scintillation tiles as the active medium, as shown in Figure 3.10. The absorber-tile pattern is laid out radially and is normal to the beam axis for the full length of the calorimeter. In general, this makes the

tiles themselves not projective in pseudorapidity but the scintillating tile fibres are grouped into the readout photomultiplier tubes (PMTs) so that together as cells there is an approximate projective geometry in pseudorapidity (see Figure 3.11). The tile calorimeter, like the EM calorimeter, is segmented in depth into three readout layers. The fibre groupings make the cell geometry approximately $\Delta\eta \times \Delta\phi = 0.1 \times 0.1$ in the first two layers and $\Delta\eta \times \Delta\phi = 0.2 \times 0.1$ in the outermost layer.

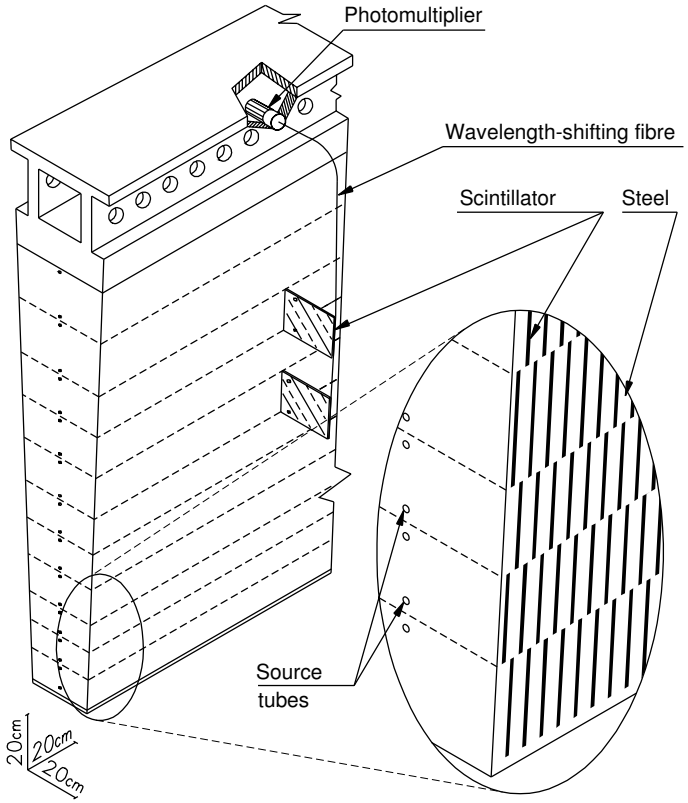

Figure 3.10: A sketch of the tile calorimeter modules [68].

Hadronic end-cap calorimeter

The hadronic end-cap calorimeter is a liquid-argon sampling calorimeter with a cylindrical shape, and covers $1.5 < |\eta| < 3.2$. It is in some ways similar to the EM calorimeter but it does not share the same accordion geometry. The hadronic end-cap calorimeters use plates of the absorber material, copper, with liquid argon in the gaps between them. These are assembled into wheels (two wheels per end-cap), which are placed face-to-face along the z axis (see Figure 3.12). Each wheel contains two layers making a total of four readout layers per hadronic end-cap. Like a pizza, each wheel

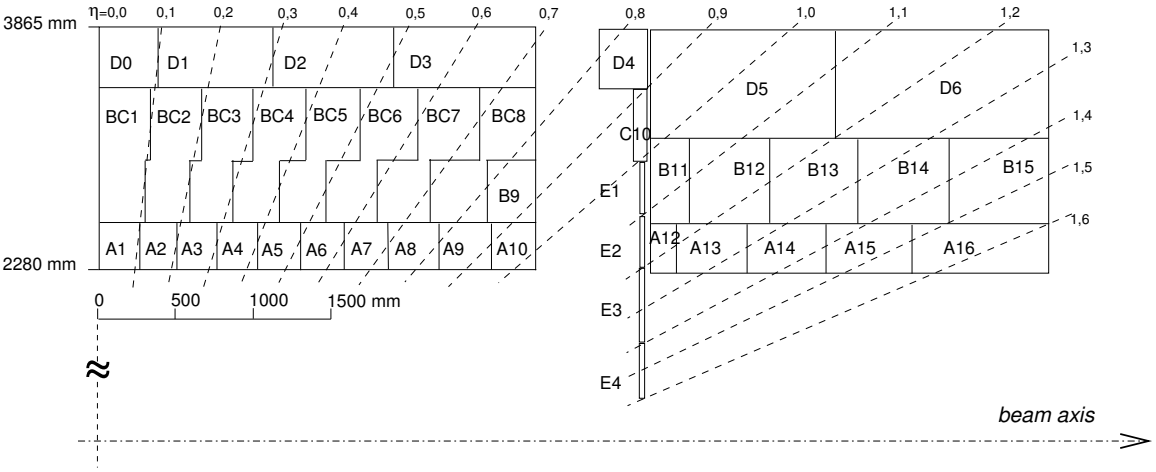

Figure 3.11: A sketch of the tile calorimeter readout fibre groupings used to create the approximately projective geometry in pseudorapidity [68].

is made up of (32) identical wedge-shaped modules that together encompass the full 2π of ϕ, as shown in Figure 3.13. The front wheels have 24 absorber plates, each 25 mm thick, and a 12.5 mm thick front plate. The rear wheels provide a coarser measurement with only 16 absorber plates, each 50 mm thick, and a 25 mm thick front plate. The gaps between the plates are all 8.5 mm wide, and contain four liquid argon drift zones (1.8 mm wide) and three layers of readout electrodes, as shown in Figure 3.14.

3.4.3 Forward calorimeter

The forward calorimeter, a liquid-argon calorimeter, is slightly different from the other calorimeters in that it has a module for electromagnetic calorimetry and two modules for hadronic calorimetry. The innermost module is made with copper as the absorber and is primarily designed for EM measurements. The outer two modules are made with tungsten as the absorber and measure predominantly the hadronic interactions. As the forward calorimeters are located very far forward in ATLAS ($3.1 < |\eta| < 4.9$), they are exposed to a very large flux of particles [68].

The light charged leptons and jets explicitly used in this analysis are required to be more central than the pseudorapidity coverage of the forward calorimeters (see Section 4.2). The forward calorimeters are used mainly in the measurement of the missing energy in the event.

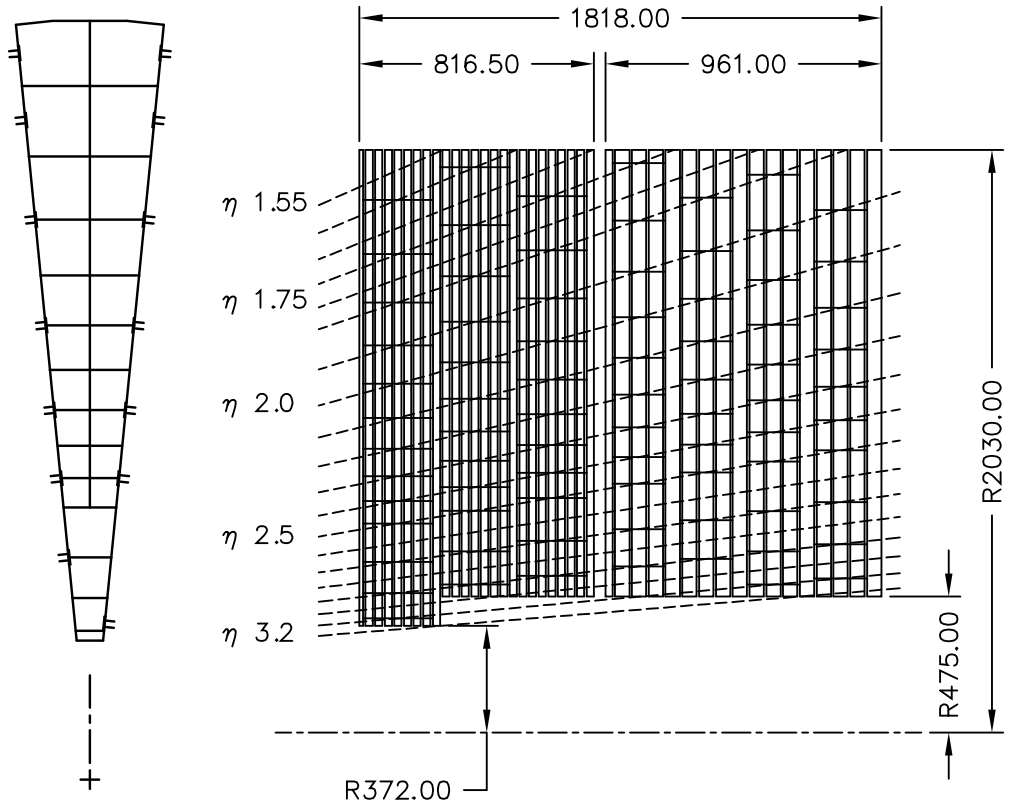

(a) HEC: $r - \phi$ (b) HEC: $r - z$

Figure 3.12: Sketch of the hadronic end-cap calorimeter geometry as seen from two different views [68]. In Figure 3.12b the semi-pointing layout of the readout electrodes in η is indicated by the dashed lines.

3.5 Muon spectrometer and toroidal magnets

The ATLAS muon spectrometer was designed to give ATLAS "good muon identification and momentum resolution over a wide range of momenta and the ability to determine unambiguously the charge of high-p_{T} muons [68]." To accomplish this the muon spectrometer makes use of four different types of detectors: monitored drift tubes (MDTs), thin gap chambers (TGCs), resistive plate chambers (RPCs), and cathode strip chambers (CSCs) as depicted in Figure 3.15. Three large superconducting air-core toroid magnets, shown in Figure 3.16 are used to deflect the muons and enable the measurement of their charges and momenta. The MDTs and CSCs are used for precision momentum measurements while the RPCs and TGCs are used for triggering.

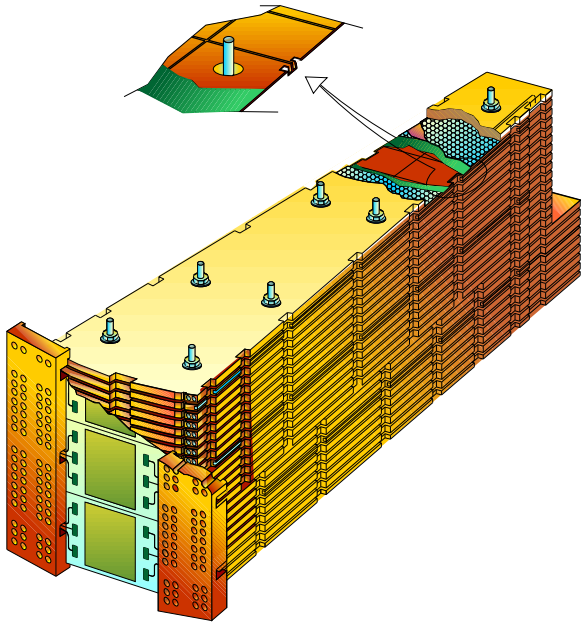

Figure 3.13: A sketch of one the hadronic end-cap modules [68].

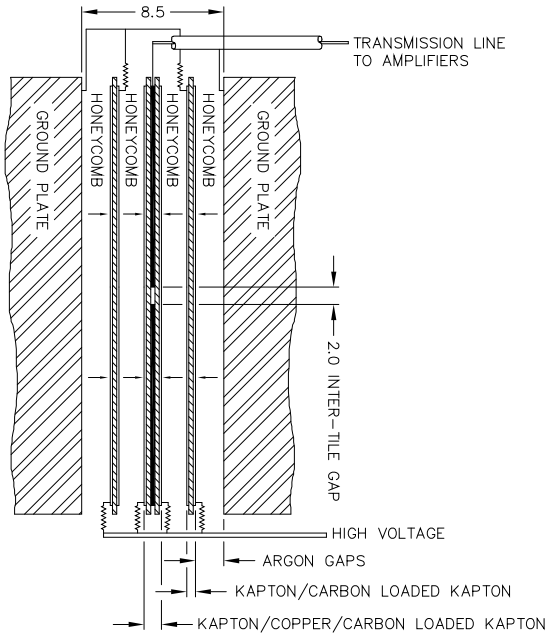

Figure 3.14: A sketch of the hadronic end-cap readout structure [68].

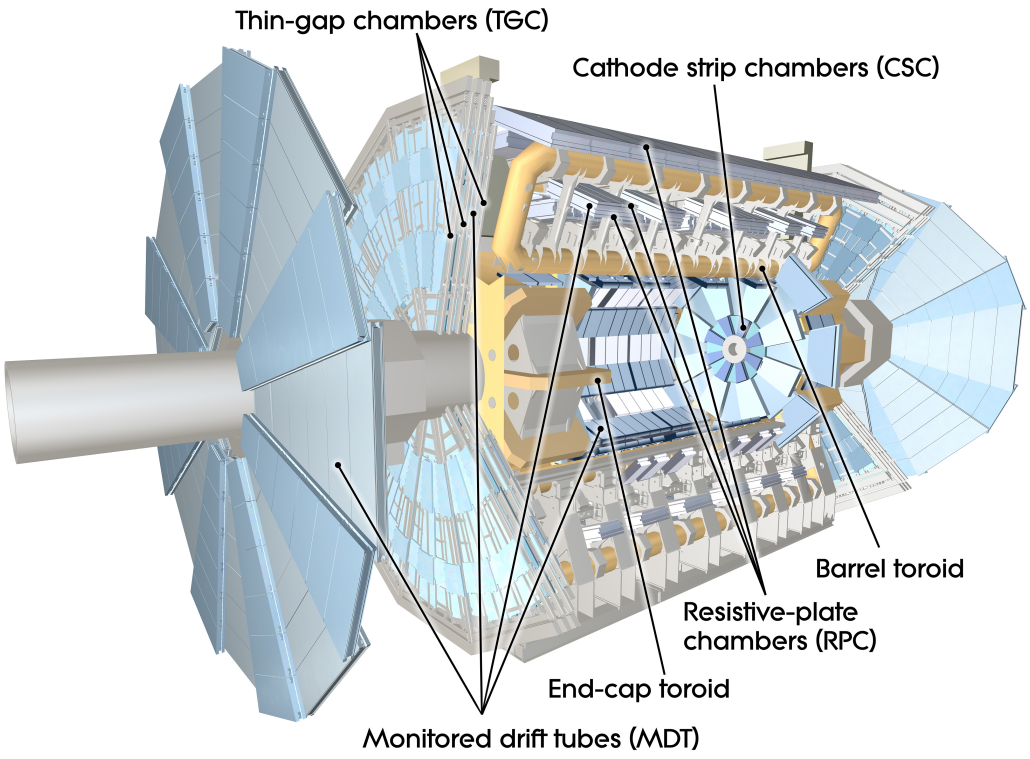

Figure 3.15: Cutaway diagram of the ATLAS muon spectrometer showing its major components [68].

3.5.1 Toroidal magnets and detector layout

The muon spectrometer gives an improved muon momentum measurement over using just the ATLAS inner detector and the toroids are especially beneficial for high momentum muons in the forward regions where solenoids in general are less effective. Muons in the forward regions travel very close to the direction of the field of the solenoid and so are not affected much by it. The ATLAS toroids were designed so that the magnetic field is roughly perpendicular to the trajectory of the muons and the bending of the muon tracks is in the r-z plane. The central solenoid bends the tracks in r-ϕ so the direction of the bending of the muons in the inner detector is orthogonal to the direction of the bending of the muons in the muon spectrometer. The air-core design minimises the amount of material that the muons traverse and so minimises the resolution loss due to multiple scattering.

Each of the three toroidal magnets is made up of eight flat coils assembled radially and symmetrically around the z-axis ($0 < |\eta| < 2.7$). The magnetic field they produce is approximately perpendicular to the trajectory of the muons as indicated in Figure

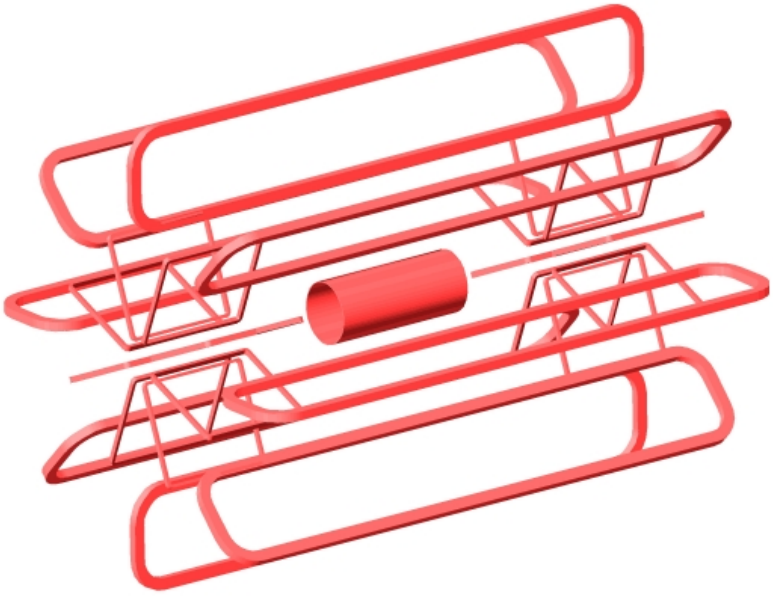

Figure 3.16: The ATLAS magnets: the solenoid, the barrel toroid, and the end-cap toroids [72].

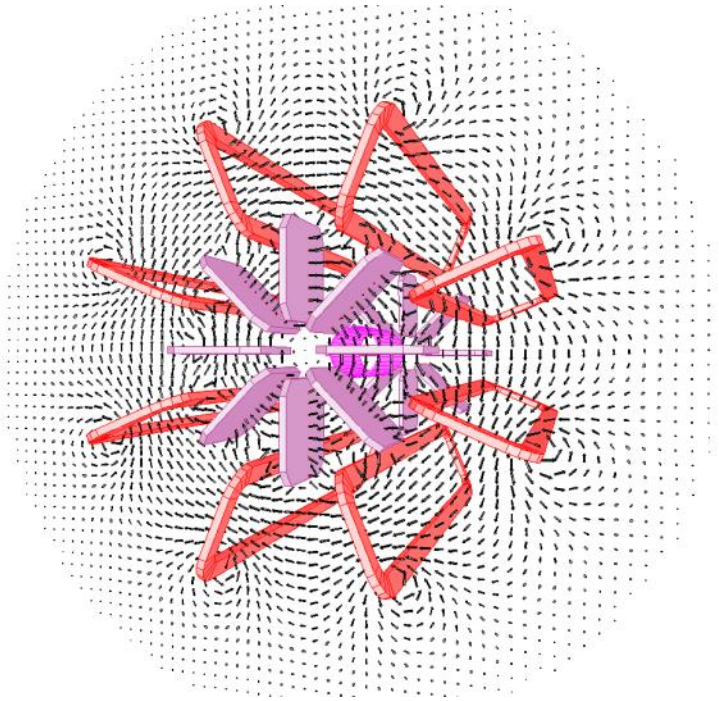

Figure 3.17: The magnetic field lines within an x-y plane [73].

3.17. The toroidal magnetic field varies with position. In the barrel the field varies from 0.15 T to 2.5 T with an average of approximately 0.5 T. In the end-cap toroids

the field ranges from 0.2 T to 3.5 T [68].

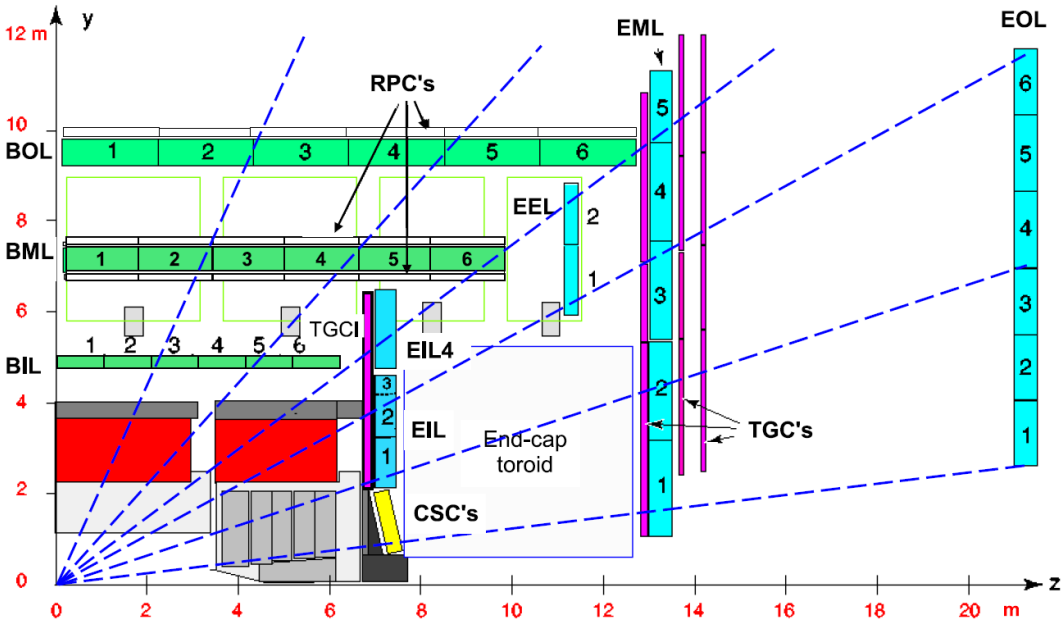

Figure 3.18: Layout of the muon spectrometer. The Barrel Inner, Middle, and Outer Layers, and the End-cap Inner, Extra, Middle, and Outer Layers are labelled for the MDTs. The general positions of the CSCs, RPCs, and TGCs are shown [68].

The muon spectrometer is located outside of the calorimeters. The muon spectrometer detectors are mostly grouped into three stations where each station is made up of several detector layers. There are large spaces between the stations to allow muons from the interaction point to deviate a substantial distance from a straight line trajectory in the magnetic field of the toroids. As shown in Figure 3.18 the chambers are arranged to form three concentric cylinders around the beam axis in the barrel region and in the end-cap regions the chambers are arranged in wheels that are perpendicular to the z-axis [74]. In both the barrel and the end-cap regions, the inner stations are situated in a location where the muons will traverse a station before entering the toroid magnets, and the outer stations are situated in a location where the muons will have already traversed the toroid magnets before traversing the stations. In the barrel the middle station is situated within the barrel toroid magnet field while in the end-cap regions the middle station is outside of the toroid magnets like the outer stations.

Detector modules overlap to avoid gaps in the detector coverage. Some regions of the muon spectrometer have lower acceptance because they are left uninstrumented

to allow space for the detector's support infrastructure or services to the detectors and solenoid within. The relative sizes and layout of the wheels mean that it is possible for a track to pass through only two stations for some specific track η and momenta. To make sure that all tracks in the end-cap regions pass through at least three stations, an extra ring of detectors (which was not yet fully installed in 2012 when the data used for this analysis were collected) is placed between the inner and middle wheels (EEL in Figure 3.18).

The MDTs and CSCs are used to take precision measurements of the coordinates of track hits in the bending direction of the toroidal magnet (z in the barrel and r in the end-cap regions) and therefore give the muon momentum measurement ($|\eta| < 2.7$). The RPCs and TGCs are used for both triggering ($|\eta| < 2.4$) and measuring the track hit coordinates in the direction orthogonal to the precision measurement coordinate and approximately parallel to the magnetic field, the ϕ coordinate. The third position coordinate is known from the detector position.

3.5.2 Monitored drift tubes (MDTs)

The monitored drift tubes are the main precision measurement detectors in the muon spectrometer. They cover the range $|\eta| < 2.7$ except in the innermost end-cap layer where they cover $|\eta| < 2.0$. A single monitored drift tube is conceptually similar to a straw tube of the TRT in the inner detector (see Section 3.3.2). The MDTs are monitored so that temperature-induced changes affecting their size and geometry can be taken into account in particle reconstruction.

In the barrel region the chambers are arranged in three concentric cylinders, so that particles will pass through the inner, middle and outer stations. In the end-caps the MDTs are arranged in three disks. The average muon travelling outwards from the centre of the detector will traverse 8 tubes in the inner station, 6 tubes in the middle station, and 6 tubes in the outer station totalling 20 MDT hits. The number of MDTs in each station allows for the muon trajectory to be reconstructed separately in each station.

3.5.3 Cathode strip chambers (CSCs)

The cathode strip chambers are multiwire proportional chambers used for precision position measurements in the high η region of the detector ($2 < |\eta| < 2.7$). In the very forward regions of ATLAS there is a large flux of particles, too large for the

MDTs. The CSCs replace the MDTs in the area close to the beam pipe in the innermost station in each end-cap. These detectors were chosen to be used in this region because of their high rate capacity along with their good time, spatial and double track resolution [68]. The geometry includes two cathode planes with a plane of anode wires between them. Both cathode planes are instrumented with strips, where the strips on one cathode plane are orthogonal to the strips on the other cathode plane. Only the signals from the strips are read out. The CSCs are tilted so that the detector faces are orthogonal to the particle trajectories.

3.5.4 Resistive plate chambers (RPCs)

The resistive plate chambers are the triggering detectors of the muon spectrometer used in the barrel region $|\eta| < 1.05$. The RPCs are gaseous detectors and have two planes of strips: a cathode and an anode. The two sets of strips are orthogonal to each other. RPC modules are constructed with two layers and are referred to as doublets. The RPCs are mounted on common supports with the middle and outer MDTs, which only measure the z coordinate of tracks in the barrel region. The RPCs provide the missing ϕ coordinate measurements and a coarse z measurement for matching to MDT hits [68].

3.5.5 Thin gap chambers (TGCs)

The thin gap chambers ($1.05 < |\eta| < 2.4$) are mounted as wheels in the end-caps. They are used for triggering and measuring the track hit ϕ coordinates to complement the MDT precision position measurements. TGCs are multiwire proportional chambers like the CSCs. One cathode plane is segmented into strips while the wires run orthogonal to the strips. The ganged wires provide the r measurements for matching to MDT hits while the strips provide the ϕ measurements. The TGC modules are built with two or three layers together and are referred to as doublets and triplets respectively.

Chapter 4

Triggering and reconstruction

Before any full physics analysis can be performed on the LHC collision data several important procedures must take place. Firstly, during the data taking the ATLAS trigger selects which events to save to disk [75]. Secondly, the low-level data are reconstructed into the particles, jets, and missing energy that are explicitly used by the physics analyses.

The manners in which triggering and reconstruction are performed are constantly changing as problems with software or hardware are found and fixed, software and hardware upgrades are implemented, and adaptations are made to the different collision settings. In this chapter the triggering and reconstruction will be discussed as pertaining to the 2012 data set used for this analysis. [1]

4.1 Triggering

The LHC is designed to run with up to 2808 proton bunches per beam and to collide them at a nominal rate of 40 MHz with a nominal bunch spacing of 25 ns. Only a fraction of the data can be saved to disk so a triggering system is used to control the frequency of different types of events being saved to disk. The triggering system is also used to manage deadtime. Deadtime is imposed when the triggering system vetos full events to manage the event rates [76]. A different form of deadtime is managed instead by the detector readout electronics. When individual channels are hit they become insensitive to future hits while the leftover signal dissipates. Deadtime

[1] Changes made since 2012, which do not affect this analysis, are beyond the scope of this work. The present tense will be used throughout this chapter for ease of reading.

is imposed on the channel by temporarily masking it to avoid leftover signals being incorrectly identified as a new signal [68].

4.1.1 The trigger system

The ATLAS triggering system is extremely important to the ability of the experiment to filter and record data. The triggering system is necessary to reduce the data saving rate to affordable levels and to be able to manage the detector deadtime. The event size times data taking rate is so large that that monetary cost is too great to save all the events to disk. The trigger saves to disk as many of the rare hard scattering events as possible while throwing away the vast majority of the less rare events. The probability for a given type of event to be saved to disk is set by the experiment via the trigger menu.

There are three levels to the ATLAS trigger: Level-1 (L1), Level-2 (L2), and the Event Filter (EF) [68]. The Level-1 trigger was designed to reduce the event rate from 40 MHz to 75 kHz. The L2 trigger was designed to reduce this to below 3.5 kHz and the Event Filter designed to reduce it to the final rate of about 200 Hz, the rate at which the data are written to disk [77, 78]. In the actual operation of the experiment these rates are larger than the original design rates and varied and changed over short and long time scales. If the event does not pass any of the triggers at any level then the event is thrown away and lost forever.

The Level-1 trigger is based on custom-built electronics and uses information from the calorimeters and the muon spectrometer (but not the inner detector) to select events to pass to the Level-2 trigger [77]. It searches for signatures of high-p_{T} muons, electrons, photons, jets, and tau leptons decaying into hadrons. The L1 trigger also searches for large total transverse energy and large missing transverse energy [68]. For each event, the L1 trigger creates one or more regions of interest (ROI), which contain information on the type of features identified and the criteria that caused the ROI to be formed. The ROI are then passed on to the Level-2 trigger.

The L2 trigger uses all the available data in the ROI at full granularity and precision, and uses fast algorithms to reconstruct inner detector tracks in them. A single ROI used by the Level-2 trigger contains approximately 2% of all the data in the event [68]. The Event Filter uses the full event to determine whether or not to select the event. The Level-2 reconstruction is done in a fast but simplified way but the Event Filter reconstruction is done in a very similar way to the offline reconstruction

with many of the same tools being used except when they are far too computationally heavy and slow [79]. The simplified reconstructions of the events are used so that the triggers can use the data from the full event while also ensuring that the trigger runs quickly enough to keep up with the LHC collision rate. The Event Filter has access to the inner detector for reconstruction which means that particle identification is significantly enhanced over the Level-1 reconstruction where the inner detector information was not available [79]. The L2 trigger and the Event Filter are collectively referred to as the High Level Trigger (HLT) and they are based almost entirely on commercially available computers and networking hardware.

During a data-taking run, most of the trigger settings cannot be changed, except for a few specific items like the trigger prescale factors. A prescale factor (or just "prescale"), PS, is a number that tells the trigger how frequently it should accept a particular trigger. If a trigger has a prescale of n then that trigger is given a probability of passing of $1/n$ on an event where the trigger would otherwise be accepted. This is used to selectively reduce the rate of the common events that swamp the interesting rare processes. All the triggers used in this analysis are "unprescaled" ($n = 1$).

4.1.2 Electron and muon triggers

Two types of triggers (or "trigger chains") are used in this analysis: electron triggers and muon triggers. A trigger chain is the path through the L1, L2, and EF triggers of interest. The full chain is important because the prescale factors can be independently applied at each trigger level and an event cannot be studied by the higher level triggers unless it first passes the lower-level triggers in the chain.

Electron triggers

The L1 trigger used to trigger on electrons is part of the L1 calorimeter trigger. The level-1 trigger has to work quickly so the L1 calorimeter selections are made using reduced-granularity information from all of the calorimeters. It searches for indications of objects with high transverse energy such as electrons, photons, jets, tau leptons decaying into hadrons, and events with large missing transverse energy. The trigger separates these tasks into searches for hadronic energy deposits and searches for electromagnetic energy deposits. The Level-1 calorimeter trigger does not attempt to distinguish an electron from a photon [78].

The trigger cells of the L1 electromagnetic triggers are summed using analogue

electronics to make "trigger towers" that cover the full depth of the calorimeter and are 0.1×0.1 in $\Delta\eta \times \Delta\phi$. The $\Delta\eta \times \Delta\phi$ size is larger in the end-caps and the forward calorimeter where the detector geometry is less projective [80]. The trigger tower readout is then converted into transverse energies and a sliding-window clustering algorithm is used to locate concentrations of high E_{T} energy deposits. The sliding window is of size 4×4 trigger towers ($\eta \times \phi$) and two towers deep (one EM calorimeter trigger tower plus one hadronic calorimeter trigger tower) as shown in Figure 4.1. Within each window several energy thresholds are placed on the summed E_{T} of different combinations of trigger towers to reduce backgrounds and to enforce various types of isolation. The values of these thresholds are specific to each trigger defined in the Level-1 trigger menu.

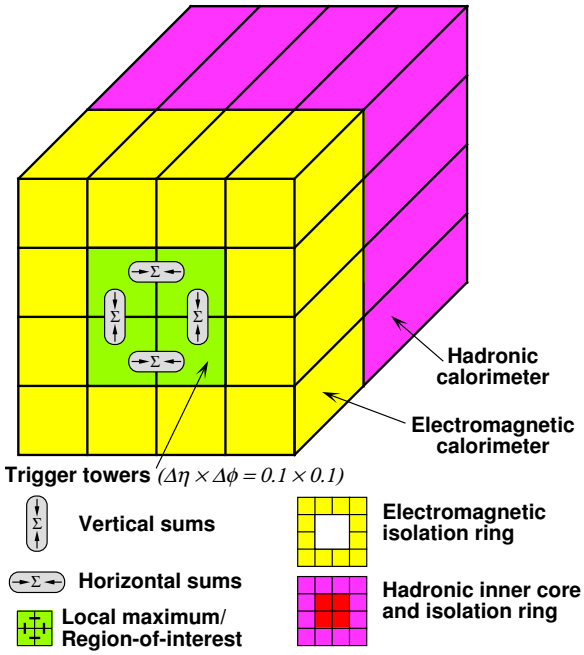

Figure 4.1: Sketch of the calorimeter trigger towers. These towers are used by the electron trigger to identify electromagnetic energy deposits [68].

Events passing the Level-1 trigger are then studied in more detail by the High Level Trigger. The Level-2 and Event Filter triggers study the energy deposits using clusters of individual cells in individual calorimeter layers [79]. Once an energy deposit is determined to be electromagnetic, further work is done to match it to a track to form an electron [81] (or a photon if there is no matching track). The L2 trigger uses simplified reconstruction while the EF reconstruction is much closer to the offline reconstruction (see Section 4.2). If the event passes the EF (including prescale factors

and deadtime) then it is saved to disk for use in analyses.

Muon triggers

At Level-1, high-p_{T} muons are identified using the RPCs (barrel) and TGCs (end-caps) in the muon spectrometer (see Section 3.5). The Level-1 muon trigger searches for hit patterns that are indicative of high-p_{T} muons originating from the interaction region [68]. It processes the raw data from the muon spectrometer and calculates the total muon multiplicities for the different p_{T} thresholds while ensuring there is no double counting of muons traversing more than one detector region [68, 82].

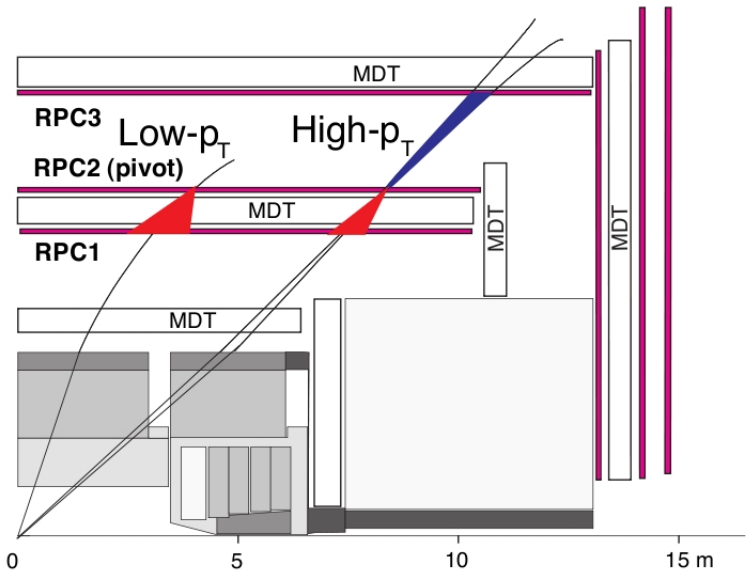

Figure 4.2: The RPC doublets with example low-p_{T} and high-p_{T} coincidence windows for the muon trigger [68].

In the muon spectrometer there are at least tens of centimetres of separation between each of the three groups of trigger detector layers, as shown in Figure 3.15. Each of these groups has three or four layers of triggering detectors (two doublets or a triplet). The L1 muon trigger searches for detector hit patterns in a coincidence window, as shown by the red and blue "triangles" in Figure 4.2. The number of detector hits required is a function of the p_{T} of the muon trigger threshold [68]. The width of the coincidence window also depends on the p_{T} threshold of the trigger: the larger the coincidence window, the smaller the p_{T} threshold. The coincidence window size also depends on other factors like the magnetic field, and the expected amount of

multiple scattering in the calorimeters. The exact sizes were determined using Monte Carlo simulations [78].

The Level-2 and Event Filter triggers [83] use increasingly more complex and slower tools to reconstruct the muons. Muon spectrometer hits (only in an ROI at Level-2) are reconstructed into stand-alone muon tracks and combined with tracks formed from inner detector hits to make the muon candidates [74]. At the Event Filter level muon candidates are reconstructed using tools similar to those used in the offline reconstruction, which will be discussed in Section 4.2. If the event passes the Event Filter (including prescale factors and deadtime) then it is saved to disk for analyses to use.

4.2 Reconstruction

Before any particle physics analyses can be performed the raw data have to be reconstructed. The tracking detector hits and calorimeter cell energies are combined to build the particle tracks and energy clusters, respectively. These are then used to reconstruct photons, charged leptons, jets, and missing transverse energy.

Inner detector tracks

The tracks of charged particles with $p_{\mathrm{T}} > 0.5$ GeV and $|\eta| < 2.5$ are reconstructed and measured in the inner detector and magnetic field generated by the solenoid [68]. The reconstruction process in the inner detector can be divided into three steps. First, in the pre-processing stage, raw data (electric charges and currents) from the pixel and SCT trackers (see Section 3.3.1) are converted into clusters of signal information. A cluster of sensor information is used because the hit position resolution improves if the signal is deposited over several pixel (or SCT) sensors. The data from the SCTs has to be clustered because two silicon microstrips are required to measure the third coordinate. The raw data from the TRT (see Section 3.3.2) are converted into drift circles where a drift circle is the radial distance of the track from the central anode wire. In the track-finding stage, partial tracks are formed using the hits in the first few silicon detector layers closest to the beam pipe. The track fits are cleaned by removing outlying hits to reject fake tracks. The data are then refitted and these steps are iterated by including more hits and then drift circles until the final track candidates are created.

Muon spectrometer tracks

The reconstruction process in the muon spectrometer can be separated into four steps: pre-processing, pattern-finding and segment making, segment combining, and track-fitting [68]. In the first step the raw data are used to form drift circles in the MDTs and clusters in the CSCs, RPCs, and TGCs (see Section 3.5). Track segments are built by making short track fits within single MDT or CSC stations. Fully fledged track candidates are built from track segments and the final track fitting takes into account the material that the muons traversed and the inhomogeneities of the magnetic field along the muon trajectories.

Calorimeter energy deposits

Different types of particles leave energy deposits in the calorimeters with different characteristic patterns, for example electrons deposit most of their energy in the EM calorimeter while charged pions interact moderately in the EM calorimeter but predominantly in the hadronic calorimeter. An energy deposit left by a particle in the calorimeters is typically grouped together spatially across several cells and thus is usually reconstructed as a cluster in the different calorimeter layers. The $\Delta\eta \times \Delta\phi$ size of a cluster can vary depending on the type of particle being reconstructed, and where in the calorimeter the cluster is located. Measuring the energy of the clusters in three dimensions requires the summation of the energies in all the associated calorimeter cells while also including special corrections to account for the sampling nature of the calorimeters, longitudinal and lateral energy leakage out of the cluster/calorimeter, and energy deposited in the material in front of the EM calorimeter.

The energy clusters used to reconstruct photons and electrons are typically just rectangular groups of cells defined by N cells in $\Delta\eta$ and M cells in $\Delta\phi$. The cluster sizes for electrons and photons are set to be $N \times M = 3 \times 5$, 5×5, or 3×7, depending on the η of energy deposits and the presumed particle identity.

The energy clusters used in jet reconstruction are more complicated than those used to reconstruct electrons because jets are made up of a collection of particles. In a jet there can be large overlaps between the showers of adjacent particles in the jet and as a result it is very difficult to identify an energy deposit as being only from one specific particle. At the same time the interaction length of hadrons can be large making it also possible for a single particle to produce several physically separated energy deposits.

The energy clusters left by the particles in jets are reconstructed as topological clusters (or "topoclusters"). The clustering algorithm adds physically adjacent cells to the cluster if the cell's energy significance meets certain specific requirements. For jets, it is generally intended that there should be approximately one particle associated to each of these three-dimensional groupings of cells. The clustering energy thresholds are set such that a single charged pion results most commonly in three topoclusters and a single neutral pion results most commonly in one topocluster [84]. The average ATLAS proton-proton event is composed of a few hundred topoclusters with the exact number varying widely as a function of the pile-up.

4.2.1 Vertices

Individual proton-proton collisions in each event can be partially reconstructed as vertices formed by tracks in the inner detector. The primary hard scattering proton-proton collision is identified as the vertex with the highest scalar sum of the squared transverse momentum of the tracks associated to it, Σp_{T}^2 [85]. This vertex is labelled the primary vertex. The primary vertex is required to have at least five tracks with $p_{\mathrm{T}} > 500$ MeV.

4.2.2 Jets

A jet is a collection of (usually) nearby particles with a common origin and is produced by the hadronisation of a gluon or a quark. The LHC is a hadron collider so there are usually a large number of jets in each ATLAS event. Algorithms are required to determine which particles should be part of which jet or if they should be part of a jet at all. In ATLAS the anti-k_t algorithm [86] is used to assign topological clusters to jets. This algorithm takes as input a "radius" parameter and tends to form approximately conically shaped jets in $\eta \times \phi$.

For this analysis the radius parameter for the jets is set to $R = 0.4$ and all jet candidates are required to have $p_{\mathrm{T}} > 20$ GeV and $|\eta| < 2.5$. The radius parameter gives an approximate maximum radius for the jet where a radius is defined as $\sqrt{\Delta y^2 + \Delta\phi^2}$ and y is the rapidity. Events containing jets likely to have arisen from detector noise, cosmic radiation, or beam backgrounds are removed [87]. Events are also removed if they fail to meet various jet quality criteria. These event vetoes are applied to a looser selection of the jet candidates with $|\eta| < 2.8$.

Jets that have $p_{\mathrm{T}} < 50$ GeV and $|\eta| < 2.4$ are required to have a "jet vertex fraction" above 0.5 to ensure that the jet originates from the hard scatter collision rather than from pile-up. The jet vertex fraction is defined as the sum of the p_{T} of the tracks associated to the jet and also associated to the primary vertex, divided by the sum of the p_{T} of all the tracks associated to the jet.

Topoclusters are by default reconstructed assuming only electromagnetic interactions and neglecting the calorimeter response to hadrons. Jets are reconstructed using a set of topoclusters that are calibrated to the calorimeter response to hadrons using the local cell signal weighting (LCW) method [84]. It is important for the topoclusters to be calibrated to hadrons because hadrons can interact via the electromagnetic interaction as well as the strong interaction, and the ATLAS calorimeters have different responses to the two types of interactions. Some energy deposits from hadrons are invisible because the energy is absorbed in nuclear reactions, which does not happen with electromagnetic interactions and so a calorimeter does not naturally respond to the two different types of interactions in the same way. The ATLAS calorimeter responses to these two types of interactions as a function of energy are different from each other and so the reconstruction has to accommodate the differences. Other calibrations are applied to the full jets to correct for pile-up, to align the jet direction with respect to the primary vertex, to calibrate the jet energy and η, and to correct for diffences between data and simulations (to be discussed in Chapter 5) [88]. These jet calibrations make up the "jet energy scale" (JES) calibration [89]. The calibrations include corrections based on simulations, corrections based on the data, and corrections based on comparisons between the data and the simulations. The energy scale calibrations can be recursive as well in that the low-momentum jets may be calibrated with respect to $Z \to ee$ decays and then higher momentum jets are calibrated with respect to low-momentum jets. More details on the jet energy scale are given in Chapter 7.

The systematic uncertainties related to jets will be discussed in Chapter 7.

b-tagging

It is a non-trivial task to identify a jet in ATLAS as having originated from a gluon or a specific quark flavour; however, the ability to tag a jet candidate as having arisen from a specific flavour of heavy quark can be very beneficial. The jet candidates meeting the selection requirements specified in Section 4.2.2 as well as $|\eta| < 2.5$ are

analysed by a multivariate algorithm to identify jet candidates that originated from a b-quark. A jet originating from a b-quark will contain a b-hadron, which is much shorter lived than charged pions, and will travel a short but measurable distance inside the beam pipe before decaying and producing more tracks originating from this secondary vertex ($c\tau \sim 10^{-4}$ m). The b-tagging algorithm identifies b-jets by utilising the impact parameters of tracks, secondary vertex reconstruction, and the topology of b-hadron and c-hadron decays inside jets [68]. The impact parameters of a track are the longitudinal (z) and lateral (r) positions of the point of closest approach of the track to a specific vertex, usually the primary vertex.

The algorithm determines a single "b-tagging weight" per jet. This quantity is an estimate of the probability that the jet originated from the decay of a b-hadron. The algorithm has several working points with different levels of b-jet tagging efficiency balanced against the inefficiency of mis-identifying a jet as a b-jet. Each working point uses a different cut on the b-tagging weight. The working point used for this analysis has a 70% efficiency for tagging b-jets and rejection factors of 5 and 137 against b-tagging a c-quark jet and a light-quark or gluon jet respectively [90, 91].

The systematic uncertainties related to b-tagging will be discussed in Chapter 7.

4.2.3 Electrons and photons

The reconstruction of an electron candidate requires the matching of an energy cluster in the EM calorimeter to an inner detector track. An EM cluster size in $\Delta\eta \times \Delta\phi$ varies at different stages of the reconstruction process and in different regions of the detector. Typically it is formed by the combination of over 50 cells. Various quantities are used to measure the quality of the cluster-track matching including the ratio of the energy in the EM cluster to the momentum of the track, and the difference in the η and ϕ positions of the EM cluster in the second layer of the calorimeter and the η and ϕ positions of an associated track extrapolated to the point it would hit the calorimeter layer. These quantities and others including the lateral and longitudinal shower shapes in the EM cluster and the number of inner detector hits are used to select electron candidates with different levels of identification efficiency and rejection power for jets being mistaken as electrons [92]. Three working points are used for the identification: *loose*, *medium*, and *tight*. The *tight* selection has the most strict levels of background rejection and the *loose* selection the least. The *tight* selection is a subset of the *medium* and *loose* selections, while the *medium* selection is a subset of

the *loose* selection; thus the *loose* selection has the highest identification efficiency of the three working points. With the increasing level of tightness of the working points more variables are added and the cuts are tightened on the variables already used in the looser selections [93, 94]. The electron identification efficiencies are about 95%, 91% and 80% for the *loose*, *medium* and *tight* working points respectively. The final energy of the electrons used in this analysis comes entirely from the calorimeter energy measurements while the η and ϕ directions come from the associated track [94].

The electron candidates used in the electron-hadron analysis are required to satisfy the *tight* selection quality criteria, have $p_{\mathrm{T}} > 25$ GeV, $|\eta| < 2.47$ and longitudinal and transverse impact parameters within 2 mm and 1 mm of the primary vertex, respectively. The electrons must also be isolated within the tracking volume following the requirement that the scalar sum, Σp_{T}, of the p_{T} of inner detector tracks within a cone of size $\Delta R \equiv \sqrt{(\Delta\eta)^2 + (\Delta\phi)^2} = 0.2$ around the electron candidate, be less than 10% of the electron p_{T}. The tracks involved in this isolation requirement are matched to the primary vertex, do not include the main electron track, and must have a $p_{\mathrm{T}} > 1$ GeV.

The systematic uncertainties related to electrons will be discussed in Chapter 7.

Photon candidates are identified as EM calorimeter deposits consistent with a photon and with no associated inner detector track. Photons are not explicitly used in this analysis and their reconstruction is beyond the scope of this document.

4.2.4 Muons

The ATLAS experiment uses the information from the inner detector and muon spectrometer to reconstruct muons. To a lesser extent, information from the calorimeters is also used. Muon candidates are reconstructed using the STACO algorithm [95]. They are identified by combining tracks in the inner detector with tracks in the muon spectrometer. The muon reconstruction requires specific minimum numbers of pixel, SCT, TRT, and muon spectrometer sub-detector hits. The muons explicitly used in this analysis are required to traverse the inner detector, however muon candidates reconstructed in $2.5 < |\eta| < 2.7$ where there is muon spectrometer coverage but not inner detector coverage are used for the calculation of missing transverse momentum (see Section 4.2.6).

The combination of an inner detector track and a muon spectrometer track re-

quires a correction for the energy lost by the muon in the region between, which is largely instrumented with calorimeters. A muon typically loses about 3 GeV of energy, mainly due to ionisation, in the material between the inner detector and the muon spectrometer although high-p_{T} muons occasionally deposit a very large fraction of their energy via bremsstrahlung radiation. The final muon momentum is calculated from two tracks and the calorimeter energy loss information.

Muon candidates are required to have $p_{\mathrm{T}} > 10$ GeV, $|\eta| < 2.4$, and longitudinal and transverse impact parameters within 1 mm and 0.2 mm of the primary vertex, respectively. These selections have an overall efficiency of approximately 99%. Any muon that meets these selection requirements is referred to as a *loose* muon. To ensure that a muon did not originate from a hadron in a jet, the muon candidate is required to fulfil the isolation requirement that there should be at most one additional track with $1 < p_{\mathrm{T}} < 1.8$ GeV reconstructed within a cone of size $\Delta R = 0.2$ around the muon. Any muon that meets all these requirements is referred to as a *tight* muon thus making *tight* muons a subset of *loose* muons.

The systematic uncertainties related to muons will be discussed in Chapter 7.

4.2.5 Tau leptons

The tau lepton can decay to produce an electron or muon (combined branching ratio $\sim 35\%$) but it is also heavy enough that it can decay hadronically (branching ratio $\sim 65\%$). Typically no effort is made to determine if an electron or muon came from a tau lepton decay; however, special algorithms are used to reconstruct and identify hadronically decaying taus. Hadronic decays of the tau lepton predominantly produce one or three charged pions and a neutrino. They may also be accompanied by neutral pions. Over 90% of all hadronic tau decays include at least one charged pion [10]. The remaining 10% includes decays with other types of charged hadrons and decays with ≥ 5 charged hadrons. Hereafter the hadronic tau decay producing one charged hadron will be referred to as the one-prong decay and the decay producing three charged hadrons will be referred to as the three-prong decay.

Hadronically decaying taus leave signatures in the ATLAS detector that are very similar to those of jets from quarks and gluons: there are energy deposits in the calorimeters from charged and neutral hadrons and track(s) in the inner detector. One of the main distinguishing features of a hadronically decaying tau is that they predominantly produce just one or three charged hadrons with branching ratios of

50% and 15% respectively. The sum of the charges of the hadrons must equal ± 1 due to the conservation of charge of the tau lepton.

The process of reconstructing and identifying a hadronically decaying tau relies on several important discriminating variables including the narrow shower shape, a displaced vertex, and the number of charged particle tracks. The process of selecting hadronically decaying taus in ATLAS events is slightly different from that of muons, electrons, or jets because the process is broken up into a reconstruction process and then an identification process. Many objects may go through the first step of being reconstructed as a hadronically decaying tau but they are only considered a reconstructed hadronically decaying tau if they also pass the identification step.

Hadronically decaying taus are built from a set of jets reconstructed using the anti-k_t algorithm with radius parameter $R = 0.4$, $p_{\mathrm{T}} > 10$ GeV, and $|\eta| < 2.5$ [96]. The topocluster energy deposits from each of these jets are used to seed a hadronically decaying tau.

The vertex from which a hadronically decaying tau was produced is explicitly determined since in events with multiple primary vertex candidates due to pile-up, the chosen primary vertex may not match the vertex from which the hadronically decaying tau was produced. The tau lepton has a short lifetime but it is long enough that it travels a short distance within the beampipe before it decays ($c\tau = 87$ μm). It is with respect to this tau vertex that the properties of the hadronically decaying tau are determined including its transverse momentum [96, 97]. Tracks in the jet candidate are identified and hit pattern requirements are imposed. The tracks that are used to classify each hadronically decaying tau candidate as having one or three charged hadrons are those that lie within $\Delta R < 0.2$ of the axis of the seed jet.

The hadronically decaying tau energy reconstruction is done in a way similar to that of jets but is specific to tau leptons. Topoclusters are reconstructed and local hadronic calibrations are applied. The topoclusters used to measure the hadronically decaying tau energy are located within $\Delta R < 0.2$ of the hadronically decaying tau axis. Other calibrations are applied to the hadronically decaying tau to correct for pile-up, to align the decay products with the tau vertex, to calibrate the hadronically decaying tau energy and η, and to correct for differences between the data and Monte Carlo [96]. These calibrations make up the "tau energy scale" (TES) calibration. The hadronically decaying tau energy refers just to the visible energy as the neutrinos from the tau lepton decay carry away energy that is lost. The mass of this measured visible hadronically decaying tau object is defined to be zero. More details on the tau

energy scale are given in Chapter 7.

The reconstruction process focuses on accurately determining the properties of a hadronically decaying tau candidate if the object is indeed a hadronically decaying tau. Unfortunately, these selection criteria do not filter out much of the large background of jets that can produce similar signatures in the detector. As a result the process of reconstructing topoclusters and tracks as a hadronically decaying tau is, by itself, insufficient for the task of isolating hadronically decaying taus for use in an analysis. After the reconstruction step an identification phase is required to distinguish true hadronically decaying taus from the jets, electrons and to a lesser extent, muons, that can be mistaken for hadronically decaying taus. The hadronically decaying tau identification is performed by a boosted decision tree (BDT), which is a multivariate technique [98, 99].

To distinguish a hadronically decaying tau from a jet there are two BDTs, one specifically designed for one-pronged decays and another for three-pronged decays. Several of the important variables to reject jets include the fraction of the energy deposited in the most central region of the hadronically decaying tau candidate, a p_{T}-weighted ΔR for all tracks associated to the hadronically decaying tau with respect to the tau axis $\left(R_{\mathrm{track}} = \frac{\sum_i^{\Delta R_i<0.3} p_{\mathrm{T}}^i \Delta R_i}{\sum_j^{\Delta R_j<0.3} p_{\mathrm{T}}^j}\right)$, and the number of tracks in the isolation region of $0.2 < \Delta R < 0.4$. See Reference [96] for more details. A separate BDT is used to distinguish the identified hadronically decaying taus from electrons. Several of the important discriminating variables to reject electrons include the energy distributions between the EM and hadronic calorimeters, and transition radiation information from the TRT for the charged particles.

The identification algorithms are calibrated at three working points with different levels of hadronically decaying tau identification efficiency balanced against rejection power against mis-identification of jets and electrons. In this analysis only one working point is used (the *medium* working point) where the jet-veto identification algorithm has a 60% and 55% signal efficiency for one- and three-pronged decays respectively while the electron-veto identification algorithm has an 85% signal efficiency. For low momentum τ_{had} candidates, the jet-veto identification algorithm has inverse background efficiencies (rejection factors) of approximately 20 and 90 for one- and three-pronged decays respectively (see Figure 5a of [96]). The electron-veto has an inverse background rejection better than approximately 100 (see Figure 9 of Reference [96]). The final hadronically decaying tau candidates are required to have

$p_{\mathrm{T}} > 20$ GeV, and $|\eta| < 2.47$.

The systematic uncertainties related to hadronically decaying taus will be discussed in Chapter 7.

4.2.6 Missing momentum

The missing transverse momentum vector, $\mathbf{p}_{\mathrm{T}}^{\mathrm{miss}}$, (where $E_{\mathrm{T}}^{\mathrm{miss}} \equiv \left|\mathbf{p}_{\mathrm{T}}^{\mathrm{miss}}\right|$) is calculate as the negative vector sum of the transverse momenta of all the reconstructed electrons, photons, jets, and muons, as well as the calorimeter energy clusters that are not associated to a reconstructed object [100]. The hadronically decaying taus are treated as jets in this calculation. The reconstructed electrons and jets are required to have $p_{\mathrm{T}} > 10$ GeV, and $p_{\mathrm{T}} > 20$ GeV respectively. The reconstructed muons and photons are required to have $p_{\mathrm{T}} > 5$ GeV, and $p_{\mathrm{T}} > 20$ GeV respectively. The calculation also includes muons reconstructed in the muon spectrometer that are outside the inner detector acceptance and thus cannot be reconstructed as combined muons. The energy deposits in the form of topoclusters (see Section 4.2) that are not associated to a reconstructed object and the tracks connected to the primary vertex that are not associated to a reconstructed object are both included. When one of these tracks can be associated to one of these topoclusters then only one of the p_{T} of the track or the transverse energy of the topocluster is included depending on which is expected to have the better resolution. The calculation includes calorimeter cells in $|\eta| < 4.5$.

The systematic uncertainties related to missing transverse momentum will be discussed in Chapter 7.

4.2.7 Overlap removal

A given final-state object can be simultaneously reconstructed as (for example) a jet, an electron, or a muon. There are many reasons that this can occur, for example jets and hadronically decaying taus leave similar signatures in the detector, and some hadrons in a jet can decay to produce muons. An algorithm is used to resolve these ambiguities for the reconstructed electrons, jets, muons, and hadronically decaying taus described in this section. If two objects are close in ΔR then one is discarded following the rules and sequence defined in Table 4.1.

Table 4.1: Sequence of the overlap removal algorithm. Here, ℓ refers to electrons and muons.

Condition	Discarded object
$\Delta R(\text{jet}, \text{electron}) < 0.2$	jet
$\Delta R(\tau_{\text{had}}, \ell) < 0.2$	τ_{had}
$\Delta R(\text{jet}, \ell) < 0.4$	ℓ
$\Delta R(\tau_{\text{had}}, \text{jet}) < 0.2$	jet

Chapter 5

Data and Monte Carlo simulations

The search for scalar tops requires a comparison of data to the Standard Model. The data are collected by the ATLAS detector using a combination of triggers, and the Standard Model backgrounds are estimated using Monte Carlo simulations. The simulations of the events are not perfect and so the distributions from the simulations are corrected to match the distributions in the data by using scale factors. This chapter dicusses the data, the simulations, and the corrective weights applied to the simulated events.

5.1 Data

In 2012 a total of 21.3 fb^{-1} of data were recorded by ATLAS at a centre of mass energy of 8 TeV as shown in Figure 5.1. This analysis uses the data that were collected by electron triggers and muon triggers (see Chapter 4).

To maximise the efficiency of triggering on an electron, the logical OR of two electron triggers is used. One electron trigger has a minimum p_{T}-threshold of 24 GeV, while the other has a p_{T}-threshold of 60 GeV. Both of these triggers have a prescale of 1 (see Section 4.1.1) and the 24 GeV electron trigger was the lowest-threshold unprescaled electron trigger during the data-taking period. The lower p_{T}-threshold trigger has an isolation requirement on the electron that is not used in the higher p_{T}-threshold trigger. This isolation requirement reduces the probability for selecting fake low-p_{T} electrons but means that the trigger is not fully efficient at high-p_{T} because the electrons may radiate a large amount of energy, and so the 60 GeV threshold trigger without isolation is used to make up the difference.

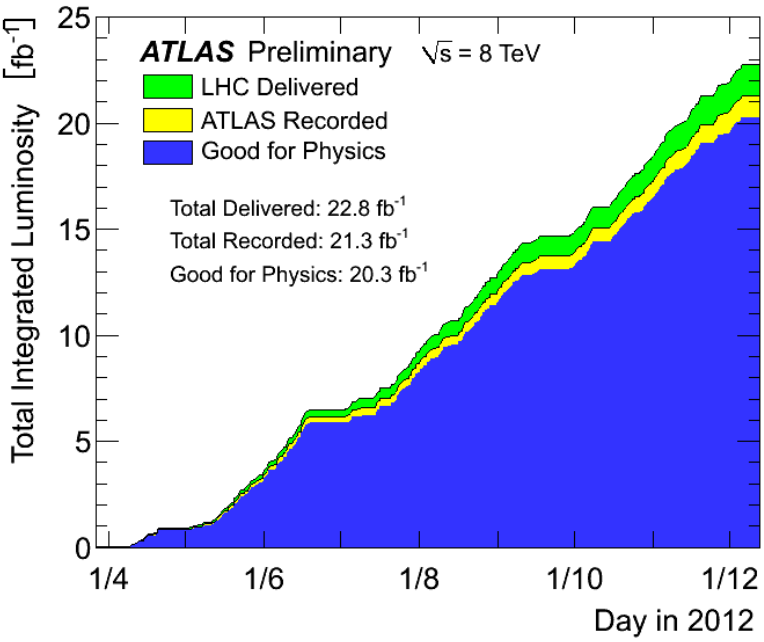

Figure 5.1: Total integrated luminosity and data quality in 2012 [101]

A very similar situation exists with the muon trigger. A logical OR is applied between a single-muon trigger with a minimum p_{T}-threshold of 24 GeV and a single-muon trigger with a p_{T}-threshold of 36 GeV. Again the higher p_{T} threshold trigger is used to supplement the lower p_{T} threshold trigger that has an additional isolation requirement. Both triggers are unprescaled and the 24 GeV muon trigger was the lowest-threshold unprescaled muon trigger during the data-taking period.

This combination of triggers reaches a maximum efficiency for light charged leptons of $p_{\mathrm{T}} > 25$ GeV. After the data-quality requirements are applied (i.e. removing events because a vital part of the detector was not operational), the integrated luminosity of the data samples from the combination of the electron and muon triggers for this analysis is 20.3 fb^{-1} [102].

In 2012 the LHC collided protons with a 50 ns bunch spacing. The LHC settings with this bunch spacing meant that the amount of pile-up was different from what it would be with the nominal 25 ns bunch spacing. The average in-time pile-up was 20.7 interactions per bunch crossing as shown in Figure 5.2.

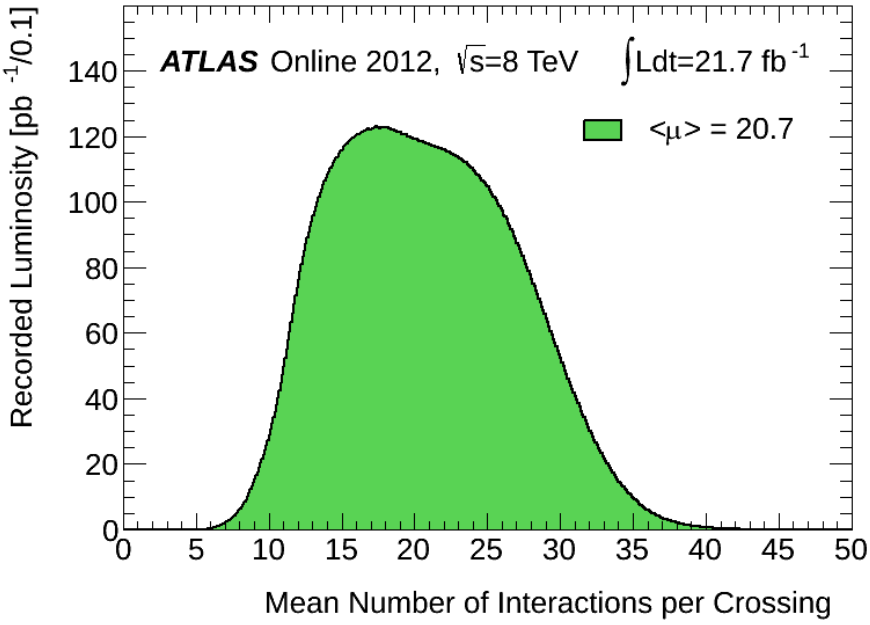

Figure 5.2: Number of interactions per bunch crossing in 2012 [101]

5.2 Monte Carlo simulations

Simulations of the proton–proton collisions and the ATLAS detector are required to properly model the background and signal processes in this analysis. The simulation of an event divides the event processes into several steps that are illustrated in Figure 5.3. Since protons are made up of quarks and gluons, the proton–proton collision is really a collision of partons, which have a distribution of possible momenta. These distributions of momenta are called "parton distribution functions" (PDF). The part of the collision that produces the particles of interest in this analysis is labelled in the figure as the hard sub-process. The colliding quarks and gluons may radiate particles (initial state radiation, not depicted) before the collision and the particles produced in the hard sub-process may also radiate producing final state radiation. These cascades of radiation are referred to as parton showers where the term parton is used to encompass quarks and gluons but also leptons and photons (the showering of radiation is not just from QCD). The quarks and gluons then hadronise and a chain of decays may occur.

The other partons from the protons in the original proton–proton collision also undergo these same processes and produce what is called the underlying event (not shown in Figure 5.3). Pile-up from multiple proton–proton interactions and multiple

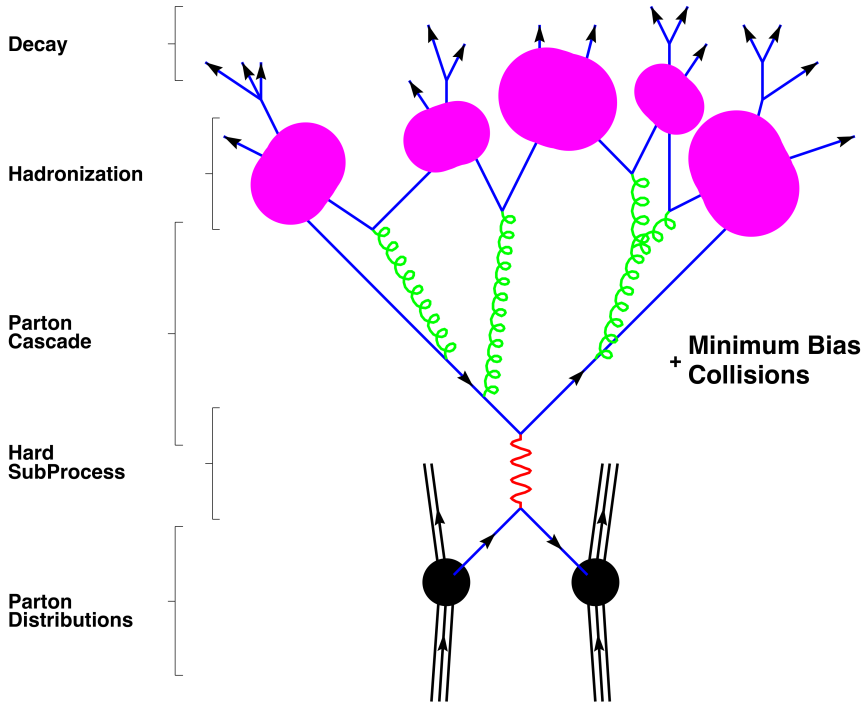

Figure 5.3: Event structure. The image was taken from Reference [103] and modified. See text for more details.

parton–parton interactions is also simulated. The propagation of the particles through the detector is then simulated. This simulation takes into account the geometry of the ATLAS detector and the detector responses. The output from the simulation is an "event" that can be reconstructed in exactly the same way as a data event.

Several different event generators are used to simulate the hard-scattering processes. Each hard-scattering process is simulated by an event generator that was selected based on the generator's relative strengths and weaknesses. Several factors that come into play when selecting the appropriate generator for a specific process include: the order at which the hard-scattering process (matrix element) is simulated, whether or not spin correlations are included, the accuracy of the simulation of large numbers of additional jets arising from partons radiated in the initial or final state, and the capacity to model particles and interactions not present in the Standard Model. Other practical factors are also taken into account such as the amount of time required to simulate the events using a specific event generator and whether or not the generator has been validated for use by the ATLAS Monte Carlo groups. Table 5.1 shows the details about the MC generation for the dominant background samples

Table 5.1: Details on the MC generation of the signal and dominant background samples.

Process	Generator	Parton shower	Cross-section normalisation	PDF set	Generator tune
$t\bar{t}$	POWHEG-BOX r2129 [104, 105]	PYTHIA 6.426 [106]	NNLO+NNLL [107, 108, 109, 110, 111, 112]	NLO CT10 [113]	Perugia 2011C [114]
$W(\to L\nu)$+jets, $L = e, \mu, \tau$	SHERPA 1.4.1 [115]	SHERPA 1.4.1	NNLO [116]	NLO CT10	SHERPA default
$\tilde{t}_1\tilde{t}_1^*$	HERWIG++ 2.6.3 [117]	HERWIG++ 2.6.3	NLO+NLL [118, 119, 120]	CTEQ6L1 [121]	UE-EE-3 [122]

Table 5.2: Details on the MC generation of the $t\bar{t}$ background samples used for the systematic uncertainty studies.

Usage	Generator	Parton shower
Nominal	POWHEG-BOX r2129	PYTHIA 6.426
Systematic - Generator	MC@NLO-4.06 [123]	HERWIG (parton shower) + Jimmy (additional parton interactions)[124]
Systematic - Parton shower	POWHEG-BOX r2129	HERWIG (parton shower) + Jimmy (additional parton interactions)
Systematic - ISR/FSR	AcerMC-3.8 [125]	PYTHIA 6.426

and the signal samples. Table 5.2 shows the details about the MC generation used for the systematic variations for the $t\bar{t}$ samples, which will be discussed in Chapter 7.

All of the simulated events were processed using either the full ATLAS detector simulation [126] based on GEANT4 [127] or a fast simulation. The fast simulation is based on a parameterisation of the performance of the ATLAS calorimeters [128] and the full GEANT4 simulation is used everywhere else in these events.

5.2.1 Corrective weights

Every Monte Carlo simulated event is assigned several multiplying scale factors to reweight various distributions to match data. No weights are applied to the data, only to the simulated events. Some of these corrective weights include:

- Pile-up: The simulated events contain pile-up but the pile-up conditions were not known when the events were generated, which was before the data were taken. The amount of pile-up is a function of how the LHC is run. The distribution of the number of proton–proton inelastic collisions per event (see Figure 5.2) and the number of primary vertices per event are correlated and both corrected using event-level weights.

- Reconstruction and identification: The identification and reconstruction efficiencies of the charged leptons (e, μ, τ) in simulation do not perfectly match those in data. Event-level weights are applied to compensate for this. One weight is applied to the event where the value of the weight is based on the properties of the τ_{had} and another weight is applied to the event where the value of the weight is based on the properties of the light charged lepton.

- b-tagging: An event-level scale factor is used to correct the b-tagging efficiency because the b-tagging efficiency in the simulation is slightly different from the efficiency in data. The "b-tagging efficiency scale factor" is not the same as the "b-tagging weight" (see Section 4.2.2). The former is used as an event-level weight while the latter is a quantity that is used to set the tagging efficiency. A b-tagging efficiency scale factor is calculated for each jet as a function of the jet p_{T} and the jet η. The total event-level b-tagging efficiency scale factor is the product of all the individual jet b-tagging efficiency scale factors.

- Triggers: The simulations include the same triggers used on the data. An event-level weight is applied to correct for the differences in the trigger efficiencies between simulation and data [83, 129, 75, 130].

- $t\bar{t}$: ATLAS measurements of the $t\bar{t}$ cross-section found that the `POWHEG-BOX` + `PYTHIA` simulation of $t\bar{t}$ events overestimates the transverse momentum of the top pair system with respect to data [131]. Event-level scale factors are used to reduce the weight of events that have a higher $p_{\text{T}}^{t\bar{t}}$.

The above list only refers to the corrective weights that were derived by ATLAS groups dedicated to that task; the weights are applicable to many different ATLAS analyses. The corrective weights that were measured specifically for this analysis will be described in Chapter 6.

An overall scale factor is also applied to the simulated events to obtain the same total integrated luminosity as the data, as described in Section 5.1. A scale factor is also used to impose the appropriate cross-section and branching ratio for each individual process. The triggers are all unprescaled so no prescale weights need to be explicitly included.

Chapter 6

Analysis

6.1 Introduction

This analysis is a search for the direct production of pairs of scalar tops that decay to produce two tau leptons, two b-jets, and large amounts of missing transverse momentum [57] as described in Section 2.3.4. As each tau lepton can decay either to hadrons or to light charged leptons, there are three possible final states: lepton–lepton, lepton–hadron, and hadron–hadron. These tau lepton final states define the three separate analyses that were performed. The lepton–hadron search is the focus of this dissertation.

Two parameters define the signal model: the mass of the scalar top and the mass of the scalar tau (the gravitino is assumed to be nearly massless). The three searches are designed to complement each other by probing different parts of the phase space defined by the masses of these two particles, which will be referred to as the "stop-stau mass plane". There is some overlap in the sensitivity regions of the different analyses to ensure full coverage of the stop-stau mass plane. The lepton–lepton analysis is a re-interpretation [132] of an earlier search for direct pair production of scalar tops that decay $\tilde{t}_1 \to t + \tilde{\chi}_1^0$ or $\tilde{t}_1 \to b + \tilde{\chi}_1^\pm$ [133]. The lepton–lepton analysis probes the region of phase space very close to the kinematic limit of $m(\tilde{t}_1) = m(b) + m(\tilde{\tau}_1)$, where the masses of the other particles not shown in this equation are small and have been ignored (e.g. neutrino mass). The hadron–hadron analysis [57] is designed to probe low scalar tau masses for a wide range of scalar top masses. The lepton–hadron analysis [57] has two sub-analyses. The lepton–hadron "low-mass analysis" targets models with light scalar tops. The lepton–hadron "high-mass analysis" targets

models with heavy scalar tops but where the scalar tau mass is also large. Together the analyses based on the three decay channels of the two tau leptons cover light and heavy scalar tops and light and heavy scalar taus.

Each decay channel comes with different benefits and complications. The design of the signal regions for the different decay channels takes these into account. Some of the important factors/concepts that affect the design of the analyses include:

- Cross-sections: The production cross-section of pair-produced scalar tops decreases as the mass of the scalar top increases. This means that a signal region should be designed to be sensitive to a specific range of scalar top masses.

- Branching ratios: The relative and absolute branching ratios for leptonic and hadronic decays in the signal and the dominant backgrounds are important. The analysis design has to balance the branching ratios of the signal and background processes along with the production cross-sections.

- Object resolution: The resolution of the four-momentum of light charged leptons is better than that of jets and hadronically decaying taus. The resolution of the four-momentum of the final state objects affects the resolution for reconstructing the masses of the scalar top and the scalar tau. When designing an analysis, consideration should be put towards which final state to use to meet the required resolutions of the scalar top and scalar tau masses for the various signal regions.

The lepton–hadron search will be described in detail and is the focus of this dissertation. The results from all three channels will be discussed. No previous hadron collider searches have been published looking for the three-body decay of the scalar top into the scalar tau. The only existing limits that can be directly applied to this analysis are from LEP where searches for direct pair-production of the scalar tau were performed. A conservative combination of the LEP results excludes a scalar tau with a mass less than 87 GeV [134, 135, 136, 137, 138] as long as the mass of the LSP is not within $\sim$ 10 GeV of the mass of the scalar tau. A search for direct pair production of scalar taus has also been performed by ATLAS [139]. Searches for the scalar top with the neutralino as the LSP have been performed by both the ATLAS and CMS collaborations [59, 60, 61, 62, 63, 64, 65]. Searches for scalar tops decaying to gravitinos (but without a scalar tau in the decay chain) have also been performed [140, 141, 142]. Thus far no searches for the scalar top have shown any statistically significant excesses.

6.2 Main backgrounds introduction

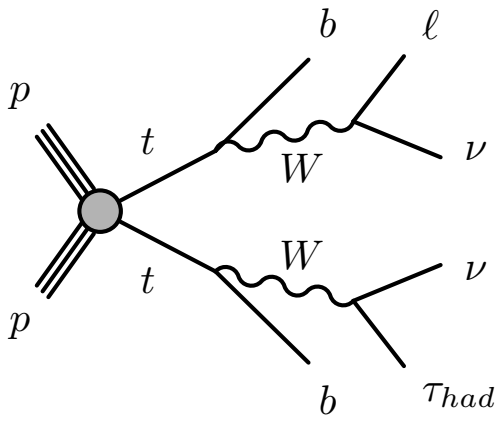

(a) Real-τ_{had} $t\bar{t}$ decay

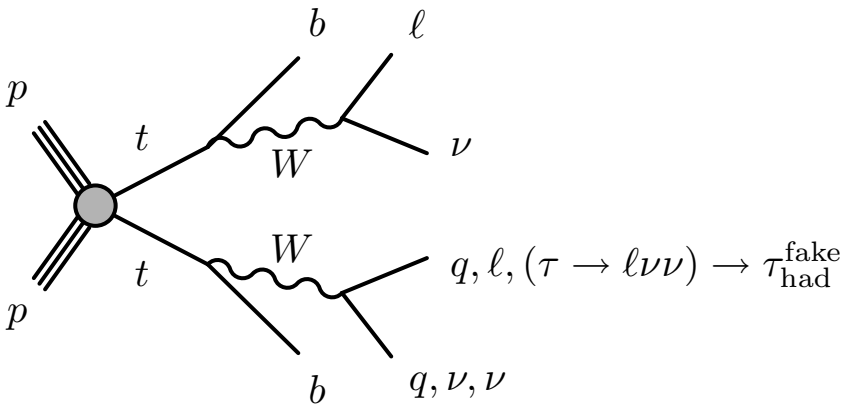

(b) Fake-τ_{had} $t\bar{t}$ decay

Figure 6.1: Main $t\bar{t}$ background made up of true (Figure 6.1a) and fake (Figure 6.1b) hadronically decaying taus. In Figure 6.1b no hadronically decaying taus are produced; instead one of the other decay products of a W boson decay (depicted here) or one of the additional jets in the event (depicted in Figure 6.2) is misidentified as a τ_{had}.

The dominant background processes to the lepton–hadron channel are $t\bar{t}$ with a real hadronically decaying tau, $t\bar{t}$ with a fake hadronically decaying tau, and W+jets with a fake hadronically decaying tau. These processes are shown in Figures 6.1 and 6.2 and will be discussed in more detail in Section 6.5.4 after the event selection is defined in Section 6.5.3.

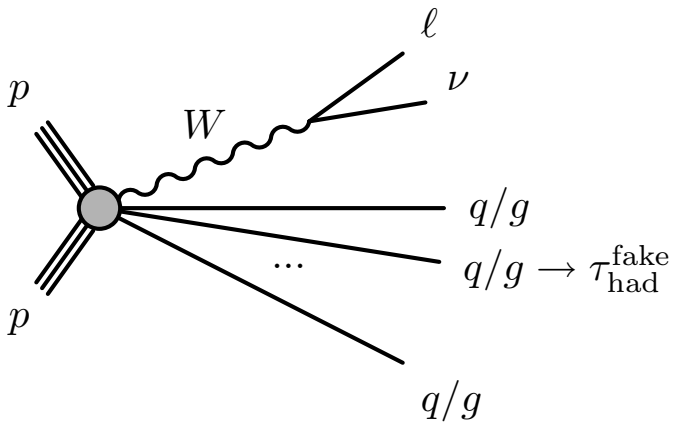

Figure 6.2: W+jets. One of the additional jets in the event is misidentified as a τ_{had}.

6.3 Background estimation

The general analysis strategy involves applying various sets of selections of events (cuts) to define different regions in the phase space. A signal region is defined with a set of cuts that maximise the sensitivity to the signal. The lepton–hadron analysis has a signal region to search for low-mass scalar tops (SRLM) and a signal region to search for high-mass scalar tops (SRHM).

The search for new particles requires an accurate and precise estimation of the background processes that can mimic the signal. In this analysis the main background processes are all estimated using Monte Carlo simulations but their overall scale is corrected to match data (see Section 6.6). All the other types of background processes, which only contribute a relatively small number of events, are estimated directly from simulations.

The expected dominant backgrounds in the signal region are studied in isolation using control regions. Control regions are designed so that most of the events in them are from background processes and only a small fraction of events are from signal (assuming there is any). We say that these regions have low signal contamination. Control regions are required to have low signal contamination to test the modelling of the background events by comparing the simulated events to the data. For each of the two signal regions there are three control regions, one for each dominant background process: there is a control region for W+jets, a control region for top-quark events with a real hadronically decaying tau, and a control region for top-quark events with a fake hadronically decaying tau. The total numbers of events in the control regions

are scaled to match the data. This is called the background-only fit, the details of which will be described in Chapter 9. The scale factors are then applied to the signal region to produce the expected distribution of background events in the signal region.

The top-quark control regions for true and fake hadronically decaying taus for the low-mass selection are referred to as CRTfLM and CRTtLM respectively while CRWLM refers to the low-mass W+jets control region. Similarly, the top-quark control regions for true and fake hadronically decaying taus for the high-mass selection are referred to as CRTfHM and CRTtHM respectively while CRWHM refers to the high-mass W+jets control region.

The top-quark control regions are composed of both Wt and $t\bar{t}$ events but are designed around the pair-produced top-quark events, which dominate. They separate true and fake hadronically decaying taus because fake hadronically decaying taus are not expected to be as well modelled as real hadronically decaying taus. Most characteristics of the events with fake hadronically decaying taus are, however, well modelled, with the exception of the overall number of events and the p_{T} distribution of the hadronically decaying tau in W+jets events. The p_{T} of the (fake) hadronically decaying taus in W+jets events is corrected using data and this correction process will be discussed in more detail in Section 6.5.7 after describing how the analysis isolates W+jets events. All the plots in this dissertation include the correction to the hadronically decaying tau p_{T} distribution for W+jets events unless otherwise specified.

The extrapolation of the scale factors to the signal regions is checked in validation regions where there is also little signal contamination. The low-mass and high-mass validation regions are labelled as VRLM and VRHM respectively. The control regions and validation regions are designed to be very similar to the signal region but with little signal contamination. In terms of the main kinematic variable(s) that separate the control regions, validation region, and signal region, the validation region is placed between the control regions and signal region to test the extrapolation in the correct direction.

This analysis is performed "blinded" to minimise the human bias. The blinding is done by not looking at the data in the signal regions until it has been checked that the data match the SM expectations in the control regions and validation regions. Once the background estimations are validated then the signal regions are unblinded by looking at the data in them. All of these steps have been performed and only the unblinded results will be shown in this dissertation.

6.4 Analysis tools

A range of tools are required to perform this analysis. Custom software was written in `C++` using `ROOT` [143] to select the reconstructed events and to generate plots. Statistical analysis of the data and Monte Carlo is performed using the `HistFitter` program [144] and will be discussed in Chapter 9.

6.5 Event selection

6.5.1 Event cleaning

After the events are reconstructed, some final event cleaning must be performed before the events can be selected for the various signal, control, and validation regions. The purpose of event cleaning is to remove events contaminated by things like non-beam radiation. Events are vetoed if a potential cosmic muon is found where cosmic muons are conservatively assumed to be any muons found to have longitudinal and transverse impact parameters outside of 1 mm and 0.2 mm of the primary vertex, respectively. Events may also be vetoed based on the objects in the event passing through regions of the detector that are known to have malfunctioned at around the same period of time.

6.5.2 Additional kinematic variables

Determining what process took place in an event can be difficult and so several kinematic variables are used to extract more information from the four-momenta of the final state particles. The scalar sum of the transverse momenta of the two highest-p_{T} jets ("leading" jets) is referred to as H_{T}. This variable estimates the amount of hadronic activity in the event. The effective mass, $m_{\mathrm{eff}} = H_{\mathrm{T}} + E_{\mathrm{T}}^{\mathrm{miss}} + p_{\mathrm{T}}^{\ell} + p_{\mathrm{T}}^{\tau_{\mathrm{had}}}$, is a measure of the total amount of activity in the event. The transverse momenta of the light charged lepton and the hadronically decaying tau are represented by p_{T}^{ℓ} and $p_{\mathrm{T}}^{\tau_{\mathrm{had}}}$ respectively.

A very useful quantity to separate the different types of background processes as well as the signal from background would be the invariant masses of the parent particles: the W boson, the top quark, the scalar tau, and the scalar top. Unfortunately the invisible particles (including neutrinos as well as the LSP) prevent a full reconstruction of the masses of the parent particles. Instead, several kinematic variables

are used to estimate/investigate these parent particle masses using the missing transverse momentum. These variables will first be defined in very general terms before then describing how they can be used to investigate the masses of the parent particles in specific processes.

The transverse mass associated with two final-state objects a and b is defined as

$$m_{\mathrm{T}}\left(\mathrm{a},\mathrm{b}\right) = \sqrt{m_{\mathrm{a}}^2 + m_{\mathrm{b}}^2 + 2\left(E_{\mathrm{T}}^{\mathrm{a}} E_{\mathrm{T}}^{\mathrm{b}} - \mathbf{p}_{\mathrm{T}}^{\mathbf{a}} \cdot \mathbf{p}_{\mathrm{T}}^{\mathbf{b}}\right)}, \tag{6.1}$$

where m and $\mathbf{p}_{\mathrm{T}}$ are the masses and transverse momentum vectors, respectively, of the daughter particles, and the daughter particles may be visible or invisible. The transverse energy of the daughter particles, E_{T}, is defined as $E_{\mathrm{T}} = \sqrt{m^2 + p_{\mathrm{T}}^2}$. The definition of the transverse mass is analogous to the mass of a parent particle decaying to objects a and b, $m\left(\mathrm{a},\mathrm{b}\right) = \sqrt{m_{\mathrm{a}}^2 + m_{\mathrm{b}}^2 + 2\left(E^{\mathrm{a}} E^{\mathrm{b}} - \mathbf{p}^{\mathbf{a}} \cdot \mathbf{p}^{\mathbf{b}}\right)}$, but it uses only the transverse information instead of the full three-dimensional information. As a result, the invariant mass of the parent particle is the upper limit on the transverse mass (ignoring offshell decays and energy resolutions etc.).

In some decays, a daughter particle is undetectable and it is impossible to fully reconstruct the mass of the parent particle. The transverse mass is most useful when one of the child particles is a neutrino (or another weakly interacting particle that escapes detection) because the missing transverse momentum can be used in place of the neutrino. In the case of a $W \to \ell\nu$ decay, $m_{\mathrm{T}}\left(\ell, p_{\mathrm{T}}^{\mathrm{miss}}\right)$ provides an estimate of the W boson mass, which is by construction smaller than the actual parent particle mass, assuming that no other invisible particles in the event contribute to the $p_{\mathrm{T}}^{\mathrm{miss}}$. A kinematic maximum to $m_{\mathrm{T}}\left(\ell, p_{\mathrm{T}}^{\mathrm{miss}}\right)$ in $W \to \ell\nu$ events is useful when trying to separate them from other events and processes that allow the variable to extend above that kinematic upper limit. Most of the time the term "transverse mass" is used to refer to $m_{\mathrm{T}}\left(\mathrm{a},\mathrm{b}\right)$ where $\mathrm{b} = \mathrm{p}_{\mathrm{T}}^{\mathrm{miss}}$ because for all the other measurable objects in an event one can calculate the full invariant mass rather than just the transverse mass. The objects entering the m_{T} calculation are often assumed to be massless.

A variable similar to the transverse mass is defined for the decays of particles produced in pairs. The "stransverse mass" (m_{T2}) [145, 146] is computed as

$$m_{\mathrm{T2}}\left(\mathrm{a},\mathrm{b}\right) = \sqrt{\min_{\mathbf{q}_{\mathrm{T}}^{\mathbf{a}} + \mathbf{q}_{\mathrm{T}}^{\mathbf{b}} = \mathbf{p}_{\mathrm{T}}^{\mathrm{miss}}} \left(\max\left[m_{\mathrm{T}}^2\left(\mathbf{p}_{\mathrm{T}}^{\mathrm{a}}, \mathbf{q}_{\mathrm{T}}^{\mathrm{a}}\right), m_{\mathrm{T}}^2\left(\mathbf{p}_{\mathrm{T}}^{\mathrm{b}}, \mathbf{q}_{\mathrm{T}}^{\mathrm{b}}\right)\right]\right)}, \tag{6.2}$$

where $\mathbf{q}_{\mathrm{T}}^{\mathrm{a}}$ and $\mathbf{q}_{\mathrm{T}}^{\mathrm{b}}$ are any pair of two-dimensional vectors satisfying $\mathbf{q}_{\mathrm{T}}^{\mathrm{a}} + \mathbf{q}_{\mathrm{T}}^{\mathrm{b}} = \mathbf{p}_{\mathrm{T}}^{\mathrm{miss}}$. A

minimisation is performed on the maximum of the two transverse masses over all the allowed combinations of $\mathbf{q}_{\mathrm{T}}^{\mathrm{a}}$ and $\mathbf{q}_{\mathrm{T}}^{\mathrm{b}}$. The stransverse mass is used when two identical parent particles are produced and each decays to at least one invisible particle. It is a very similar quantity to transverse mass but a minimisation is required to partition the missing transverse momentum (a single measurable quantity) between the two invisible particles. The $\mathbf{q}_{\mathrm{T}}^{\mathrm{a}}$ and $\mathbf{q}_{\mathrm{T}}^{\mathrm{b}}$ vectors are effectively dummy particles that take the place of the particles that escaped undetected. After the minimisation, their transverse momenta are correlated with the true transverse momenta of the invisible particles; however, the minimum does not correspond to the actual true transverse momenta. In the case of a $WW \to e\nu\mu\nu$ decay, $m_{\mathrm{T2}}(e,\mu)$ provides an estimate of the mass of the W boson, which is deliberately smaller than the actual parent particle mass, assuming that only the two neutrinos in the event contribute to the $p_{\mathrm{T}}^{\mathrm{miss}}$. A kinematic maximum to $m_{\mathrm{T2}}(e,\mu)$ in $WW \to e\nu\mu\nu$ events is useful when trying to separate them from other events and processes that allow the variable to extend above that kinematic upper limit. The maximum function in the m_{T2} definition can be used because the two parent particles are assumed to be identical and thus have the same mass (although not necessarily the same transverse mass).

6.5.3 Preselection

The lepton–hadron channel requires that there be at least two jets with $p_{\mathrm{T}} > 20$ GeV in an event, the highest-p_{T} jet must have $p_{\mathrm{T}} > 50$ GeV, and at least one of these two jets must be b-tagged. It requires exactly one *tight* electron or muon with $p_{\mathrm{T}} > 25$ GeV and no additional *tight* electrons or muons of $p_{\mathrm{T}} > 10$ GeV. Exactly one hadronically decaying tau with $p_{\mathrm{T}} > 20$ GeV is required and it must have the opposite charge to that of the light charged lepton. This set of cuts is referred to as the SRHM preselection.

After these cuts, some further cuts are applied to split the analysis into the low-mass and high-mass signal regions. The low-mass signal region is designed to search for scalar tops with masses that are close to or smaller than the mass of the top quark. The high-mass signal region is designed to search for scalar tops with masses that are larger than the top-quark mass. The high-mass SR is not designed to be sensitive to all allowed scalar tau masses but only to large scalar tau masses. Figure 6.3 is a sketch of where each lepton–hadron signal region targets in the stop-stau mass plane.

The SRHM preselection is designed for the high-mass analysis. The SRLM prese-

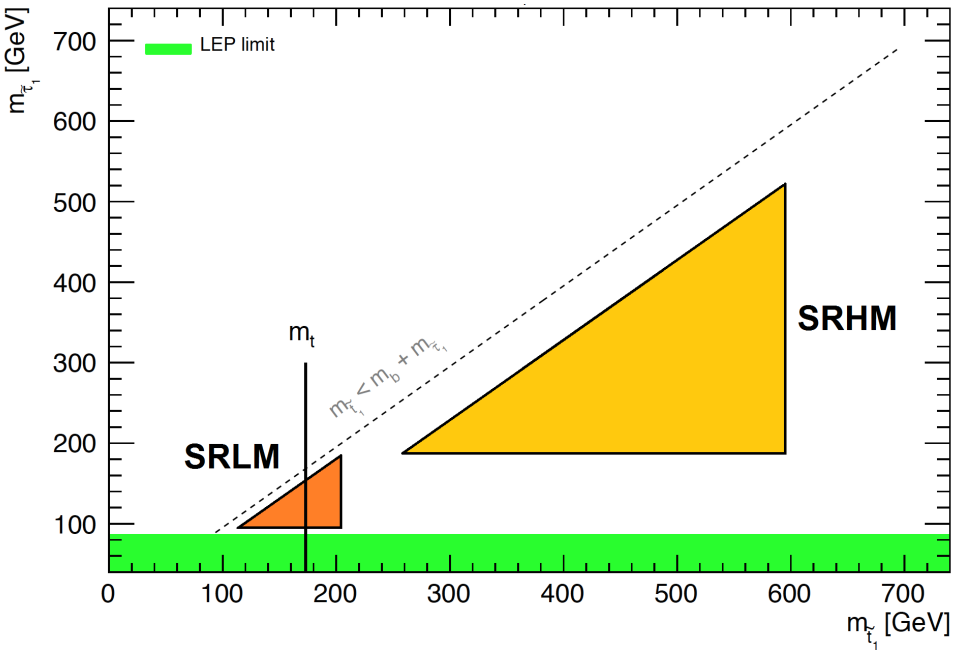

Figure 6.3: The low-mass and high-mass signal regions in the lepton–hadron analysis are designed to target different parts of the stop-stau mass plane.

lection is used for the low-mass analysis and has the same cuts as the SRHM preselection but with the requirement of two, not just one, b-tagged jets. Even though the dominant $t\bar{t}$ background and signal events effectively always produce two b quarks, some regions require only a looser selection of one or more b-tagged jets because the b-tagging inefficiency loses an unacceptably large fraction of signal events when both b-jets are required to be tagged (efficiency $= 0.7 \times 0.7 = 0.49$).

The low-mass and high-mass signal regions were optimised with respect to the expected signal significance using the $(m_{\tilde{t}_1}, m_{\tilde{\tau}_1}) = (195, 87)$ and $(391, 148)$ GeV mass points respectively. The sets of cuts defining the two signal regions are summarised in Tables 6.1 and 6.2 and will be described in more detail in Section 6.5.5.

A set of distinctive and useful kinematic distributions after the SRHM preselection are plotted in Figures 6.4, 6.5, and 6.6. The distributions for the light charged lepton p_{T} and the hadronically decaying tau pseudorapidity after the SRHM preselection are shown in Figures 6.4 and 6.5 respectively. The SRHM preselection distributions for the p_{T} of the highest- and second-highest-p_{T} jets are shown in Figure 6.6. Figures 6.4 - 6.6 all show that the data match the Standard Model backgrounds. The individual components of the four-momenta of all the objects measured at the preselection level are well modelled with the exception of the p_{T} of the τ_{had}, which is the subject of Sec-

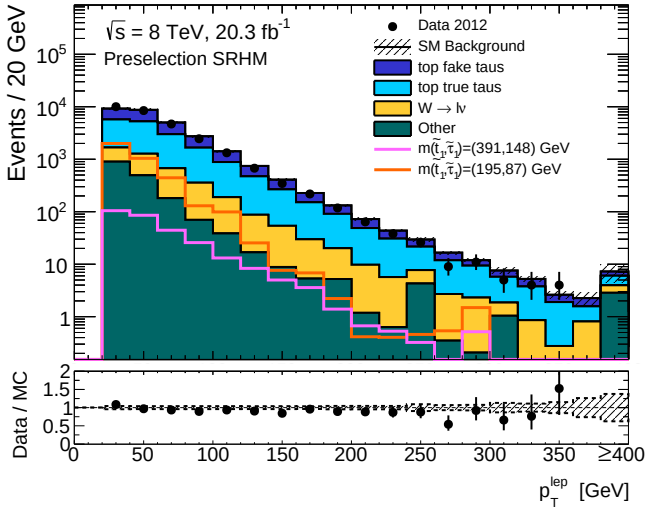

Figure 6.4: Distribution of the light charged lepton transverse momentum for events passing the SRHM preselection requirements. The contributions from all SM backgrounds are shown as a histogram stack; the bands represent the total uncertainty. The distributions expected for the two signal optimisation points are also shown. The distribution includes corrections to the p_{T} of the τ_{had}, which will be discussed in Section 6.5.7.

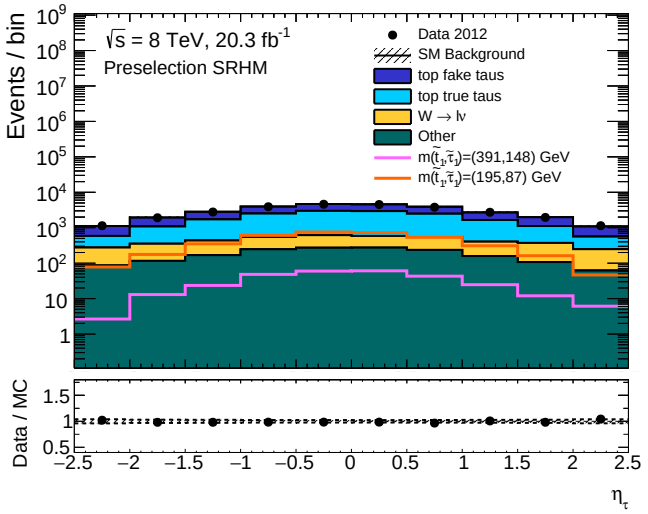

Figure 6.5: Distribution of the pseudorapidity of the hadronically decaying tau for events passing the SRHM preselection requirements. The contributions from all SM backgrounds are shown as a histogram stack; the bands represent the total uncertainty. The distributions expected for the two signal optimisation points are also shown. The distribution includes corrections to the p_{T} of the τ_{had}, which will be discussed in Section 6.5.7.

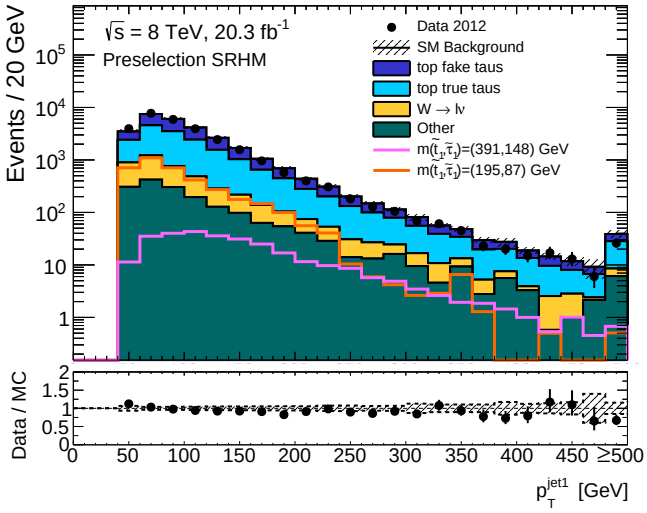

(a) p_{T} of highest-p_{T} jet

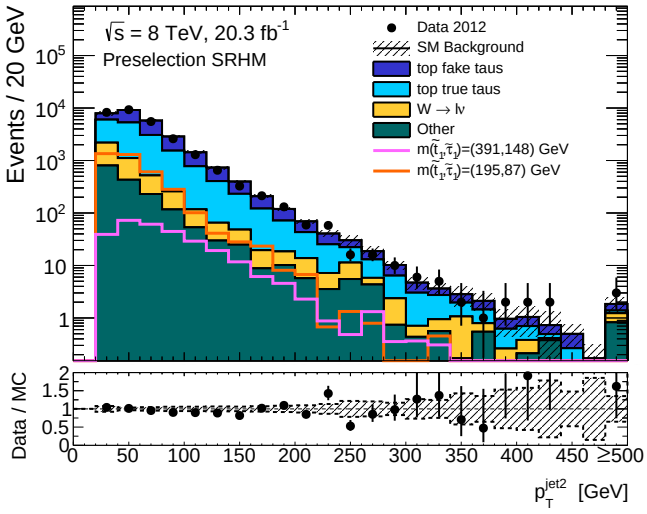

(b) p_{T} of second highest-p_{T} jet

Figure 6.6: Distributions of the transverse momenta for the highest-p_{T} (Figure 6.6a) and second-highest-p_{T} (Figure 6.6b) jets for events passing the SRHM preselection requirements. The contributions from all SM backgrounds are shown as a histogram stack; the bands represent the total uncertainty. The distributions expected for the two signal optimisation points are also shown. The distributions include corrections to the p_{T} of the τ_{had}, which will be discussed in Section 6.5.7.

tion 6.5.7. It is important that the individual components of the four-momenta of all objects are well modelled because they are the inputs to the more complex kinematic variables that perform most of the separation of the signal from the backgrounds. The modelling of the p_{T} of the light lepton is also important because the analysis uses a lepton trigger with a minimum-p_{T} threshold (see Section 4.1 and Chapter 5).

6.5.4 Dominant backgrounds after preselection

The dominant background processes in the lepton–hadron channel after the preselection cuts are $t\bar{t}$ with a real hadronically decaying tau, $t\bar{t}$ with a fake hadronically decaying tau, and W+jets with a fake hadronically decaying tau. These processes are shown in Figures 6.1 and 6.2. The three main decays of a $t\bar{t}$ system result in 0, 1, and 2 leptons (from the W boson decays) and are referred to as the fully-hadronic, semi-leptonic, and fully-leptonic channels respectively.

The $t\bar{t}$ processes with fake hadronically decaying taus include several different processes including fully-leptonic $t\bar{t}$ where one light charged lepton is not reconstructed (or "lost") and semi-leptonic $t\bar{t}$ decays where a jet (either from the W boson decay or another jet in the event) is misidentified as a hadronically decaying tau. In nearly all the $t\bar{t}$ and W+jets events passing the preselection, one W boson decays to a real electron or muon because ATLAS has a much better reconstruction efficiency and rejection power against fakes for electrons and muons than for hadronically decaying taus. The selected W+jets events nearly all include a fake hadronically decaying tau and a real light charged lepton. In $t\bar{t}$ (and Wt) events the light charged lepton comes from a W decay while the hadronically decaying tau can be real or fake.

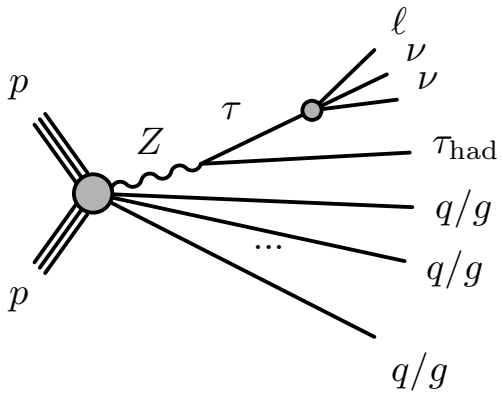

Figure 6.7: Z+jets

The remaining backgrounds are generally referred to just as "other" Standard Model processes as they contribute only a small fraction of the total number of background events after the preselection. The largest background process in the "other" grouping at the preselection level is Z/γ^*+jets (see Figure 6.7) where $Z \to \tau\tau$. Other backgrounds considered include $t\bar{t}V$, multijet events, and diboson production (VV), where $V = W$ or Z. Multijet events are events where the hard scatter is a QCD interaction. The definition excludes top quark events to avoid events being included in multiple definitions.

6.5.5 Signal region definitions

The selection cuts for the lepton–hadron low-mass and high-mass signal regions are defined in Tables 6.1 and 6.2 respectively. In the low-mass analysis, the main variable that separates the control regions, the validation region, and the signal region from each other is $m_{\mathrm{T2}}\left(\mathrm{b}\ell, \mathrm{b}\tau_{\mathrm{had}}\right)$ while $m_{\mathrm{T2}}\left(\ell, \tau_{\mathrm{had}}\right)$ is used to separate these regions in the high-mass analysis (except for the W+jets control regions where the number of b-tagged jets is used). These variables and others will be described in the following sections.

Table 6.1: Definition of the signal region SRLM used in the low-mass lepton–hadron analysis. The selections of the associated control regions for top-quark events with true hadronically decaying taus (CRTtLM), top-quark events with fake hadronically decaying taus (CRTfLM), and W+jets (CRWLM), and of the validation region (VRLM) are also given.

Region	$N_{b-\mathrm{jet}}$	$H_{\mathrm{T}}/m_{\mathrm{eff}}$	$\frac{p_{\mathrm{T}}^{\ell}+p_{\mathrm{T}}^{\tau_{\mathrm{had}}}}{m_{\mathrm{eff}}}$	$m_{\mathrm{T2}}(b\ell, b)$	$m_{\mathrm{T2}}(b\ell, b\tau_{\mathrm{had}})$	$m_{\mathrm{T}}(\ell, p_{\mathrm{T}}^{\mathrm{miss}})$	m_{eff}
SRLM	≥ 2	< 0.5	> 0.2	< 100 GeV	< 60 GeV	-	-
CRTtLM	≥ 2	-	> 0.2	< 100 GeV	$110 - 160$ GeV	> 100 GeV	-
CRTfLM	≥ 2	-	> 0.2	< 100 GeV	$110 - 160$ GeV	< 100 GeV	-
CRWLM	0	< 0.5	> 0.2	-	-	> 40 GeV	< 400 GeV
VRLM	≥ 2	> 0.5	> 0.2	< 100 GeV	$60 - 110$ GeV	-	-

Table 6.2: Definition of the signal region SRHM used in the high-mass lepton–hadron analysis. The selections of the associated control regions for top-quark events with true hadronically decaying taus (CRTtHM), top-quark events with fake hadronically taus (CRTfHM), and W+jets (CRWHM), and of the validation region (VRHM) are also given.

Region	$N_{b-\text{jet}}$	$E_{\text{T}}^{\text{miss}}$	m_{eff}	$H_{\text{T}}/m_{\text{eff}}$	$m_{\text{T2}}(b\ell, b\tau_{\text{had}})$	$m_{\text{T2}}(\ell, \tau_{\text{had}})$	$m_{\text{T}}(\ell, p_{\text{T}}^{\text{miss}})$
SRHM	≥ 1	> 150 GeV	> 400 GeV	< 0.5	> 180 GeV	> 120 GeV	-
CRTtHM	≥ 1	> 150 GeV	> 400 GeV	< 0.5	> 180 GeV	20-80 GeV	> 120 GeV
CRTfHM	≥ 1	> 150 GeV	> 400 GeV	< 0.5	> 180 GeV	20-80 GeV	< 120 GeV
CRWHM	0	> 150 GeV	> 400 GeV	< 0.5	-	20-80 GeV	40-100 GeV
VRHM	≥ 1	< 150 GeV	> 400 GeV	< 0.5	> 180 GeV	> 80 GeV	-

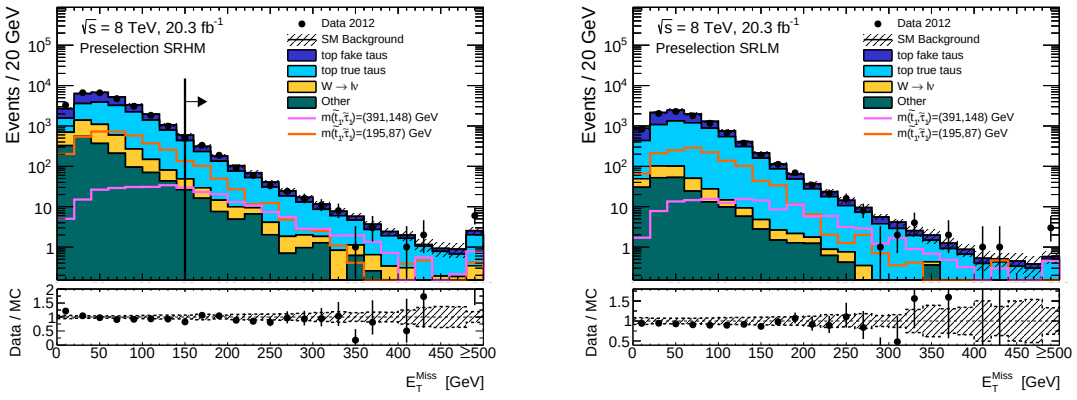

(a) $E_{\text{T}}^{\text{miss}}$ - SRHM preselection

(b) $E_{\text{T}}^{\text{miss}}$ - SRLM preselection

Figure 6.8: Distributions of the missing transverse momentum for events passing the SRHM preselection requirements (Figure 6.8a) and the SRLM preselection requirements (Figure 6.8b). The contributions from all SM backgrounds are shown as a histogram stack; the bands represent the total uncertainty. The distributions expected for the two signal optimisation points are also shown. The distributions include corrections to the p_{T} of the τ_{had}, which will be discussed in Section 6.5.7. The two distributions show how the size of the W+jets background changes as a function of the number of b-tagged jets required by the selection (to be discussed in Section 6.5.6). The line and arrow show the cut on the plotted variable that is required for the SRHM selection.

Several kinematic variables are used to separate the signal from background. The missing transverse momentum is plotted in Figure 6.8 after the preselection cuts. For

the SRHM selection a minimum value is placed on this variable. This is because the signal model has a larger number of invisible particles than the dominant backgrounds. This cut becomes more efficient as the mass of the scalar top increases because increasing the mass of the scalar top increases the boost to the invisible particles from its decay, and thus increases the missing transverse momentum. No cut is placed on the $E_{\mathrm{T}}^{\mathrm{miss}}$ in the low-mass selection.

Three m_{T2} variables are employed in the lepton–hadron selections with different choices for the visible object 4-momenta defined in equation 6.2:

- $m_{\mathrm{T2}}\left(\mathrm{b}\ell, \mathrm{b}\tau_{\mathrm{had}}\right)$ is calculated using the two jets with the highest b-tagging weights paired with the light charged lepton and the τ_{had}. One of these two jets is paired with the light charged lepton and the other with the τ_{had}. The four-momentum vectors of the two resulting pairs of particles are then used in the m_{T2} algorithm. The missing transverse momentum is assumed to be created by two invisible massless particles. For $t\bar{t}$ events where the b quark and the charged lepton belong to the decay of the same top quark, this variable is bounded from above by the top-quark mass. Similarly, for signal events, the upper bound on this variable is the scalar top mass. A maximum-value cut is therefore used in the low-mass selection and a minimum-value cut in the high-mass selection with the values of the cuts chosen with respect to the top-quark mass.

  The distribution for $m_{\mathrm{T2}}\left(\mathrm{b}\ell, \mathrm{b}\tau_{\mathrm{had}}\right)$ after the SRLM preselection is shown in Figure 6.9. The figure includes two overlaid signal models (the low-mass and high-mass optimisation points) to show the separation between the signal and the sum of the SM backgrounds. In both the low-mass and high-mass selections the $m_{\mathrm{T2}}\left(\mathrm{b}\ell, \mathrm{b}\tau_{\mathrm{had}}\right)$ variable is used to distinguish the scalar tops in the signal from the top quarks in the dominant $t\bar{t}$ backgrounds. The high-mass signal region targets heavy scalar tops by requiring $m_{\mathrm{T2}}\left(\mathrm{b}\ell, \mathrm{b}\tau_{\mathrm{had}}\right) > 180$ GeV and the low-mass signal region targets light scalar tops by requiring $m_{\mathrm{T2}}\left(\mathrm{b}\ell, \mathrm{b}\tau_{\mathrm{had}}\right) < 60$ GeV.

  An ambiguity exists in the pairing of the two jets with the two leptons. Only the pairings for which the invariant masses $m(b\ell)$ and $m(b\tau_{\mathrm{had}})$ are both smaller than $m(t)$ are considered[1]. If exactly one pairing satisfies the condition, that

[1]For top-quark pair production events where the lepton and the jet belong to the decay of the same top quark, the invariant mass has an upper bound at $\sqrt{m_t^2 - m_W^2}$, approximately 152 GeV. The algorithm tries to select pairs that satisfy this condition, loosened to account for the detector resolution.

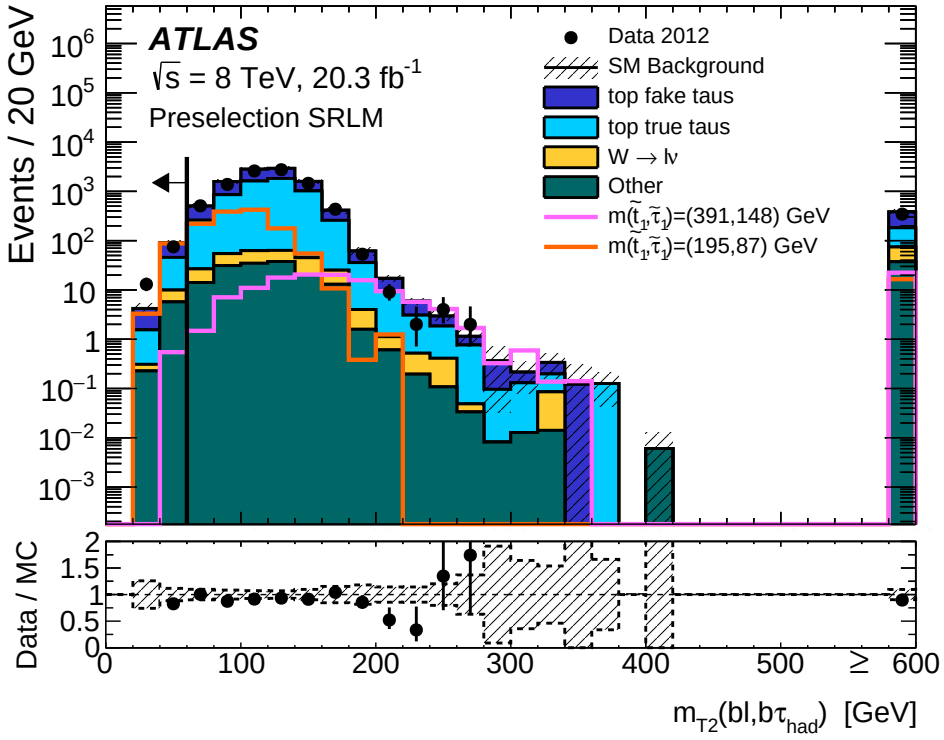

Figure 6.9: Distribution of the stransverse mass constructed from the b-jet plus light charged lepton and b-jet plus τ_{had}, $m_{\text{T2}}\,(\text{b}\ell, \text{b}\tau_{\text{had}})$, for events passing the SRLM preselection requirements. The contributions from all SM backgrounds are shown as a histogram stack; the bands represent the total uncertainty. The overflow bin in the $m_{\text{T2}}\,(\text{b}\ell, \text{b}\tau_{\text{had}})$ plot is filled with the events that have no $(b\ell, b\tau_{\text{had}})$ pairing satisfying $m(b\ell) < m_t$ and $m(b\tau_{\text{had}}) < m_t$. The distributions expected for the two signal optimisation points are also shown. The distribution includes corrections to the p_{T} of the τ_{had}, which will be discussed in Section 6.5.7. This figure was taken from Reference [57] and the line and arrow were overlayed on top of it. The line and arrow show the cut on the plotted variable that is required for the SRLM selection.

pairing is used in the m_{T2} calculation. If both pairings satisfy the condition, m_{T2} is calculated for both pairings and the smaller value is taken. If no pairing satisfies the condition, the event is considered to have passed the $m_{\text{T2}}\,(\text{b}\ell, \text{b}\tau_{\text{had}})$ selection for the high-mass signal region and to have failed it for the low-mass signal region.

- $m_{\text{T2}}\,(\ell, \tau_{\text{had}})$ is only used for the high-mass selection. It uses the momenta of the light charged lepton and the hadronically decaying tau. The missing transverse momentum is assumed to result from two invisible massless particles. For events

where the light charged lepton, the hadronically decaying tau, and the missing transverse momentum originate from the decay of a pair of W bosons, this variable is bounded from above by the W boson mass. This is the case for the majority of the background events (e.g. $t\bar{t}$ events). The high-mass selection requires $m_{\mathrm{T2}}(\ell, \tau_{\mathrm{had}})$ to be large because this variable's distribution for signal models with heavy scalar taus and scalar tops peaks at higher values than for the dominant SM background. The cut is also set relatively high because the variable is sensitive to the mass of the scalar tau and SRHM is designed to focus on higher mass scalar taus while the hadron–hadron channel focuses on lower mass scalar taus.

The distribution for $m_{\mathrm{T2}}(\ell, \tau_{\mathrm{had}})$ after the SRHM preselection cuts is shown in Figure 6.10. The figure includes the overlaid optimisation points to show the separation between the signal and the sum of the SM backgrounds. The high-mass selection requires $m_{\mathrm{T2}}(\ell, \tau_{\mathrm{had}}) > 120$ GeV to separate heavy scalar taus in the signal from the W bosons in the dominant $t\bar{t}$ background.

- $m_{\mathrm{T2}}(\mathrm{b}\ell, \mathrm{b})$ is only used for the low-mass selection. The two jets with the highest-b-tagging weights are selected as the two b quarks for this algorithm, which is the same procedure as is done with $m_{\mathrm{T2}}(\mathrm{b}\ell, \mathrm{b}\tau_{\mathrm{had}})$. The system of one of the b-jets and the light charged lepton is considered as the first visible four-momentum. Only pairings for which $m(b\ell) < m_t$ are considered. If neither pairing satisfies the condition, the event is discarded. If both pairings satisfy the condition then the pairing that yields the smaller value of $m_{\mathrm{T2}}(\mathrm{b}\ell, \mathrm{b})$ is used. The invisible particle associated with this system is assumed to be massless. The other b-jet is the second visible system used in the m_{T2} calculation. The $m_{\mathrm{T2}}(\mathrm{b}\ell, \mathrm{b})$ variable targets fully-leptonic $t\bar{t}$ events where one lepton from a W boson decay is not detected or identified and so the full W boson is lost. To correct for this, the mass of the associated invisible particle in the second system is set to the W boson mass. For the dominant $t\bar{t}$ background, the $m_{\mathrm{T2}}(\mathrm{b}\ell, \mathrm{b})$ variable is bounded from above by the top-quark mass.

  The distribution for $m_{\mathrm{T2}}(\mathrm{b}\ell, \mathrm{b})$ after the SRLM preselection is shown in Figure 6.11. The figure has the optimisation points overlaid to show the separation between the signal and the sum of the SM backgrounds. The $m_{\mathrm{T2}}(\mathrm{b}\ell, \mathrm{b})$ variable is used to distinguish the scalar tops in the signal from the top quarks in the dominant $t\bar{t}$ backgrounds. This variable has a softer distribution for low-mass

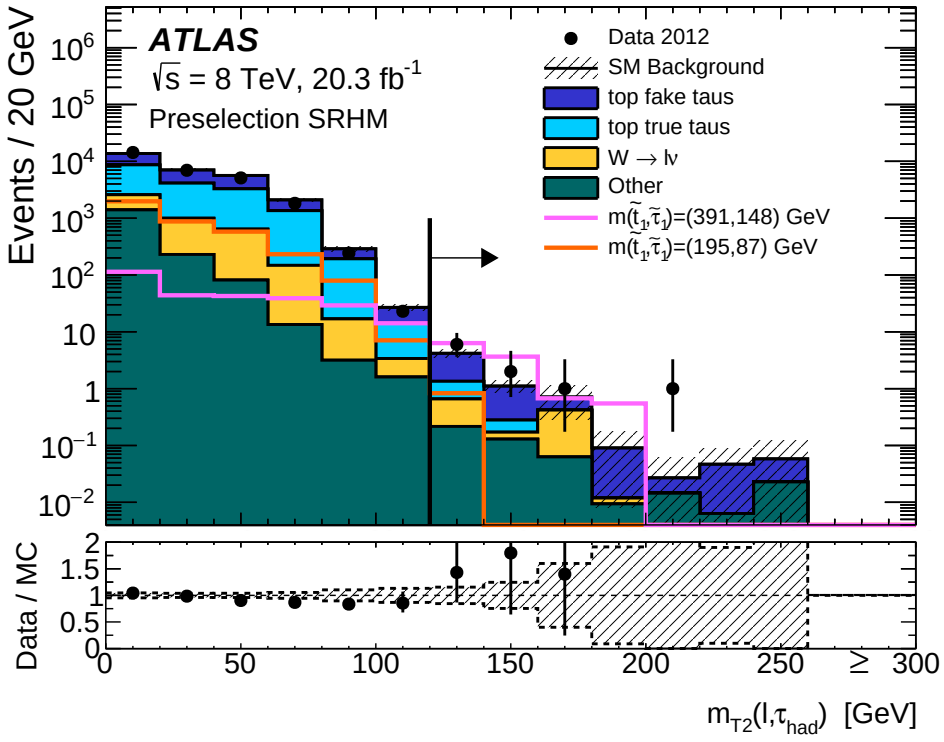

Figure 6.10: Distribution of the stransverse mass constructed from the momenta of the light charged lepton and the hadronically decaying tau, $m_{\mathrm{T2}}(\ell, \tau_{\mathrm{had}})$, for events passing the SRHM preselection requirements. The contributions from all SM backgrounds are shown as a histogram stack; the bands represent the total uncertainty. The distributions expected for the two signal optimisation points are also shown. The distribution includes corrections to the p_{T} of the τ_{had}, which will be discussed in Section 6.5.7. This figure was taken from Reference [57] and the line and arrow were overlayed on top of it. The line and arrow show the cut on the plotted variable that is required for the SRHM selection.

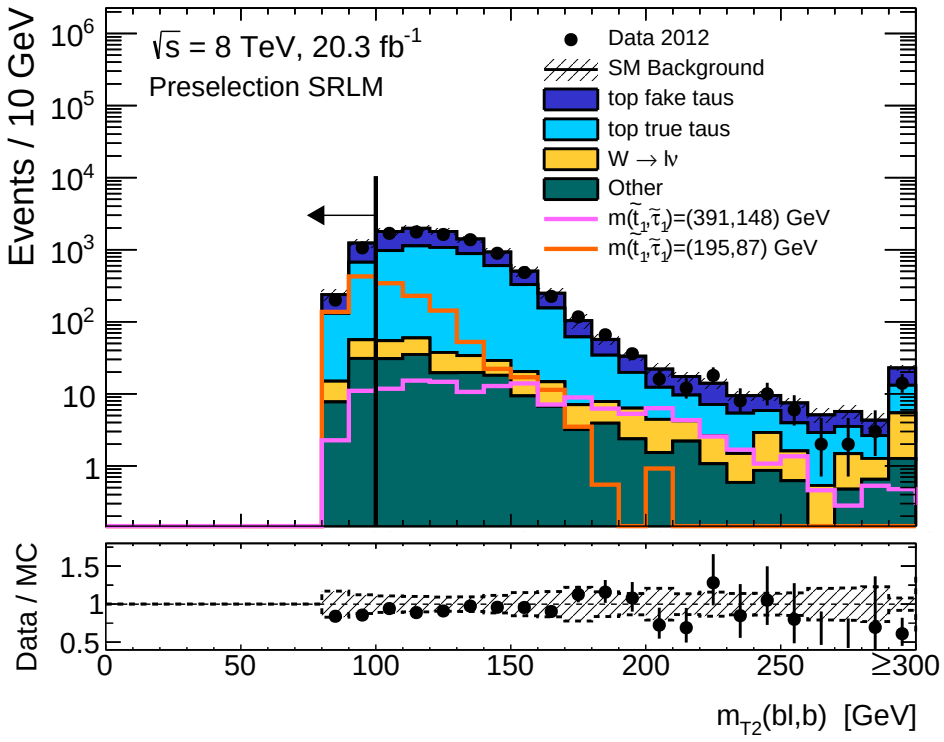

Figure 6.11: Distribution of the stransverse mass constructed from the b-jet plus light charged lepton and the second b-jet, $m_{\mathrm{T2}}\,(\mathrm{b}\ell, \mathrm{b})$, for events passing the SRLM preselection requirements. The contributions from all SM backgrounds are shown as a histogram stack; the bands represent the total uncertainty. The distributions expected for the two signal optimisation points are also shown. The distribution includes corrections to the p_{T} of the τ_{had}, which will be discussed in Section 6.5.7. The line and arrow show the cut on the plotted variable that is required for the SRLM selection.

signal events than for the dominant $t\bar{t}$ background and so the low-mass selection requires $m_{\mathrm{T2}}\,(\mathrm{b}\ell, \mathrm{b})$ to be less than 100 GeV.

Several other kinematic variables are used to separate the signal from the dominant backgrounds. The scalar sums of the p_{T} of the objects in the event can provide rough information about the masses of the parent particles in the event. The m_{eff} (see Figure 6.12) includes contributions from all the decay products of the scalar top system under study and so it can act as a very rough probe into the mass of the scalar top. This figure will be discussed further in Chapter 8. The light charged lepton and the τ_{had} are decay products of the scalar tau and so the scalar sum of their transverse momenta is related to the scalar tau mass. Ratios of these scalar sums can then also provide

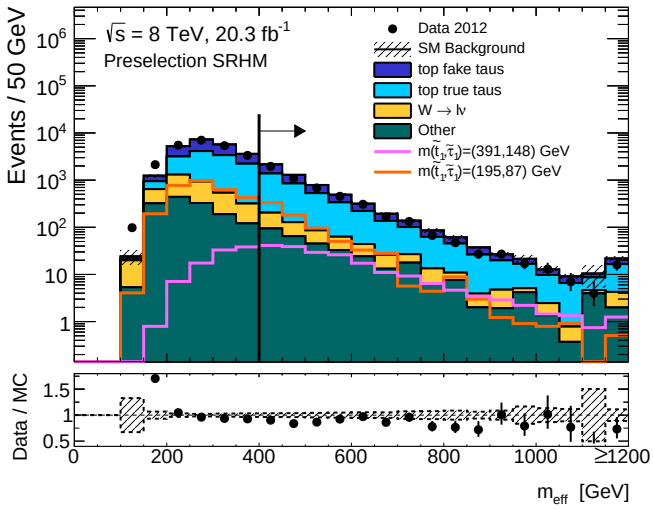

Figure 6.12: Distribution of the m_{eff} for events passing the SRHM preselection requirements. The contributions from all SM backgrounds are shown as a histogram stack; the bands represent the total uncertainty. The distributions expected for the two signal optimisation points are also shown. The distributions include corrections to the p_{T} of the τ_{had}, which will be discussed in Section 6.5.7. The line and arrow show the cut on the plotted variable that is required for the SRHM selection.

rough information about the relative masses of the parent particles in the event.

In both the lepton–hadron signal regions $H_{\text{T}}/m_{\text{eff}}$ (see Section 6.5.2 for variable definitions) is required to be less than 0.5. This cut targets signal models with smaller mass differences between the scalar top and scalar tau (i.e. $m_{\tilde{t}_1} - m_{\tilde{\tau}_1}$ is small) because the p_{T} of the two b-jets from the decay of the scalar tops into the scalar taus is forced to be relatively small compared to the p_{T} of the charged lepton decay products of the scalar tau and thus also relatively small compared to the total scalar sum p_{T} in the event (see Figure 2.11). The $H_{\text{T}}/m_{\text{eff}}$ cut can also distinguish the three-body decays of the scalar top from the two-body decays of the dominant $t\bar{t}$ backgrounds. The three-body decays of the scalar top produce more invisible particles than the two-body decays of the $t\bar{t}$ background, thus creating a larger $E_{\text{T}}^{\text{miss}}$. The larger $E_{\text{T}}^{\text{miss}}$ results in a larger m_{eff}, and thus a smaller $H_{\text{T}}/m_{\text{eff}}$. The distribution of $H_{\text{T}}/m_{\text{eff}}$ after the SRHM preselection cuts is plotted in Figure 6.13. This variable does not provide as good separation power at the optimisation points as some of the variables so the maximum cut values for both SRLM and SRHM are not very small. Other variable selections used in the two signal regions (e.g. $E_{\text{T}}^{\text{miss}} > 150$ GeV in SRHM) are correlated to $H_{\text{T}}/m_{\text{eff}}$ and remove events that have higher values of the $H_{\text{T}}/m_{\text{eff}}$.

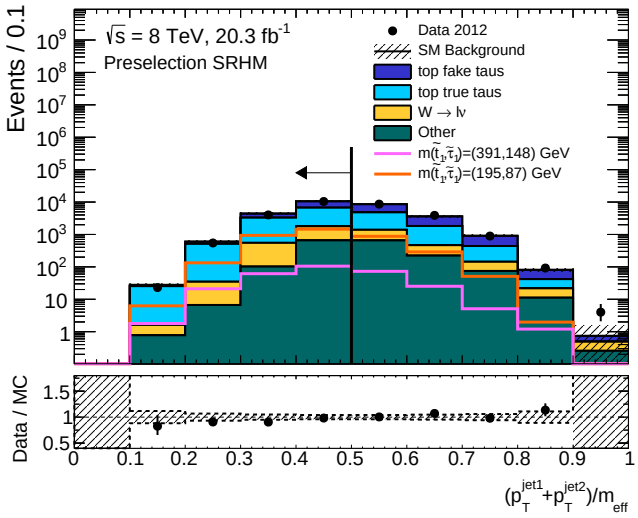

Figure 6.13: Distribution of the $H_{\mathrm{T}}/m_{\mathrm{eff}}$ for events passing the SRHM preselection requirements. The contributions from all SM backgrounds are shown as a histogram stack; the bands represent the total uncertainty. The distributions expected for the two signal optimisation points are also shown. The distributions include corrections to the p_{T} of the τ_{had}, which will be discussed in Section 6.5.7. The line and arrow show the cut on the plotted variable that is required for the SRHM selection.

As is visible from the $H_{\mathrm{T}}/m_{\mathrm{eff}}$ distribution, the separation power starts to decrease as $H_{\mathrm{T}}/m_{\mathrm{eff}}$ goes above approximately 0.5. A cut value of 0.5 on $H_{\mathrm{T}}/m_{\mathrm{eff}}$ is used to define the signal regions.

The low-mass selection requires $\left(p_{\mathrm{T}}^{\ell} + p_{\mathrm{T}}^{\tau_{\mathrm{had}}}\right)/m_{\mathrm{eff}} > 0.2$. This cut targets signal points that have smaller mass differences between the scalar top and the scalar tau. When the mass difference between the scalar top and scalar tau is small then the charged lepton decay products of the scalar tau will have relatively large p_{T} compared to the p_{T} of the b-jets, which leads to the momenta of the charged lepton decay products of the scalar tau also being large compared to m_{eff}. This reasoning is the same as was used to explain the $H_{\mathrm{T}}/m_{\mathrm{eff}}$ cut. For the majority of the mass points being targeted by the low-mass selection the difference in mass between the scalar top and the scalar tau will be smaller than the difference in mass between the top quark and the W boson because the scalar top is lighter than the top quark and the LEP limit of 87 GeV on the scalar tau mass implies that the scalar tau is more massive than the W boson (see Section 6.1). This cut provides some separation of the signal from the dominant $t\bar{t}$ background because of the different mass differences. Even in the case of the optimisation point where the mass difference in the signal is actually slightly larger

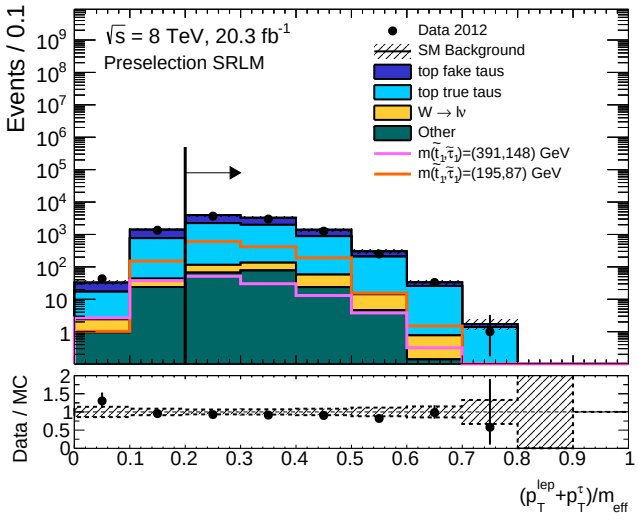

Figure 6.14: Distribution of the $(p_{\mathrm{T}}^{\ell} + p_{\mathrm{T}}^{\tau_{\mathrm{had}}})/m_{\mathrm{eff}}$ for events passing the SRLM preselection requirements. The contributions from all SM backgrounds are shown as a histogram stack; the bands represent the total uncertainty. The distributions expected for the two signal optimisation points are also shown. The distributions include corrections to the p_{T} of the τ_{had}, which will be discussed in Section 6.5.7. The line and arrow show the cut on the plotted variable that is required for the SRLM selection.

than the mass difference in the dominant $t\bar{t}$ background, the three-body nature of the signal producing a large $E_{\mathrm{T}}^{\mathrm{miss}}$ still gives the $\left(p_{\mathrm{T}}^{\ell} + p_{\mathrm{T}}^{\tau_{\mathrm{had}}}\right)/m_{\mathrm{eff}} > 0.2$ cut separation power between the signal and background. The distribution for $\left(p_{\mathrm{T}}^{\ell} + p_{\mathrm{T}}^{\tau_{\mathrm{had}}}\right)/m_{\mathrm{eff}}$ after the SRLM preselection cuts is shown in Figure 6.14. At the optimisation point, other variables provide better separation power than this one so the cut on this variable is relatively soft.

The set of cuts for each signal region has associated with it a signal selection efficiency. The low-mass signal region has a signal efficiency around 0.01% in the scalar top mass range of 150 to 200 GeV. At the $(m_{\tilde{t}_1}, m_{\tilde{\tau}_1}) = (195, 87)$ GeV optimisation point the low-mass signal region has a signal efficiency of 1.36×10^{-4}. The high-mass signal region has a signal efficiency that increases with the scalar top mass and also increases with the scalar tau mass. The efficiency of the high-mass selection varies between 0.0007% and 1% for a scalar top mass between 200 and 700 GeV. At the $(m_{\tilde{t}_1}, m_{\tilde{\tau}_1}) = (391, 148)$ GeV optimisation point the high-mass signal region has a signal efficiency of 9.44×10^{-4}. These efficiencies include the signal region selection cuts, the preselection cuts, the decay branching ratios, the detector acceptance, and the identification and trigger efficiencies. The detector acceptance is partly determined

by the geometric coverage of the different sub-detectors (see Chapter 3). The muon reconstruction efficiency is fairly high but the τ_{had} identification efficiency and the b-tagging efficiency are not (see Section 4.2). These efficiencies are discussed further in Section 9.2.4.

6.5.6 Control regions and validation regions definitions

The selection cuts for the low-mass and high-mass control and validation regions are defined in Tables 6.1 and 6.2 respectively. For the selection regions, plots will be shown where all the selections have been applied except for the variable being plotted. These will be referred to as "N-1" plots.

The variables used to define SRLM and SRHM are also used in the definitions of the control and validation regions. One variable used in defining the control and validation regions that is not used in the signal region definitions is the transverse mass, $m_{\text{T}}\left(\ell, p_{\text{T}}^{\text{miss}}\right)$. For both the low-mass and the high-mass selections, the main variables used to separate the control and validation regions from their respective signal regions are the number of b-tagged jets, $H_{\text{T}}/m_{\text{eff}}$, $E_{\text{T}}^{\text{miss}}$, the transverse mass, and a stransverse mass variable. The low-mass selections use $m_{\text{T2}}\left(\text{b}\ell, \text{b}\tau_{\text{had}}\right)$ to separate top-quark events from scalar top events while the high-mass selections use $m_{\text{T2}}\left(\ell, \tau_{\text{had}}\right)$. See Section 6.5.5 for a description of how these stransverse mass variables separate the signal from the dominant backgrounds. The validation regions are separated from the signal regions in part by using $H_{\text{T}}/m_{\text{eff}}$ in the low-mass analysis and $E_{\text{T}}^{\text{miss}}$ in the high-mass analysis. Inverting the selection cuts on these two variables allows for a reasonable number of events in both the signal regions and the validation regions.

The fraction of W+jets events with at least one b-jet is small. This is also true of nearly all the "other" background processes. However, the decay of a top quark almost always produces a b-jet so the number of b-tagged jets can be used to separate W+jets events from top-quark events. Increasing the required number of b-tagged jets per event decreases the relative fraction of W+jets events to $t\bar{t}$ events, which can be seen by comparing the two missing transverse momentum plots in Figure 6.8. In this figure, increasing the number of b-tagged jets reduces the relative number of W+jets and "other" events (orange+green) to the sum of the Standard Model backgrounds across the whole distribution. Phrased differently, Figure 6.8b has a much larger fractional surface area covered by the blue backgrounds than Figure 6.8a does. The control regions for W+jets require the number of b-tagged jets to be zero. The $t\bar{t}$

control regions and the validation regions require the same number of b-tagged jets as their associated signal region.

The transverse mass variable made with the light charged lepton and the missing transverse momentum, $m_{\mathrm{T}}\left(\ell, p_{\mathrm{T}}^{\mathrm{miss}}\right)$, is used for two main purposes. Firstly, it is used to distinguish W+jets events from multijet events with the cut $m_{\mathrm{T}}\left(\ell, p_{\mathrm{T}}^{\mathrm{miss}}\right) > 40$ GeV. Multijet events contain only jets and do not have real prompt light charged leptons nor large amounts of missing transverse energy. A large amount of missing transverse energy in a multijet event is likely to be the result of incorrectly reconstructing the momenta of one or more jets. Reconstructed light charged leptons in multijet events are actually mis-identified jets or non-prompt light charged leptons (e.g. from the leptonic decay of a heavy flavoured hadron in a jet). The $E_{\mathrm{T}}^{\mathrm{miss}}$ in multijet events is generally parallel to the lepton, which is the jet with the misreconstructed energy. This cut distinguishes multijet events from W+jets events because it removes some of the events with small amounts of $E_{\mathrm{T}}^{\mathrm{miss}}$ while also taking into account the direction of the $p_{\mathrm{T}}^{\mathrm{miss}}$ with respect to the light charged lepton.

The transverse mass calculated using the light charged lepton and $p_{\mathrm{T}}^{\mathrm{miss}}$ is also used to distinguish events with real hadronically decaying taus from events with fake hadronically decaying taus in the dominant top-quark background. This quantity is shown in Figure 6.15 in the low-mass and high-mass top control regions where all the cuts except the transverse mass cut have been applied. The transverse mass is sensitive to the number of invisible particles that contribute towards the missing transverse momentum. If the hadronically decaying tau is fake then one of the W bosons is more likely to have decayed hadronically and not produced any invisible particles. This implies that the $p_{\mathrm{T}}^{\mathrm{miss}}$ only comes from one $W \to \ell\nu$ decay, which should produce $m_{\mathrm{T}}\left(\ell, p_{\mathrm{T}}^{\mathrm{miss}}\right) < m(W)$. In a fully-leptonic $t\bar{t}$ decay with a true hadronically decaying tau and a light charged lepton there will be two invisible particles from the two W boson decays. This results in a larger value of $m_{\mathrm{T}}\left(\ell, p_{\mathrm{T}}^{\mathrm{miss}}\right)$, which is not limited by $m(W)$. In the high-mass selection a cut of $m_{\mathrm{T}}\left(\ell, p_{\mathrm{T}}^{\mathrm{miss}}\right) > 120$ GeV is used to isolate the $t\bar{t}$ events with a real τ_{had} while a cut of $m_{\mathrm{T}}\left(\ell, p_{\mathrm{T}}^{\mathrm{miss}}\right) < 120$ GeV is used to isolate the events with a fake τ_{had}. For the low-mass selection a cut of 100 GeV is used. The cut values are set to values larger than the W boson mass to increase the purity of the true τ_{had} events in the associated control regions, while also striking a balance with the total number of events in each $t\bar{t}$ control region and the purity of fake hadronically decaying taus in the $t\bar{t}$ fake-τ_{had} control regions.

Finally for the low-mass regions, a cut on m_{eff} is also applied to the W+jets control

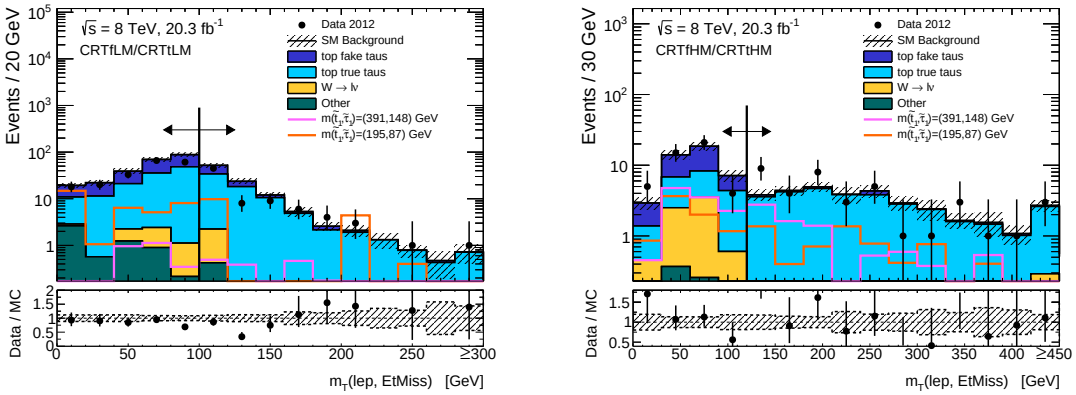

(a) $m_{\mathrm{T}}\left(\ell, p_{\mathrm{T}}^{\mathrm{miss}}\right)$ for CRTtLM + CRTfLM

(b) $m_{\mathrm{T}}\left(\ell, p_{\mathrm{T}}^{\mathrm{miss}}\right)$ for CRTtHM + CRTfHM

Figure 6.15: CRT N-1: Distributions of the transverse mass made with the light charged lepton, $m_{\mathrm{T}}\left(\ell, p_{\mathrm{T}}^{\mathrm{miss}}\right)$, for events passing all the low-mass and high-mass top control region selections except that on $m_{\mathrm{T}}\left(\ell, p_{\mathrm{T}}^{\mathrm{miss}}\right)$. Figure 6.15a is the combination of CRTtLM + CRTfLM, while Figure 6.15b is the combination of CRTtHM + CRTfHM. The distributions show how the transverse mass variable is used to separate true hadronically decaying taus from fake hadronically decaying taus. The contributions from all SM backgrounds are shown as a histogram stack; the bands represent the total uncertainty. The distributions expected for the two signal optimisation points are also shown. The distributions include corrections to the p_{T} of the τ_{had}, which will be discussed in Section 6.5.7. The lines and arrows show the cuts on the plotted variables that are required to separate the CRTtLM selection from the CRTfLM selection as well as the CRTtHM selection from the CRTfHM selection.

region. For the high-mass regions a large amount of total activity in the detector is expected from a heavy scalar top so m_{eff} is required to be larger than 400 GeV (see Figure 6.12). The cut on m_{eff} is used in the low-mass selection for orthogonality. All the low-mass regions are by design "orthogonal" to each other (they do not share events). All the high-mass regions are orthogonal to each other as well. The cuts were selected to guarantee this property. Orthogonality reduces correlations between regions. If regions are allowed to share events then the correlations must be taken into account to avoid incorrectly normalising the backgrounds and artificially creating fake signals or masking real signals. In the low-mass analysis, the main variable that separates the control regions, the validation region, and the signal region from each other is $m_{\mathrm{T2}}\left(\mathrm{b}\ell, \mathrm{b}\tau_{\mathrm{had}}\right)$ while $m_{\mathrm{T2}}\left(\ell, \tau_{\mathrm{had}}\right)$ is used to separate these regions in the high-mass analysis (except for the W+jets control regions where the number of b-tagged jets is used). The signal regions from all three channels are made orthogonal

to each other by use of cuts on the number of selected light charged leptons. The two signal regions in the lepton–hadron channel are made orthogonal to each other by use of the $m_{\mathrm{T2}}\left(\mathrm{b}\ell, \mathrm{b}\tau_{\mathrm{had}}\right)$ variable. In the lepton–hadron analysis all the low-mass regions are orthogonal to all the high-mass regions. This arises naturally from the cuts on the $m_{\mathrm{T2}}\left(\mathrm{b}\ell, \mathrm{b}\tau_{\mathrm{had}}\right)$ variable with the exception of CRWLM, which is explicitly made orthogonal to CRWHM by a $m_{\mathrm{eff}} < 400$ GeV cut.

6.5.7 Tau momentum reweighting

The simulation of events is very important in the estimation of the background processes in this analysis but some aspects are difficult to reproduce accurately in a simulation. The hadronic decay of a tau lepton is simulated well but the simulation of a jet that is mis-reconstructed as a hadronically decaying tau may not be done as well because in general it is difficult to make dedicated samples of events with faked objects. To ensure that the fake hadronically decaying tau background is properly estimated, the properties of the fake hadronically deaying taus are validated. It was found that the momentum of the hadronically decaying taus is not well modelled in W+jets events. This was studied further in a specially designed region with loose cuts that are similar to both the preselection and the W+jets control region selection cuts. This region requires there to be exactly one *tight* electron or muon with $p_{\mathrm{T}} > 25$ GeV and no additional *tight* electrons or muons of $p_{\mathrm{T}} > 10$ GeV. Exactly one hadronically decaying tau is required and it must have the opposite charge to that of the light charged lepton. A cut on the transverse mass is used to prevent multijet events from entering this control sample, $m_{\mathrm{T}}\left(\ell, p_{\mathrm{T}}^{\mathrm{miss}}\right) > 40$ GeV. Each event must have at least two jets and the highest-p_{T} jet must have $p_{\mathrm{T}} > 50$ GeV. Finally the number of b-tagged jets must be zero. This selection is referred to as the "W-tau loose-selection".

The number of observed events in data divided by the number of events predicted by simulation (after the subtraction of non-W backgrounds) as a function of p_{T} is made for both the electron and muon channels independently and the best-fit functions are determined for both channels. The fit to the electron events should be consistent with the fit to the muon events. The fits are performed separately to test that they come out the same and are indeed found to be very similar. A reweighting value is then calculated on an event-by-event basis from the fit function based on the p_{T} of the τ_{had}.

The hadronically decaying tau p_{T} after the W-tau loose-selection is shown in

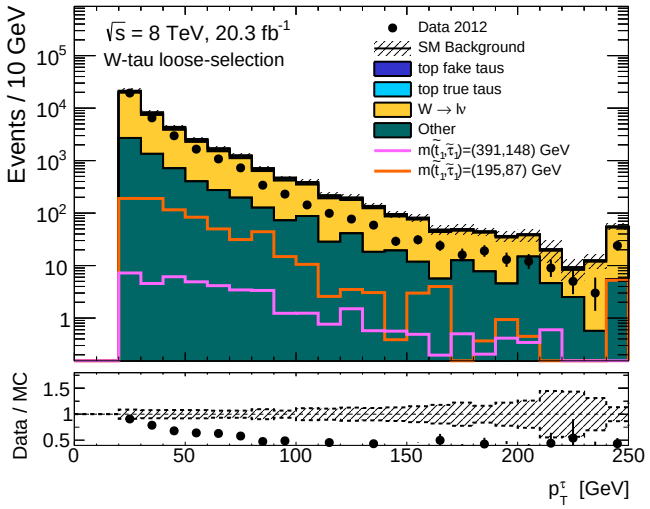

Figure 6.16: Distribution of the transverse momentum of the hadronically decaying tau for events passing the selection requirements of the W-tau loose-selection. The contributions from all SM backgrounds are shown as a histogram stack; the bands represent the total uncertainty. The distributions expected for the two signal optimisation points are also shown. The distribution shows how the p_{T} of the τ_{had} is not well modelled for W+jets events. This distribution does *not* include the τ_{had} momentum correction.

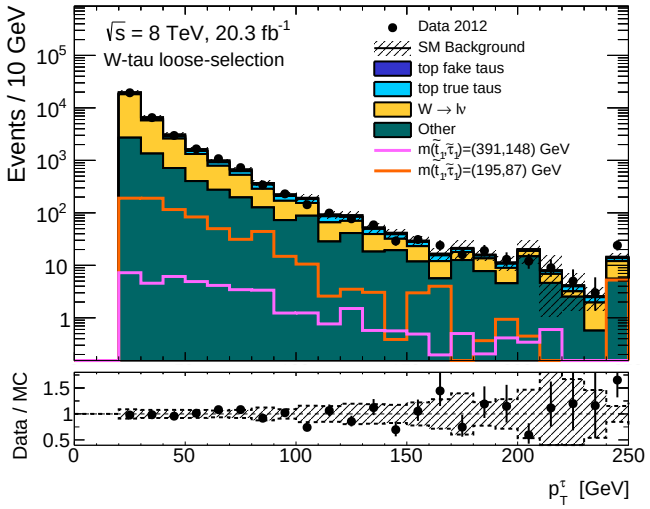

Figure 6.17: Distribution of the transverse momentum of the hadronically decaying tau for events passing the selection requirements of the W-tau loose-selection after the momentum correction has been applied. The contributions from all SM backgrounds are shown as a histogram stack; the bands represent the total uncertainty. The distributions expected for the two signal optimisation points are also shown. The reweighted distribution agrees with the data.

Table 6.3: Background normalisation parameters derived from the likelihood fits.

	Low-mass regions	High-mass regions
$t\bar{t}$ with true τ	0.71 ± 0.24	1.21 ± 0.22
$t\bar{t}$ with fake τ	0.98 ± 0.33	1.13 ± 0.41
W+jets	0.94 ± 0.04	0.61 ± 0.17

Figure 6.16. The same distribution, but including the reweighting of the p_{T} of the τ_{had}, is shown in Figure 6.17. The hadronically decaying tau p_{T} is also shown for the CRWLM and CRWHM regions in Figure 6.18 after the hadronically decaying tau p_{T} reweighting and it is apparent that the reweighted distributions match the data. The reweighting does not preserve the overall number of events in CRWLM and CRWHM. The reweighting of the τ_{had} p_{T} is done for all W+jets MC events and all plots in this dissertation are made using this reweighting unless specified otherwise.

6.6 Background-only fit results

The overall number of events for each process has to be accurately estimated. The background processes that are expected to contribute only a small number of events to the signal regions are all estimated using Monte Carlo simulations. The dominant backgrounds, however, are estimated by scaling the total numbers of simulated events to the data to correct for mismodelling. The numbers of events from simulation and data are measured in the control regions and then a simultaneous fit, the background-only fit, is performed to calculate the scale factors. This fit assumes that there is no signal in the control regions and that they contain only background events.

The background-only fits are performed independently for the low-mass and high-mass analyses. Each fit produces a scale factor for each of the three dominant processes, and these are shown in Table 6.3. Typically a scale factor of 1 implies that the simulation accurately modelled the associated process in the selected region of phase space. This is not entirely true with the fits in this analysis because the hadronically decaying tau p_{T} reweighting of the W+jets events also changes the overall number of W+jets events.

The fit is performed by maximising the likelihood function where the systematic uncertainties (to be described in Chapter 7) are included as nuisance parameters. The

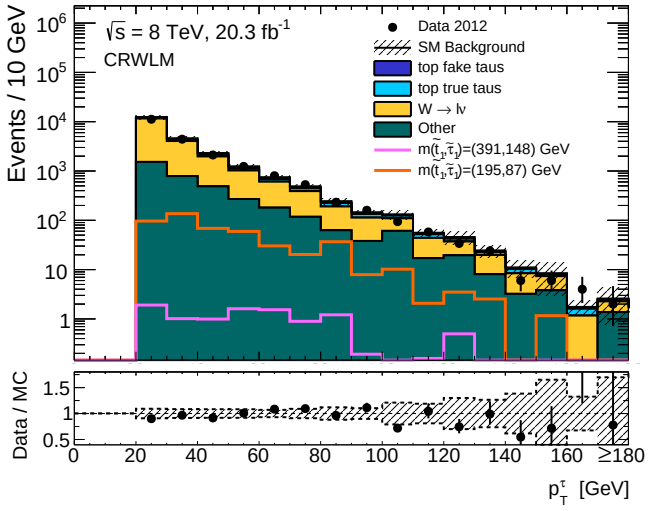

(a) p_{T} of τ_{had} - CRWLM

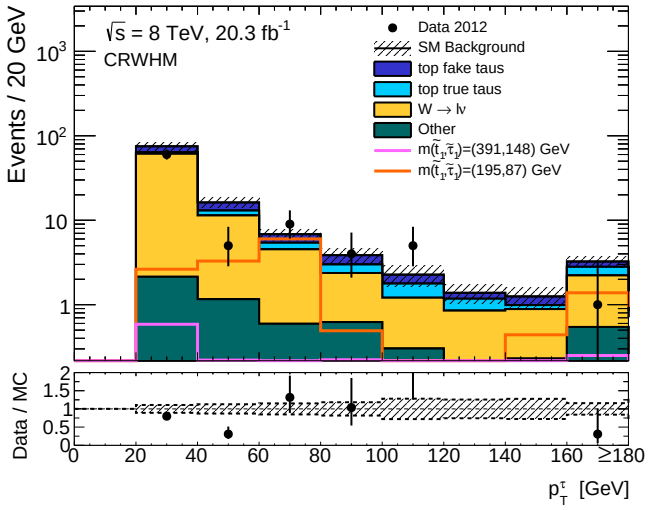

(b) p_{T} of τ_{had} - CRWHM

Figure 6.18: Distributions of the transverse momentum of the hadronically decaying tau for events passing the W+jets control region low-mass (Figure 6.18a) and high-mass (Figure 6.18b) selections after the momentum correction has been applied. The contributions from all SM backgrounds are shown as a histogram stack; the bands represent the total uncertainty. The distributions expected for the two signal optimisation points are also shown. The reweighted distributions agree with the data.

Table 6.4: Background fit results for the number of events in the three CRs and the VR in the lepton–hadron channel low-mass selection. Combined statistical and systematic uncertainties are given. The number of observed events and the total (constrained) background are the same by construction in the CRs. Entries marked with a dash indicate a negligible background contribution (< 0.1). The nominal expectations from MC simulation before the fit are given for comparison in the lower part of the table.

Channel	CRWLM	CRTtLM	CRTfLM	VRLM
Observed events	20929	77	198	386
Total (constrained) bkg events	20929.2 ± 144.7	77.0 ± 8.8	198.0 ± 14.0	350.6 ± 83.7
Top-quark events with true taus	782.8 ± 349.6	50.1 ± 16.5	83.3 ± 28.7	129.1 ± 50.0
Top-quark events with fake taus	1131.7 ± 477.9	24.6 ± 10.1	106.2 ± 35.9	206.4 ± 106.7
W+jets	15479.8 ± 640.5	1.7 ± 0.5	3.2 ± 2.3	6.7 ± 2.9
$Z/\gamma^* \to LL$	3268.1 ± 259.8	0.3 ± 0.2	4.7 ± 1.3	7.6 ± 2.4
$t\bar{t}V$	3.2	0.3	0.5	0.9
Diboson	263.5 ± 23.3	-	0.1	-
Expected bkg events before the fit	22281.7	98.1	234.7	408.6
Top-quark events with true taus	1101.6	70.6	117.2	181.6
Top-quark events with fake taus	1159.3	25.2	108.7	211.4
W+jets	16486.0	1.8	3.4	7.1
$Z/\gamma^* \to LL$	3268.1	0.3	4.7	7.6
$t\bar{t}V$	3.2	0.3	0.5	0.9
Diboson	263.5	-	0.1	-

likelihood function will be discussed in detail in Chapter 9. The numbers of observed events in the control regions constrain the fit. The likelihood function is composed of Poisson probability density functions for the event counts and Gaussian probability density functions for the systematic uncertainties. The Histfitter framework [144] is used to implement the fit and perform the statistical analyses of the results (see Chapter 8).

6.7 Validation

Tables 6.4 and 6.5 show the total expected and observed numbers of events in the lepton–hadron control and validation regions as well as a breakdown of the number of

Table 6.5: Background fit results for the number of events in the three CRs and the VR in the lepton–hadron channel high-mass selection. Combined statistical and systematic uncertainties are given. The number of observed events and the total (constrained) background are the same by construction in the CRs. Entries marked with a dash indicate a negligible background contribution (< 0.1). The nominal expectations from MC simulation before the fit are given for comparison in the lower part of the table.

Channel	CRWHM	CRTtHM	CRTfHM	VRHM
Observed events	101	39	45	17
Total (constrained) bkg events	101.0 ± 10.0	39.1 ± 6.2	45.0 ± 6.7	22.0 ± 5.0
Top-quark events with true taus	12.4 ± 3.5	36.1 ± 6.5	16.4 ± 3.7	8.8 ± 6.6
Top-quark events with fake taus	24.5 ± 10.5	1.9 ± 0.8	24.3 ± 8.7	10.47 ± 5.8
W+jets	56.3 ± 15.3	$0.1^{+0.2}_{-0.1}$	3.5 ± 2.5	1.9 ± 1.1
$Z/\gamma^* \to LL$	1.0 ± 1.0	-	-	0.5 ± 0.1
$t\bar{t}V$	0.3 ± 0.1	0.5 ± 0.2	0.4 ± 0.1	0.3 ± 0.1
Diboson	6.5 ± 0.4	0.5	0.4	0.1
Expected bkg events before the fit	131.7	32.8	41.6	20.5
Top-quark events with true taus	10.2	29.9	13.6	7.3
Top-quark events with fake taus	21.6	1.7	21.4	9.3
W+jets	92.1	0.2	5.8	3.2
$Z/\gamma^* \to LL$	1.0	-	-	0.5
$t\bar{t}V$	0.3	0.5	0.4	0.3
Diboson	6.5	0.5	0.4	0.1

expected events from each background process both before and after the background-only fit. Figures 6.19 and 6.20 show the N-1 distributions of $m_{\mathrm{T2}}\left(\mathrm{b}\ell, \mathrm{b}\tau_{\mathrm{had}}\right)$ and $m_{\mathrm{T2}}\left(\ell, \tau_{\mathrm{had}}\right)$ for the low-mass and high-mass validation regions respectively. The numbers of events in the validation regions are in good agreement with the Standard Model expectations. The observed number of events in the low-mass validation region is 386 (351 ± 84 expected), while the number of observed events in the high-mass validation region is 17 (22 ± 5 expected). The uncertainties quoted include both the statistical uncertainties and systematic uncertainties (see Chapter 7). The observed and expected numbers of events in the control regions are the same by design through the use of the background-only fit. Since the observed numbers of events and distribution shapes in the control regions and validation regions are consistent with the Standard Model expectations, there is confidence in the estimations of the backgrounds in the signal regions.

6.8 Same-sign method

The method used to estimate the large $t\bar{t}$ with fake hadronically decaying taus background in the signal region (see Sections 6.5.6 and 6.5.7) was determined to be the best of two methods considered. In the method described in the previous sections, the dominant backgrounds are estimated using Monte Carlo simulations but their overall scale is corrected to match data using scale factors determined in fits performed in control regions. As part of this method, the top-quark background is broken up into real and fake hadronically decaying taus and both are separately fitted to the data. The properties of the fake hadronically decaying taus are validated and also corrected to match the data if necessary (i.e. hadronically decaying tau p_{T} - see Section 6.5.7).

In an alternative method, the same-sign method, a similar set of cuts is defined but the light charged lepton is required to have an electric charge with the same sign as the hadronically decaying tau. The cross-section for processes like this is extremely small in the Standard Model and so it can be assumed that the vast majority of events measured in this way are due to another object (e.g. a jet) being incorrectly identified as a hadronically decaying tau candidate. A scale factor from a loose selection on data is used to extrapolate the number of opposite-sign charged leptons in the final state from the number of same-sign leptons in the final state. Too few same-sign events are observed in data for the SRHM selection to be able to make a meaningful background prediction for SRHM. The method could, however, have been used for

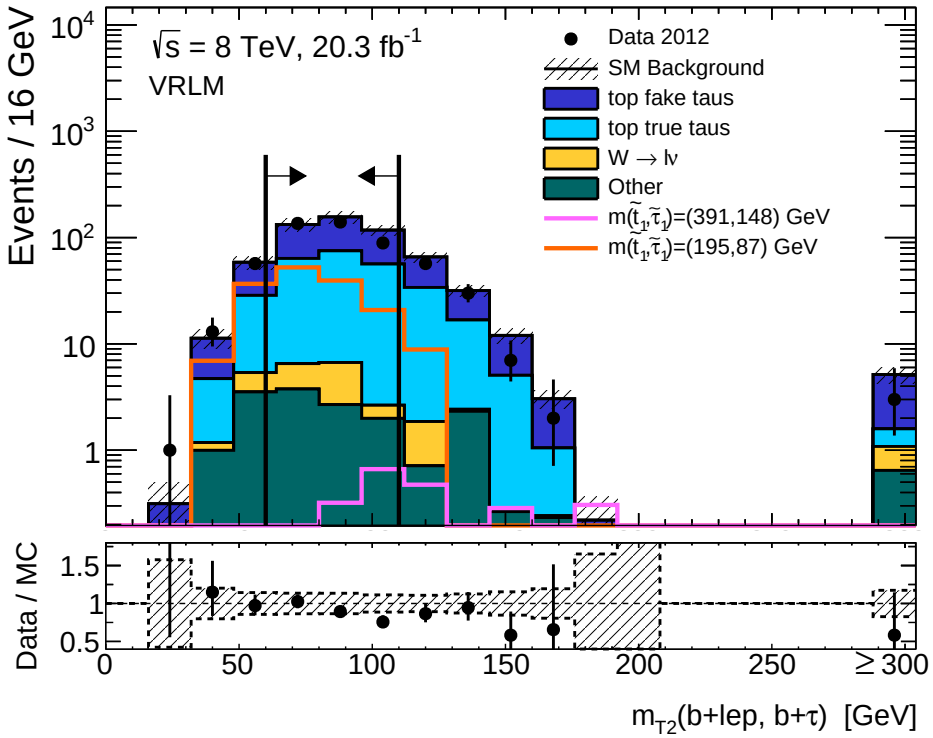

Figure 6.19: VRLM N-1: Distribution of $m_{\mathrm{T2}}\,(\mathrm{b}\ell, \mathrm{b}\tau_{\mathrm{had}})$ after the VRLM selection except for the cut on $m_{\mathrm{T2}}\,(\mathrm{b}\ell, \mathrm{b}\tau_{\mathrm{had}})$. This validation region differs from SRLM by the inversion of the $H_{\mathrm{T}}/m_{\mathrm{eff}}$ cut ($H_{\mathrm{T}}/m_{\mathrm{eff}} < 0.5$) and a cut of $60 < m_{\mathrm{T2}}\,(\mathrm{b}\ell, \mathrm{b}\tau_{\mathrm{had}}) < 110$ GeV. The contributions from all SM backgrounds are shown as a histogram stack; the bands represent the total uncertainty. The distributions expected for the two signal optimisation points are also shown. The lines and arrows show the cuts on the plotted variable that are required for the VRLM selection.

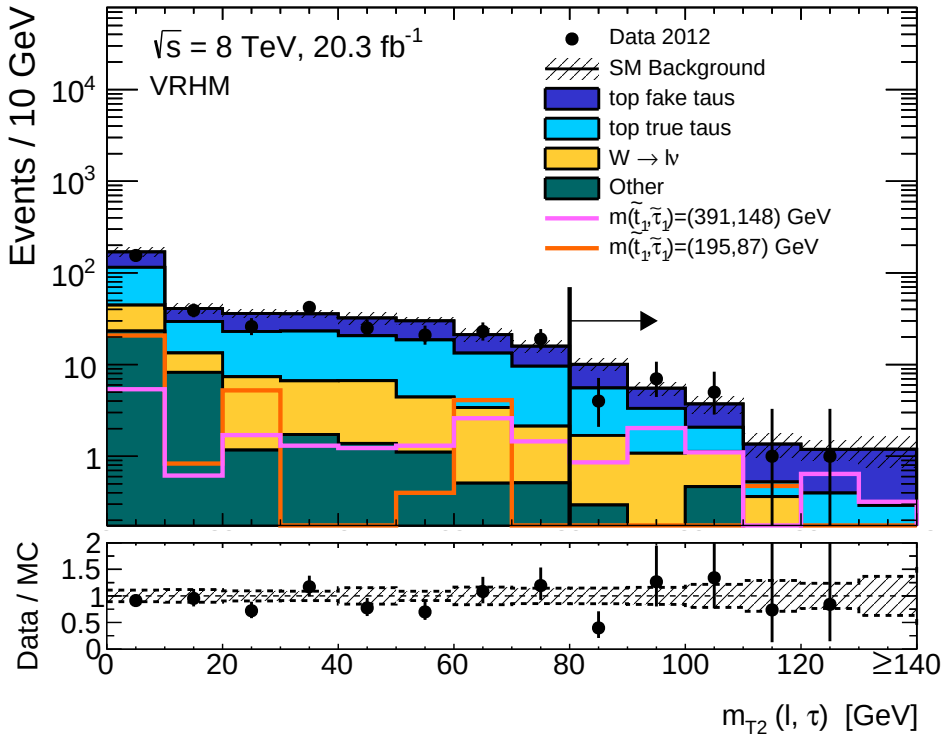

Figure 6.20: VRHM N-1: Distribution of $m_{\mathrm{T2}}(\ell, \tau_{\mathrm{had}})$ after the VRHM selection except for the cut on $m_{\mathrm{T2}}(\ell, \tau_{\mathrm{had}})$. This validation region differs from SRHM by the inversion of the $E_{\mathrm{T}}^{\mathrm{miss}}$ cut ($E_{\mathrm{T}}^{\mathrm{miss}} < 150$ GeV) and a looser cut of $m_{\mathrm{T2}}(\ell, \tau_{\mathrm{had}}) > 80$ GeV. The contributions from all SM backgrounds are shown as a histogram stack; the bands represent the total uncertainty. The distributions expected for the two signal optimisation points are also shown. The line and arrow show the cut on the plotted variable that is required for the VRHM selection.

the SRLM background estimation. The nominal method and the same-sign method for estimating the fake hadronically decaying tau background give consistent results.

6.9 Lepton-lepton and Hadron-hadron channels

The lepton–lepton and the hadron–hadron analyses probe complementary regions of the stop-stau mass plane. The lepton–lepton channel is composed of several signal regions that are made orthogonal to each other by use of the number of jets, the p_{T} of the jets, and $m_{\mathrm{T2}}(\ell,\ell)$. The hadron–hadron channel has just one signal region (SRHH) and is optimised for scalar tau masses as small as the LEP limit. It also uses the $m_{\mathrm{T2}}(\tau_{\mathrm{had}},\tau_{\mathrm{had}})$ variable in a similar way to how the lepton–hadron SRHM analysis uses $m_{\mathrm{T2}}\,(\ell,\tau_{\mathrm{had}})$. In general, the analyses use similar variables (e.g. m_{T2} and $E_{\mathrm{T}}^{\mathrm{miss}}$) to separate the dominant background processes from the signal. The hadron–hadron channel uses the *tight* working point for the τ_{had} identification, which differs from the "*medium*" working point used by the lepton–hadron channel (see Section 4.2.5). Like the SRHM selection, the SRHH selection requires at least two jets where at least one must be b-tagged. The hadron–hadron analysis and the lepton–lepton analysis were performed by fellow collaborators in the ATLAS Supersymmetry group and so the full details of these searches are beyond the scope of this dissertation. The lepton–lepton analysis is a re-interpretation [132] of an earlier search for direct pair production of scalar tops [133] and the hadron–hadron analysis is described in Reference [57].

Chapter 7

Systematic Uncertainties

The systematic uncertainties in this analysis are categorised as either experimental or theoretical. There are two main ways that particle physicists calculate systematic uncertainties. The first is to vary a quantity measured in an event by a known uncertainty. The effect on the analysis is determined by re-running the analysis programs with the positive and/or negative variation to the measured quantity to determine how the number of events in each of the regions changes. This method is typically used for the experimental uncertainties, for example the energy of the jets. Each variation may be applied directly (e.g. changing a jet energy E to $E \pm \Delta E$ or may be applied by changing an event-level scale factor (e.g. the b-tagging efficiencies). The variations are chosen to be one standard deviation in size assuming a Gaussian distribution. This method will be referred to as the quantity-variation method. The second method is to run one or two different simulated samples through the analysis to see how the results in the different regions differ from those obtained using the nominal sample. This method is typically used for estimating the systematic uncertainties relating to the physics theory, for example the choice of the MC generators. There are many ways in which simulations can differ from one another. They may involve different physics assumptions and approximations, different cut-off values for when certain processes and functions are executed, different methodologies, and different focuses and thus strengths and weaknesses. The difference between the event counts when running two different simulations is treated as a one standard deviation systematic uncertainty. This method will be referred to as the sample-variation method. All the experimental and theoretical uncertainties are propagated through the analysis selections to see how many events are added or removed from the signal regions. Finally, the effects of the individual uncertainties are combined to give a total uncertainty on the Standard

Model background estimate in each signal region.

Many of the larger experimental uncertainties are related to the measurement of the energy or momentum of an object. For a particular object, both the energy (or momentum) scale and the energy (or momentum) resolution have associated uncertainties. The energy scale and resolution are measured for jets, electrons, and hadronically decaying taus, and the momentum scale and resolution are measured for muons. The energy (or momentum) scale ensures that the energy (or momentum) distribution is correctly centred on the true value. An example of this is the jet energy scale (JES), which was introduced in Section 4.2.2. The energy (or momentum) resolution is the relative width of the distribution of the measurement of an object's energy (or momentum). The energy resolution is calculated as $\sigma(E)/E$ and the momentum resolution calculated as $\sigma(p_{\mathrm{T}})/p_{\mathrm{T}}$.

7.1 Individual uncertainties

The experimental systematic uncertainties considered include those calculated for the following:

- Jets: Jet reconstruction (see Section 4.2.2) requires cell weighting for the calorimeter response to hadrons as well as a calibration of the jet energy scale. The energy of a jet is also sensitive to pile-up as a function of the pile-up conditions and the jet area. The systematic uncertainties on the jet energy scale (JES) and the jet energy resolution (JER) are both significant. The jet energy scale uncertainty has a magnitude that depends on the event sample but typically amounts to $0.5-3\%$ [88] (see Section 7.2.2). The jet energy resolution and its uncertainty vary with energy. The jet energy resolution improves from roughly 30% for $p_{\mathrm{T}} = 20$ GeV jets to better than 10% for $p_{\mathrm{T}} = 100$ GeV jets, where 20 GeV is the lowest allowed jet p_{T} from the analysis preselections and 100 GeV is a typical value for the transverse momentum of the highest-p_{T} jet for the optimisation point $(m_{\tilde{t}_1}, m_{\tilde{\tau}_1}) = (391, 148)$ GeV. The jet energy resolution uncertainty is around 1% for jets of more than 100 GeV and less than 3% at 20 GeV [147]. The resolution uncertainty is relative to the fractional resolution, $\sigma(E)/E$, so for a $p_{\mathrm{T}} = 100$ GeV jet, the jet energy resolution uncertainty, using the numbers above, is roughly $100\ \mathrm{GeV} \times (10\% \times 1\%) \sim 0.1$ GeV. The effects of all these uncertainties on the expected number of Standard Model background

events are measured using the quantity-variation method.

- b-tagged jets: A systematic uncertainty is also used for the b-tagging efficiency. This uncertainty is associated with the scale factors used to make the b-tagging efficiency in simulation match that in data. The efficiencies are measured using $t\bar{t}$ events. Top theory uncertainties, the jet energy uncertainties, and additional smaller uncertainties are propagated through the b-tagging efficiency analysis resulting in different scale factors (see Section 5.2.1). These different scale factors are used to implement the variations in the efficiency. In this analysis, the scale factors have a total uncertainty of $\sim 2\%$ for jets with p_{T} around 100 GeV [90]. The effects of all these uncertainties on the expected number of Standard Model background events are measured using the quantity-variation method.

- Hadronically decaying taus: A hadronically decaying tau has a complex final state that can include several charged hadrons, neutral hadrons, and neutrinos. These final states can also be mimicked by electrons and jets. The only systematic uncertainty related to the reconstruction of a τ_{had} (see Section 4.2.5) explicitly considered in this analysis is the tau energy scale [96]. See Section 7.2.4 for more details. The total tau energy scale uncertainty for $E_{\mathrm{T}} > 20$ GeV and $|\eta| < 2.5$ is between 2% and 3% for a τ_{had} with one track and between 2% and 4% for a τ_{had} with more tracks, depending on E_{T} and $|\eta|$ [96]. The visible τ_{had} momentum resolution is about 20% for low-momentum (20 GeV) hadronically decaying taus and improves to about 5% as the momentum increases [96]. The resolution uncertainties were determined to be small by the ATLAS Tau Working Group and so the tau energy resolution uncertainties are not included in this analysis. The tau energy resolution uncertainties are generally smaller than the other uncertainties in this analysis.

- Electrons and muons: The systematic uncertainties related to the identification and reconstruction of electrons and muons (see Sections 4.2.3 and 4.2.4) are negligible in comparison to the other systematic uncertainties in this analysis. See Section 7.2.2 for more details.

  The electron energy scale uncertainty is smallest at $E_{\mathrm{T}} \sim 40$ GeV and $|\eta| < 1.37$ at 0.04% [92]. The electron energy scale uncertainty is smaller than 1% for a wide range of energies and η. The electron energy resolution is better than approximately 2.5% for electrons with $|\eta| \sim 0.2$ [92] and $E_{\mathrm{T}} \gtrsim 25$ GeV. The

resolution improves to approximately 1% for electrons of $E_{\mathrm{T}} \sim 200$ GeV for $|\eta| \sim 0.2$. The relative uncertainty on the electron energy resolution reaches a minimum of about 10% around $E_{\mathrm{T}} \sim 40$ GeV and increases to around 25% at $E_{\mathrm{T}} \sim 200$ GeV [92].

The muon momentum scale uncertainties are known to better than approximately 0.2% over the full pseudorapidity range of the detector [95]. The momentum resolution ranges from 1.7% for muons with small $|\eta|$ and for $p_{\mathrm{T}} \sim 10$ GeV, to 4% at large rapidity and $p_{\mathrm{T}} \sim 100$ GeV. The muon momentum resolution uncertainty is roughly 6% for muons with $p_{\mathrm{T}} \sim 100$ GeV and $|\eta| < 1.05$ (see top left plot of Figure 17 in Reference [148]).

- Missing transverse energy: The missing transverse energy is calculated using the reconstructed jets and charged leptons in the event (see Section 4.2.6) and so their systematic uncertainties propagate into the $E_{\mathrm{T}}^{\mathrm{miss}}$ calculation. The isolated tracks from pile-up and the isolated topoclusters corresponding to energy deposits created by pile-up and noise are also included in the missing transverse energy calculation [100]. The uncertainties related to the measurement of these isolated particles from pile-up are propagated into the missing transverse energy measurement as a systematic uncertainty. The total estimated uncertainty on the component of the missing transverse energy from these pile-up particles (not on the full $E_{\mathrm{T}}^{\mathrm{miss}}$) is about 2.6% [100]. In the 2010 data set where the LHC was running at a centre of mass energy of 7 TeV [100], the missing energy from just the isolated topoclusters reached a peak value for the year of less than 10 GeV. The effects of all these uncertainties on the expected number of Standard Model background events are measured using the quantity-variation method.

- Luminosity: The luminosity delivered by the LHC is determined using measurements of the amount of charge in each beam, the cross-sectional shapes of the beams, and the amount of overlap of the particle beams. All of these quantities have systematic uncertainties associated to them that are propagated into the total systematic uncertainty on the integrated luminosity. The systematic uncertainty on the luminosity delivered by the LHC is 2.8% using techniques similar to those defined in Reference [149]. One of the primary luminosity measurement procedures is the Van der Meer scan, where the two beams are separately shifted along the x-axis and along the y-axis to measure the profile of the beams. The effects of all these uncertainties on the expected number of Standard Model

background events are measured using the quantity-variation method.

- Pile-up: The simulated pile-up only matches the pile-up in data after reweighting events based on the number of inelastic proton–proton collisions and then scaling the numbers of events based on the number of primary vertices, as discussed in Sections 5.1 and 5.2.1. Luminosity uncertainties, detector acceptance uncertainties, and other uncertainties were propagated through the pile-up scaling studies to determine that there is a total uncertainty of $\sim \pm 4\%$ on the pile-up scaling. The effect of these uncertainties on the expected number of Standard Model background events is measured using the quantity-variation method.

- Hadronically decaying tau momentum reweighting: The momenta of the hadronically decaying taus in W+jets events are reweighted as discussed in Section 6.5.7. The reweighting scale factor is a function of the momentum of the hadronically decaying tau. The associated event weights should be independent of the light charged lepton being an electron or a muon, but nevertheless separate fits were performed for the electron and muon events. A systematic uncertainty is introduced to cover the difference between the two by calculating a third fit, which uses both the electron and muon events. There is a maximum deviation of $\sim 30\%$ between the scale factors from the individual fits and the scale factor from the combined fit, which occurs when the scale factors are small. The size of the effect of the hadronically decaying tau reweighting systematic uncertainty on the analysis is determined by determining the number of events in the signal regions when using only the third fit and comparing this to the number of events in the signal regions when using the two separte electron and muon fits. The effects of all these uncertainties on the expected number of Standard Model background events are measured using the quantity-variation method.

The theory systematic uncertainties considered include those on the following:

- Top events: The dominant $t\bar{t}$ systematic uncertainties are related to the choice of generator, the choice of the parton showering tool, and the amount of initial state and final state radiation. The tools used to estimate the theory systematic uncertainties are summarised in Table 5.2. The nominal generator and parton showering tool for $t\bar{t}$ are `POWHEG-BOX` + `PYTHIA` as shown in Table 5.1. The generator systematic uncertainty is measured by comparing the predictions of

POWHEG-BOX to the predictions of MC@NLO-4.06. The parton showering systematic is estimated by comparing the nominal results from POWHEG-BOX + PYTHIA with the results when POWHEG-BOX is interfaced to Jimmy + HERWIG. The parton showering is done by HERWIG while Jimmy is used for the additional parton interactions. The systematic uncertainty related to the initial-state and final-state radiation is estimated by ACERMC-3.8 run with different tunings. More details about the ATLAS modelling of top-quark events is given in Reference [150].

Single top events and $t\bar{t}$ events are simulated separately but there is no uniquely defined way to separate single top events in the Wtb channel from $t\bar{t}$ events, as the two have the same final state. A systematic uncertainty is assigned to cover how different methods define the separation [151, 152]. This affects the analysis because the $t\bar{t}$ simulated samples are separate from the W+jets simulated samples. When changing how the separation is defined, only one sample is affected and the overall number of events entering the selection regions changes.

The effects of all these uncertainties on the expected number of Standard Model background events are measured using the sample-variation method.

- W+jets events: The simulation of the parton showering in W+jets has associated systematic uncertainties. Unlike the procedure used for the $t\bar{t}$ parton showering uncertainty, the W+jets parton showering variations are introduced without changing the parton showering tool (see Table 5.1). It was not feasible to run the large W+jets sample with a different parton showering tool. Instead, the nominal sample events were reweighted based on the number of truth jets. The scale factors used to perform the reweighting were derived by and for the analysis described in References [153, 154]. Separate W+jets samples were generated using ALPGEN, one nominal sample and two systematic samples where parton showering scale variations were introduced. The reweighting scale factors are derived from the ALPGEN samples.

  There is also a systematic uncertainty related to the relative production cross-sections of W+jets events that also contain b-jets [155]. The relative uncertainties on the number of Wbb+jets events were calculated by introducing variations in the generator parameters.

  The effects of all these uncertainties on the expected number of Standard Model background events are measured using the sample-variation method.

- Cross-sections and normalisations: The production cross-sections of the various processes are calculated at finite orders in α_{EW} and α_S (see Table 5.1). For the dominant background process ($t\bar{t}$) the theoretical uncertainty on the production cross-section due to higher order corrections that haven't been calculated is about 3% [111]. The signal samples have systematic uncertainties on the production cross-sections that vary between 14% and 16% for scalar top masses between 150 and 560 GeV.

  The dominant backgrounds are normalised to data in a combined fit. The normalisation scale factors each carry an uncertainty derived from the fit.

  The effects of all these uncertainties on the expected number of Standard Model background events are measured using the quantity-variation method.

7.2 Uncertainties comparison

The total estimated backgrounds in the signal regions along with their associated statistical and systematic uncertainties are shown in Table 7.1. Many of the systematic uncertainties have been grouped together either because they are small or because they are strongly correlated with one another. The individual uncertainties are compared later in this section.

The size of the systematic uncertainties can be different in each channel and signal region. For example the total overall effect from the systematic uncertainties related to the hadronically decaying taus is different in the three channels because the total number of hadronically decaying taus is different in each channel and the τ_{had} working points are different too (see Section 6.9). This is discussed more in Section 7.2.4. The systematic uncertainties in the lepton–lepton channel will not be presented because the lepton–lepton channel is a re-interpretation of a previous analysis.

7.2.1 Introductory overview of the uncertainties

Two of the dominant systematic uncertainties in the lepton–hadron channel are the top-quark theory uncertainties and the uncertainties on the normalisation of the true-τ_{had} and fake-τ_{had} top-quark backgrounds. The jet energy scale and resolution, and the tau energy scale are the dominant detector-related systematic uncertainties for the lepton–hadron channel.

Table 7.1: Summary of background estimates and the associated total uncertainties. The size of each systematic uncertainty is quoted as a relative uncertainty on the total background. A dash indicates a negligible contribution to the uncertainty ($< 1\%$). The individual uncertainties can be correlated, and thus do not necessarily sum in quadrature to the total relative uncertainty. See Reference [133] for a breakdown of the uncertainties in the lepton–lepton channel.

	SRHH	SRLM	SRHM
Background events	3.1 ± 1.2	22.1 ± 4.7	2.1 ± 1.5
Uncertainty Breakdown [%]:			
Jet energy scale and resolution	17	13	2
Tau energy scale	9	4	3
Isolated topocluster energy scale and resolution	1	2	4
b-tagging	2	4	2
Top-quark theory uncertainty	37	11	64
W+jets theory and normalisation	-	1	19
Simulation statistics	20	6	21
Top normalisation	18	6	20

7.2.2 Jet, electron, and muon energy and momentum uncertainties

Energy and momentum resolutions

The energies of jets are measured in a fundamentally different way from the momenta of muons. The calorimeters measure the amount of deposited energy and so the higher the energy of the jet, the higher the energy deposited. As a result, the energy resolution of jets improves as the energy of the jet increases. Measurements of the momenta of muons rely on measurements of the curvature of their associated tracks. The amount of curvature of a track decreases as the momentum of the muon increases. In this analysis the muons have small momenta and so they have relatively small momentum resolutions. The jets in this analysis have small energies and so they have relatively large energy resolutions. The momentum resolution of the muons in this analysis should typically be better than the energy resolutions of the jets.

The energies of electrons are measured with the calorimeters and so the electron energy resolution decreases as the energy of the electron increases. The energy resolution of electrons is better than the energy resolution of jets because the electrons do not have nuclear interactions that complicate the energy measurements. Overall,

the electrons in this analysis should typically have smaller energy resolutions than the jets in this analysis.

Energy and momentum uncertainties comparison

In general the energy measurement of hadronic objects has larger uncertainties than the energy measurement of electrons and the momentum measurement of muons largely because jets lose energy through nuclear reactions while the light charged leptons do not. The energy and momentum uncertainties of the light charged leptons are actually folded into the energy uncertainties of the jets because some of the jet calibrations are based on events where they recoil against electrons or muons (e.g. $Z\,[\rightarrow \ell\ell] + \text{jets}$). This is done in part because the Z boson has a very well known mass and a narrow resonance width.

The momentum and energy scale and resolution uncertainties are typically smaller for electrons and muons than for jets. In this analysis, the electron and muon energy and momentum scale and resolution uncertainties are small enough ($< 1\%$) that their effects on the signal region counts were not worth including in Table 7.1. The energy scale and resolution uncertainties of the jets are relatively large compared to those of the charged leptons. Since the selections require at least two jets, the jet energy scale and resolution uncertainties from the individual jets can compound to create a larger uncertainty on the analysis selections, but this is not always the case. Compared to the other detector related uncertainties affecting the low-mass analysis, the jet energy resolution and scale uncertainties produce a relatively large uncertainty on the number of events entering SRLM. In SRHM, however, these jet uncertainties ended up producing a small uncertainty on the total event count because the numbers of events added and removed from SRHM largely cancel each other out.

7.2.3 *b*-tagging

The b-tagging uncertainty variations are applied by changing the b-tagging efficiency scale factors. The b-tagging efficiency scale factors are event-level weights to correct the b-tagging efficiencies in Monte Carlo to match the data, as discussed in Section 7.1. Each b-tagged jet has its own efficiency scale factor so the larger the number of b-tagged jets, the larger the number of event-level weights that get multiplied together. With everything else being equal, it then follows that the more b-tagged jets in an event, the larger the systematic uncertainty from b-tagging in the event.

The SRLM selection requires a minimum of two b-tagged jets but the SRHM selection and the hadron–hadron selection require only a minimum of one b-tagged jet. As a result, the b-tagging systematic uncertainty has a larger effect on the number of events passing the SRLM selection than it does on the number of events passing the SRHM selection.

7.2.4 Hadronically decaying taus

The size of the effect of the tau energy scale systematic uncertainty on a signal region is partly dependent on the number of hadronically decaying taus in the selection. The hadron–hadron selection requires two hadronically decaying taus compared to the single τ_{had} in the lepton–hadron selection and so the effect of the tau energy scale uncertainty on the number of events expected in a signal region should be larger for the hadron–hadron selection if everything else were equal. The size of the hadronically decaying tau energy uncertainties in the different signal regions is partly complicated by the τ_{had} identification working point. The hadron–hadron channel uses the *tight* working point whereas the lepton–hadron selections use the *medium* working point.

Reconstructed hadronically decaying taus are seeded from jet candidates as both are composed of hadron(s). As a result, an individual τ_{had} in this analysis could be expected to have an energy scale uncertainty similar in size to that of a jet but worse than that of an electron or muon. Of course, the energy of a τ_{had} is calibrated separately from the energy of a jet so the two should not be identical. The energy resolution uncertainty of hadronically decaying taus was found to be small and is not included.

7.2.5 Isolated particles for the missing energy calculation

The isolated topoclusters and tracks from pile-up are from relatively low-energy particles. A single low-energy particle should not have much of an effect on the missing energy calculation but an event can have many low-energy particles that can occasionally align to have a sizable effect. The isolated topoclusters have relatively large energy uncertainties and so in this analysis a small but potentially non-negligible systematic variation may be expected.

7.2.6 Top-quark and W+jets theory

The largest theory uncertainties are those relating to the simulation of the top-quark events. The $t\bar{t}$ background is the largest background by nearly an order of magnitude and so its uncertainties have a larger effect on the signal region background estimate than the sub-dominant W+jets theory uncertainties.

The top theory uncertainties are among the largest systematic uncertainties because of the large number of different event properties that are affected. Changes to the parton showering, and the initial state and final state radiation affect the properties of jets, the properties of hadronically decaying taus, and the number of jets simulated per event. All of this can affect the missing transverse energy measurement and the derived variables e.g. $m_{\mathrm{T2}}\left(\mathrm{b}\ell, \mathrm{b}\tau_{\mathrm{had}}\right)$.

The SRLM selection was designed to target scalar top masses that are similar to or smaller than the top quark mass. It also targets scalar tau masses that are only a little larger than the W boson mass. As such, the low-mass lepton–hadron analysis focuses on a region of the stop-stau mass plane that kinematically is a lot more similar to the dominant $t\bar{t}$ background compared to the very heavy scalar top and scalar tau masses that SRHM targets. The $t\bar{t}$ generators are designed to accurately simulate events in the region of phase space around the top quark mass scale and so the simulated $t\bar{t}$ events entering SRLM are more likely to be better simulated than those entering SRHM. As such, changing $t\bar{t}$ generators should have a larger effect on the high-mass analysis than the low-mass analysis. Since the hadron–hadron channel is designed to be sensitive to lower scalar tau masses, the size of the effects of changing the $t\bar{t}$ generators on SRHH should be between that of the low-mass and high-mass lepton–hadron analyses.

7.2.7 Background-only fits

The uncertainties on the background-only fits are connected to the statistical uncertainties on the numbers of events in the analysis regions. The SRLM selection has a smaller top background normalisation uncertainty than the SRHM selection partly because the low-mass control regions contain a much larger number of observed events than the high-mass control regions. The larger the number of observed events in a control region, the smaller the uncertainty on the normalisation parameter. The W+jets background normalisation uncertainties should be smaller than the top background normalisation uncertainties because the number of observed events in the W+jets

control regions is larger than the number of observed events in the top control regions. The W+jets normalisation uncertainties in this analysis are very small and so were combined with the W+jets theory uncertainties in Table 7.1. The purity of the control regions can also affect the normalisation uncertainties. The b-tagged jet vetos help to give the W+jets control regions relatively good purity. The top control regions do not always separate true from fake hadronically decaying taus very well and so the top background normalisation uncertainties are larger than the W+jets background normalisation uncertainties.

Chapter 8

Results

In this chapter the results from unblinding the lepton–hadron signal regions will be presented. The results from the lepton–lepton and hadron–hadron analyses will also be discussed. In all of the plots and tables the hadronically decaying tau p_{T} reweightings and scale factors from the background-only fits (see Section 6.3 and Chapter 9) have been applied unless specified otherwise.

8.1 Lepton-hadron channel

The numbers of expected and observed events in the various lepton–hadron low-mass and high-mass regions are summarised in Figures 8.1 and 8.2 respectively. The expected and observed numbers of events in the two lepton–hadron signal regions are given in Table 8.1 along with a breakdown of the expected numbers of events from the various background processes both before and after the background-only fit. In the low-mass signal region the observed number of events is 20 while the Standard Model expectation is 22 ± 4.7. In the high-mass signal region the observed number of events is 3 while the Standard Model expectation is 2.1 ± 1.5. The uncertainties quoted include both the statistical uncertainties and systematic uncertainties. Good agreement is seen between the observed and expected number of events in both the low-mass and high-mass signal regions; the observed number of events lies within the uncertainty ranges quoted for the expected background.

In this chapter, all the figures for the lepton–hadron analysis have the two optimisation points overlayed: the pink curve corresponds to the SRHM optimisation point and the orange curve corresponds to the SRLM optimisation point. Figure 8.3 shows

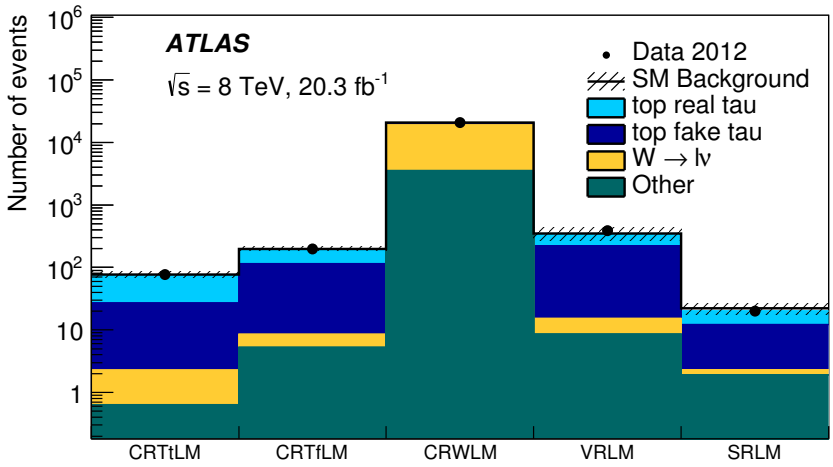

Figure 8.1: Background yields and composition after applying the background-only fit scale factors to the three CRs, the VR, and the SR in the lepton–hadron channel low-mass selection. Combined statistical and systematic uncertainties are shown as shaded bands. The observed number of events and the total (constrained) background are the same by construction in the CRs.

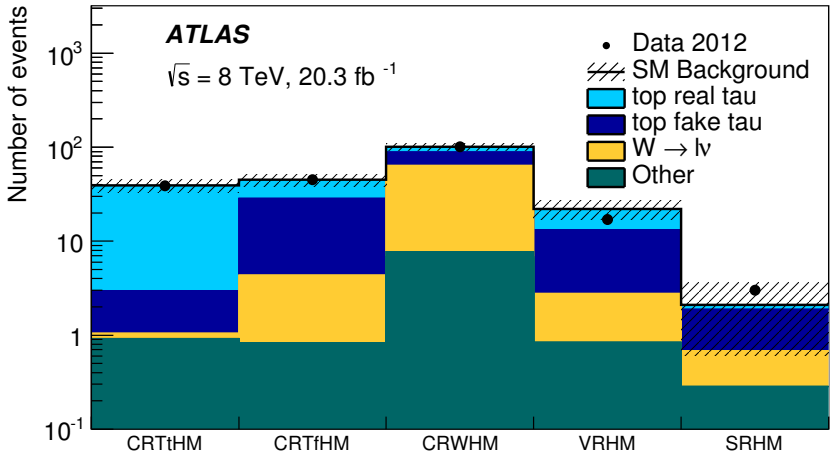

Figure 8.2: Background yields and composition after applying the background-only fit scale factors to the three CRs, the VR, and the SR in the lepton–hadron channel high-mass selection. Combined statistical and systematic uncertainties are shown as shaded bands. The observed number of events and the total (constrained) background are the same by construction in the CRs.

Table 8.1: Observed number of events and background fit results for the hadron–hadron SR and the two lepton–hadron SRs. Combined statistical and systematic uncertainties are given. The uncertainties can be correlated between the different background components so they do not necessarily sum to the total background uncertainty. A dash indicates a negligible background contribution, typically where no simulated events in the available samples pass the selection cuts. The nominal expectations from MC simulation are given for comparison in the lower part of the table.

Channel	SRHH	SRLM	SRHM
Observed events	3	20	3
Total (constrained) background events	3.1 ± 1.2	22.1 ± 4.7	2.1 ± 1.5
Top with only true tau(s)	2.0 ± 1.1	8.2 ± 3.9	$0.2^{+0.3}_{-0.2}$
Top with at least one fake tau	0.9 ± 0.5	9.8 ± 4.5	$1.2^{+1.4}_{-1.2}$
W+jets	$0.01^{+0.02}_{-0.01}$	2.2 ± 0.6	0.4 ± 0.4
Z/γ^*+jets	$0.04\ ^{+0.15}_{-0.04}$	1.9 ± 1.1	–
$t\bar{t} + V$	0.04 ± 0.02	–	0.3 ± 0.1
Diboson	0.14 ± 0.02	–	–
Expected background events before the fit	3.7	25.8	2.2
Top with only true tau(s)	2.0	11.5	0.18
Top with at least one fake tau	1.4	10.1	1.1
W+jets	0.01	2.4	0.65
Z/γ^*+jets	0.04	1.9	–
$t\bar{t} + V$	0.04	–	0.27
Diboson	0.14	–	–

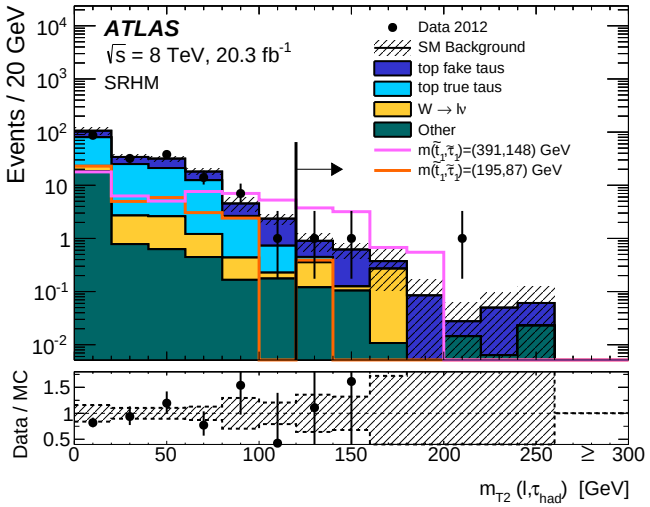

Figure 8.3: SRHM N-1: Distribution of $m_{\mathrm{T2}}(\ell, \tau_{\mathrm{had}})$ for events passing all the lepton–hadron HM signal region requirements, except that on $m_{\mathrm{T2}}(\ell, \tau_{\mathrm{had}})$. The contributions from all SM backgrounds are shown as a histogram stack; the bands represent the total uncertainty. The background yields have been rescaled by the post-fit normalisation factors. The distributions expected for two signal models are also shown. The line and arrow show the cut on the plotted variable that is required for the SRHM selection. This figure was taken from Reference [57].

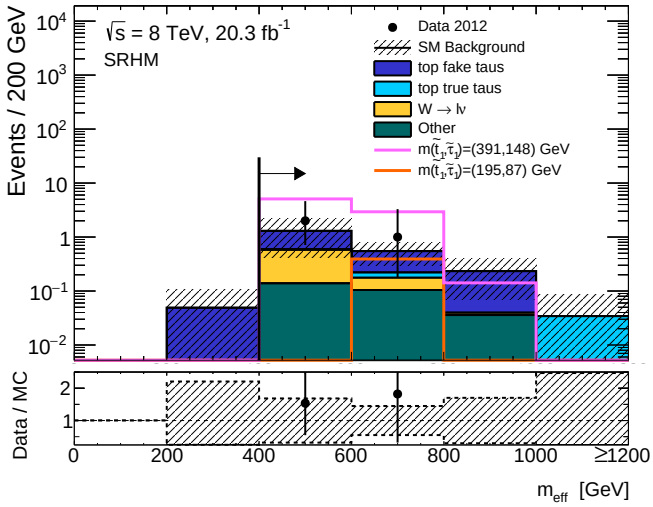

Figure 8.4: SRHM N-1: Distribution of m_{eff} for events passing all the lepton–hadron HM signal region requirements, except that on m_{eff}. The contributions from all SM backgrounds are shown as a histogram stack; the bands represent the total uncertainty. The background yields have been rescaled by the post-fit normalisation factors. The distributions expected for two signal models are also shown. The line and arrow show the cut on the plotted variable that is required for the SRHM selection.

the N-1 distribution for $m_{\mathrm{T2}}(\ell, \tau_{\mathrm{had}})$ for the events entering the high-mass signal region. Figures 8.4 and 8.5 show N-1 distributions for m_{eff} and $E_{\mathrm{T}}^{\mathrm{miss}}$ respectively for events entering SRHM. Good agreement is seen between the observed data and the Standard Model expectations in all the SRHM N-1 plots.

Figures 8.6 and 8.7 show N-1 distributions for $H_{\mathrm{T}}/m_{\mathrm{eff}}$ and $\left(p_{\mathrm{T}}^{\ell} + p_{\mathrm{T}}^{\tau_{\mathrm{had}}}\right)/m_{\mathrm{eff}}$ for the events entering the low-mass signal region. Figure 8.8 shows an N-1 distribution for $m_{\mathrm{T2}}(\mathrm{b}\ell, \mathrm{b}\tau_{\mathrm{had}})$ for events entering SRLM. There is good agreement between the observed data and the Standard Model expectations in nearly all the SRLM N-1 plots.

There are however, a couple of variable distributions at the preselection level and at the signal region N-1 level where there are deviations to note. In Figure 6.12, the deviation of the data from the Standard Model expectations in the region of $100 < m_{\mathrm{eff}} < 200$ GeV is known to be the result of mismodelling of events containing fake hadronically decaying taus. The overall number of events expected from the Standard Model in SRLM is the same as when using the same-sign method (see Section 6.8) to model events containing a fake hadronically decaying tau. The mismodelling of m_{eff} at low values is not vital to the low-mass analysis as m_{eff} is only explicitly used in CRWLM where the selection cut is relatively loose ($m_{\mathrm{eff}} < 400$ GeV). Only a subset of events in SRLM would be affected by the mismodelling. These values do not enter into the high-mass analysis as $m_{\mathrm{eff}} > 400$ GeV for all the high-mass control regions, VRHM, and SRHM.

In Figures 6.9 and 8.8, the deviation of the data from the Standard Model expectations in the region of $20 < m_{\mathrm{T2}}(\mathrm{b}\ell, \mathrm{b}\tau_{\mathrm{had}}) < 40$ GeV is known to be the result of mismodelling of events containing fake hadronically decaying taus. This is only a subset of SRLM, which is partly defined by the cut $m_{\mathrm{T2}}(\mathrm{b}\ell, \mathrm{b}\tau_{\mathrm{had}}) < 60$ GeV. The overall number of events expected from the Standard Model in SRLM is the same as when using the same-sign method to model events containing a fake hadronically decaying tau. This mismodelling does not affect the high-mass analysis because $m_{\mathrm{T2}}(\mathrm{b}\ell, \mathrm{b}\tau_{\mathrm{had}}) > 180$ GeV for all the high-mass control regions, VRHM, and SRHM.

Even if there is some mismodelling of some distributions within SRLM, there is still confidence that the total number of events expected from the Standard Model backgrounds in the signal region is sufficiently well modelled because the overall number of events in SRLM when using the nominal method to model the fake hadronically decaying tau contribution is the same as when using the same-sign method.

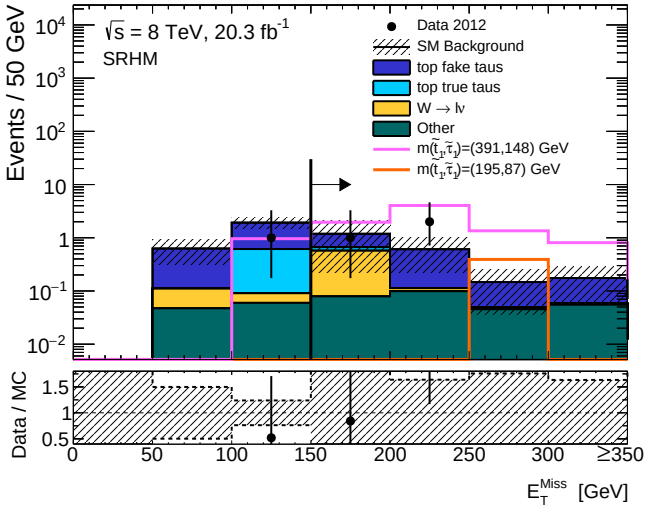

Figure 8.5: SRHM N-1: Distribution of $E_{\mathrm{T}}^{\mathrm{miss}}$ for events passing all the lepton–hadron HM signal region requirements, except that on $E_{\mathrm{T}}^{\mathrm{miss}}$. The contributions from all SM backgrounds are shown as a histogram stack; the bands represent the total uncertainty. The background yields have been rescaled by the post-fit normalisation factors. The distributions expected for two signal models are also shown. The line and arrow show the cut on the plotted variable that is required for the SRHM selection.

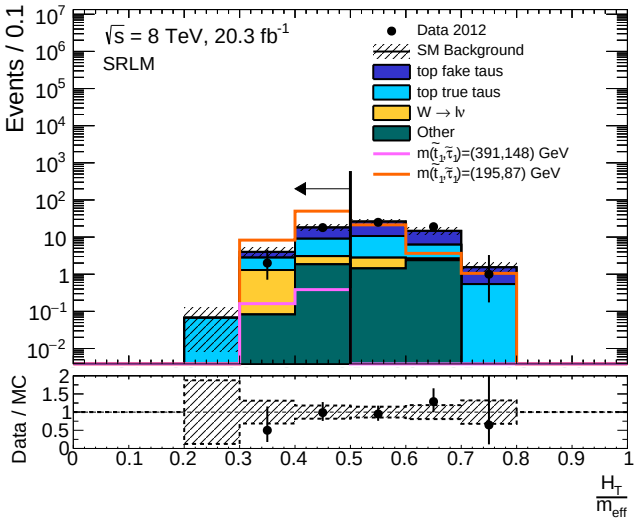

Figure 8.6: SRLM N-1: Distribution of $H_{\mathrm{T}}/m_{\mathrm{eff}}$ for events passing all the lepton–hadron HM signal region requirements, except that on $H_{\mathrm{T}}/m_{\mathrm{eff}}$. The contributions from all SM backgrounds are shown as a histogram stack; the bands represent the total uncertainty. The background yields have been rescaled by the post-fit normalisation factors. The distributions expected for two signal models are also shown. The line and arrow show the cut on the plotted variable that is required for the SRLM selection.

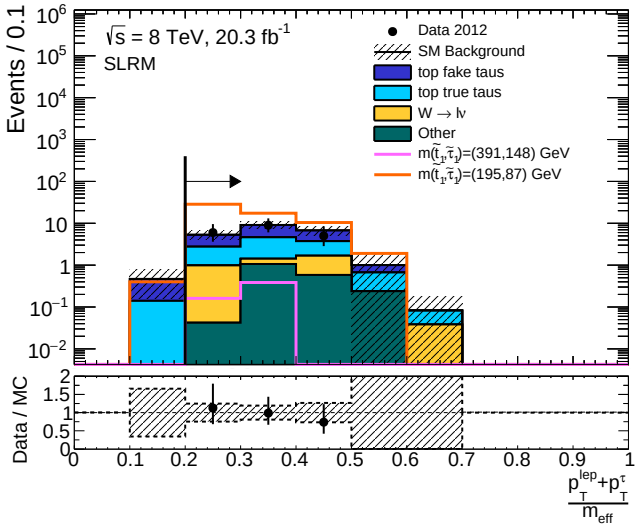

Figure 8.7: SRLM N-1: Distribution of $(p_{\mathrm{T}}^{\ell} + p_{\mathrm{T}}^{\tau_{\mathrm{had}}})/m_{\mathrm{eff}}$ for events passing all the lepton–hadron HM signal region requirements, except that on $(p_{\mathrm{T}}^{\ell} + p_{\mathrm{T}}^{\tau_{\mathrm{had}}})/m_{\mathrm{eff}}$. The contributions from all SM backgrounds are shown as a histogram stack; the bands represent the total uncertainty. The background yields have been rescaled by the post-fit normalisation factors. The distributions expected for two signal models are also shown. The line and arrow show the cut on the plotted variable that is required for the SRLM selection.

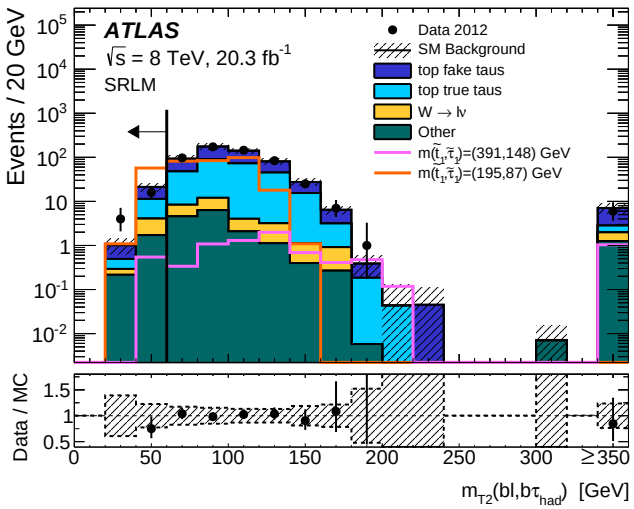

Figure 8.8: SRLM N-1: Distribution of $m_{\mathrm{T2}}\,(\mathrm{b}\ell, \mathrm{b}\tau_{\mathrm{had}})$ for events passing all the lepton–hadron LM signal region requirements, except that on $m_{\mathrm{T2}}\,(\mathrm{b}\ell, \mathrm{b}\tau_{\mathrm{had}})$. The contributions from all SM backgrounds are shown as a histogram stack; the bands represent the total uncertainty. The background yields have been rescaled by the post-fit normalisation factors. The overflow bin in the $m_{\mathrm{T2}}\,(\mathrm{b}\ell, \mathrm{b}\tau_{\mathrm{had}})$ plot is filled with the events that have for both pairings of $m(b\ell)$ and $m(b\tau_{\mathrm{had}})$ at least one invariant mass larger than m_t. The distributions expected for two signal models are also shown. The line and arrow show the cut on the plotted variable that is required for the SRLM selection. This figure was taken from Reference [57].

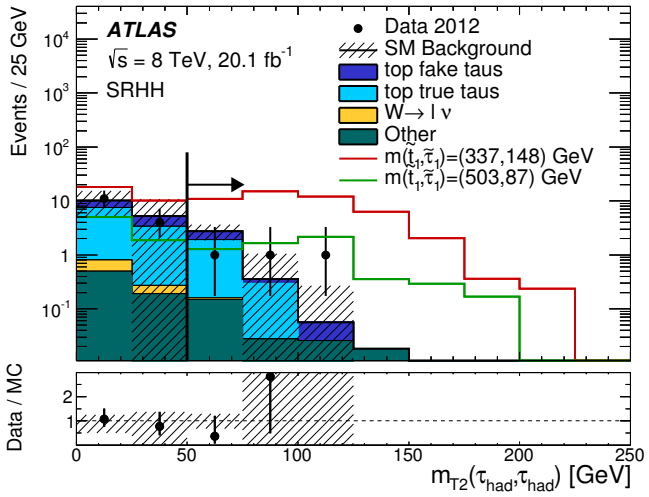

Figure 8.9: SRHH N-1: Distribution of $m_{\mathrm{T2}}(\tau_{\mathrm{had}}, \tau_{\mathrm{had}})$ for events passing all the hadron–hadron signal region requirements, except that on $m_{\mathrm{T2}}(\tau_{\mathrm{had}}, \tau_{\mathrm{had}})$. The contributions from all SM backgrounds are shown as a histogram stack; the bands represent the total uncertainty. The background yields have been rescaled by the post-fit normalisation factors. The distributions expected for two signal models are also shown. This figure was taken from Reference [57]. The line and arrow show the cut on the plotted variable that is required for the hadron–hadron selection.

8.2 Lepton-lepton and hadron-hadron channels

The number of events in the hadron–hadron signal region is given in Table 8.1. For both the lepton–lepton and the hadron–hadron analyses, the numbers of observed events in the signal regions are consistent with the Standard Model expectations. Figure 8.9 shows an N-1 distribution for $m_{\mathrm{T2}}(\tau_{\mathrm{had}}, \tau_{\mathrm{had}})$ for events entering the hadron–hadron signal region. The hadron–hadron channel focuses on the light scalar tau region of the stop-stau mass plane with a cut of $m_{\mathrm{T2}}(\tau_{\mathrm{had}}, \tau_{\mathrm{had}}) > 50$ GeV, which is looser than the lepton–hadron SRHM cut of $m_{\mathrm{T2}}(\ell, \tau_{\mathrm{had}}) > 120$ GeV (see Figure 8.3). The observed data match the Standard Model expectations over the full $m_{\mathrm{T2}}(\tau_{\mathrm{had}}, \tau_{\mathrm{had}})$ distribution. No numbers from the lepton–lepton analysis will be shown here because there are a large number of signal regions and the lepton–lepton analysis is a re-interpretation of the results of a different scalar top search [133, 132].

Chapter 9

Statistical methods and interpretation

This chapter discusses the statistical procedures used to perform the analysis and then interpret the results. The details of the likelihood function used to perform the background-only fit (introduced in Chapter 6) and the exclusion limits will be defined. The procedures used to set exclusion limits on the signal process will then be defined and applied to this analysis to exclude regions of the stop-stau mass plane at the 95% confidence level. The exclusions are calculated using the `HistFitter` program [144], which uses the software packages `HistFactory` [156] and `RooStats` [157]. In this chapter, the equations used for the statistical procedures will be presented first and then the variables used in those equations will be defined.

9.1 Statistical procedure

9.1.1 Likelihood function

The likelihood function gives a relative probability of obtaining a particular result. It is generally composed of probability distribution functions. The maximum value of the likelihood is achieved with the set of parameters that estimate the true underlying values for a given set of observations and under a given set of assumptions. These parameters are called maximum-likelihood estimators [158].

The likelihood function used in this analysis is defined in Equation 9.2. There are two main pieces to the likelihood function: one piece that includes the number of events in each control region and signal region from all the background processes

and the signal process ($P_{\text{CR,SR}}$), and another piece to constrain the nuisance parameters, which are typically associated with systematic uncertainties ($C_{\text{syst.}}$). Probability density functions can also be included for other parameters of interest such as the background normalisation scale factors.

$$L\left(\boldsymbol{\mu}, \boldsymbol{\theta}\right) = P_{\text{CR,SR}} C_{\text{syst.}} \tag{9.1}$$

$$= \prod_{r}^{\text{SR, CRs}} \text{Poisson}\left(N_r^{\text{obs}} | N_r^{\text{exp}}\left(\boldsymbol{\mu}\right)\right) \prod_{s}^{\text{systematics}} g\left(\theta_s\right), \tag{9.2}$$

On the left hand side of Equation 9.2 the vector $\boldsymbol{\mu}$ contains all the scale factors for the background processes and the signal process. Every systematic uncertainty, s, is described by a nuisance parameter, θ_s, which parametrises the systematic uncertainty. The vector $\boldsymbol{\theta}$ is the set of all the nuisance paramters.

The $P_{\text{CR,SR}}$ factor is made up of Poisson distributions for the control regions and the signal region. Each Poisson distribution is a function of the observed and expected number of events in the region. Expanding $P_{\text{CR,SR}}$ to show these separately gives:

$$P_{\text{CR,SR}} = \prod_{r}^{\text{SR, CRs}} \text{Poisson}\left(N_r^{\text{obs}} | N_r^{\text{exp}}\left(\boldsymbol{\mu}\right)\right) \tag{9.3}$$

$$= \text{Poisson}\left(N_{\text{SR}}^{\text{obs}} | N_{\text{SR}}^{\text{exp}}\left(\boldsymbol{\mu}\right)\right) \prod_{r}^{\text{CRs}} \text{Poisson}\left(N_r^{\text{obs}} | N_r^{\text{exp}}\left(\boldsymbol{\mu}\right)\right) \tag{9.4}$$

The expected and observed number of events in region r are represented by N_r^{exp} and N_r^{obs} respectively. Each is a sum over all the processes that contribute towards the total number of events and includes scale factors to correct some of the cross-sections (see Chapter 6). To simplify the notation, every process is assigned a scale factor, but that scale factor can be set to one. The expected number of events can be expanded as

$$N_r^{\text{exp}}\left(\boldsymbol{\mu}\right) = \sum_{p}^{\text{b+s processes}} \mu_p N_{r,p}^{\text{exp}} \tag{9.5}$$

where $N_{r,p}^{\text{exp}}$ is the expected number of events in region r by process p and μ_p is the background normalisation scale factor for process p. Note that the summation is over

all the background processes as well as the signal process. The background-only fit determines the values of μ_p for $t\bar{t}$ with a true τ_{had}, $t\bar{t}$ with a fake τ_{had}, and the W+jets processes. For each of the other background processes, the number of expected events is directly taken from simulation so $\mu_{\text{p}} = 1$. For a signal with the nominal cross-section, $\mu \equiv \mu_{\text{signal}} = 1$. This analysis only searches for signals that add events to the Standard Model background so $\mu \geq 0$. Expanding Equation 9.5 to show all the normalisation parameters gives:

$$\begin{aligned} N_r^{\text{exp}}(\boldsymbol{\mu}) = \mu N_{r,\text{sig.}}^{\text{exp}} & \\ + \mu_{t\bar{t}\text{ true }\tau_{\text{had}}} N_{r,t\bar{t}\text{ true }\tau_{\text{had}}}^{\text{exp}} + \mu_{t\bar{t}\text{ fake }\tau_{\text{had}}} N_{r,t\bar{t}\text{ fake }\tau_{\text{had}}}^{\text{exp}} & \\ + \mu_{W+\text{jets}} N_{r,W+\text{jets}}^{\text{exp}} & \\ + \sum_{p}^{\text{other bkg. processes}} N_{r,p}^{\text{exp}}. & \end{aligned} \tag{9.6}$$

The systematic uncertainties are considered independent and included in $C_{\text{syst.}}$ as just the product of their probability distributions, $g(\theta_s)$. Each systematic uncertainty, s, is described by a nuisance parameter, θ_s, which parametrises the systematic uncertainty. For each parametrisation, θ_s, there is a nominal value and an up/down variation. All the systematic uncertainties in the likelihood function in this analysis are treated as Gaussian distributions with a mean of zero and a standard deviation of one, and so the parametrisation has to be transformed:

$$\frac{g(\theta_s) - g_0(\theta_s)}{\sigma(g(\theta_s))} \rightarrow g(\theta_s), \tag{9.7}$$

where $g_0(\theta_s)$ is the mean value of Gaussian distribution before normalisation, and $\sigma(g(\theta_s))$ is the standard deviation of the Gaussian distribution before normalisation.

9.1.2 Background-only fit

The background-only fit is implemented by maximising a likelihood function. A separate likelihood function and fit are created for each of the low-mass and high-mass lepton–hadron analyses. The background normalisation factors are a subset of the maximum-likelihood estimators.

The background-only fit is performed only in the control regions. The fit does not include any information about the number of observed events in the signal region nor

the validation region so that unbiased comparisons can be made of the observed and expected number of events in these regions. The control regions are assumed to have zero signal contamination, which is imposed by setting $\mu = 0$.

9.1.3 CLs

When the data in the signal region are statistically consistent with the Standard Model background, the results can be used to place bounds on new physics theories. In this section, CL_s will be defined and its usage explained. This quantity is used to perform statistical tests of background and signal hypotheses. Equation 9.8 defines CL_s as a ratio of two probabilities where one probability assumes the signal model exists and the other assumes the background-only hypothesis [159, 160]. A model is said to be excluded if $\mathrm{CL}_s < 0.05$ and in this way CL_s is used like a confidence level. All the different parts of the CL_s definition will be defined and described in this section. The procedure to calculate CL_s is further described in Reference [160].

$$\mathrm{CL}_s\left(\mu\right) = \frac{P\left(\tilde{q}_\mu \geq \tilde{q}_\mu^{\mathrm{obs}} | \mu_t = \mu\right)}{P\left(\tilde{q}_\mu \geq \tilde{q}_\mu^{\mathrm{obs}} | \mu_t = 0\right)} \tag{9.8}$$

$$= \frac{\int_{\tilde{q}_\mu^{\mathrm{obs}}}^{\infty} f\left(\tilde{q}_\mu | \mu_t = \mu\right) \mathrm{d}\tilde{q}_\mu}{\int_{\tilde{q}_\mu^{\mathrm{obs}}}^{\infty} f\left(\tilde{q}_\mu | \mu_t = 0\right) \mathrm{d}\tilde{q}_\mu} \tag{9.9}$$

In ATLAS and CMS, CL_s is defined using the test statistic $\tilde{q}_\mu$, which is defined in Equation 9.10.

$$\tilde{q}_\mu = -2 \ln \frac{L\left(\mu, \hat{\hat{\boldsymbol{\mu}}}_{\text{dom. bkg.}}, \hat{\hat{\boldsymbol{\theta}}}\left(\mu\right)\right)}{L\left(\hat{\mu}, \hat{\boldsymbol{\mu}}_{\text{dom. bkg.}}, \hat{\boldsymbol{\theta}}\right)}, \qquad 0 \leq \hat{\mu} \leq \mu \tag{9.10}$$

This test statistic is a likelihood ratio where the likelihood function is defined by Equation 9.2. More details about this test statistic can be found in Reference [161]. The two likelihood functions in the definition of $\tilde{q}_\mu$ are calculated with different values of the signal strength μ, the nuisance parameters $\boldsymbol{\theta}$, and $\boldsymbol{\mu}_{\text{dom. bkg.}}$, where $\boldsymbol{\mu}_{\text{dom. bkg.}}$ is the set of scale factors for the dominant backgrounds that are associated with the control regions:

$$\boldsymbol{\mu}_{\text{dom. bkg.}} = \left[\mu_{t\bar{t}\text{ true }\tau_{\text{had}}}, \mu_{t\bar{t}\text{ fake }\tau_{\text{had}}}, \mu_{W+\text{jets}}\right] \tag{9.11}$$

For the lepton–hadron channel this means that there are four free normalisation factors in $\tilde{q}_\mu$ while all the other background normalisation factors are set to 1. In the denominator of Equation 9.10, $\hat{\mu}$, $\hat{\boldsymbol{\mu}}_{\text{dom. bkg.}}$, and $\hat{\boldsymbol{\theta}}$ are the values of μ, $\boldsymbol{\mu}_{\text{dom. bkg.}}$, and $\boldsymbol{\theta}$ that maximise the likelihood function. The likelihood function in the denominator, $L\left(\hat{\mu}, \hat{\boldsymbol{\mu}}_{\text{dom. bkg.}}, \hat{\boldsymbol{\theta}}\right)$, is the maximised unconditional likelihood function and $\hat{\mu}$, $\hat{\boldsymbol{\mu}}_{\text{dom. bkg.}}$, and $\hat{\boldsymbol{\theta}}$ are its maximum-likelihood estimators. In the numerator, μ is fixed (typically $\mu = 1$ to study the nominal signal strength), and the likelihood is calculated using the values of $\boldsymbol{\mu}_{\text{dom. bkg.}}$ and $\boldsymbol{\theta}$ that maximise the likelihood function for the fixed μ. The likelihood function in the numerator, $L\left(\mu, \hat{\hat{\boldsymbol{\mu}}}_{\text{dom. bkg.}}, \hat{\hat{\boldsymbol{\theta}}}\left(\mu\right)\right)$, is the conditional maximum-likelihood function for the chosen μ, and $\hat{\hat{\boldsymbol{\mu}}}_{\text{dom. bkg.}}$ and $\hat{\hat{\boldsymbol{\theta}}}$ are the corresponding conditional maximum-likelihood estimators. Since the signal contamination in the control regions is small, the maximum-likelihood estimators of $\boldsymbol{\mu}_{\text{dom. bkg.}}$ should be similar to the $\boldsymbol{\mu}_{\text{dom. bkg.}}$ values from the background-only fit.

Since both the likelihood functions in Equation 9.10 have to be ≥ 0 and the likelihood function in the denominator is the overall maximum-likelihood, the following limits can be set:

$$0 \leq \frac{L\left(\mu, \hat{\hat{\boldsymbol{\mu}}}_{\text{dom. bkg.}}, \hat{\hat{\boldsymbol{\theta}}}\left(\mu\right)\right)}{L\left(\hat{\mu}, \hat{\boldsymbol{\mu}}_{\text{dom. bkg.}}, \hat{\boldsymbol{\theta}}\right)} \leq 1. \tag{9.12}$$

This guarantees $\tilde{q}_\mu \geq 0$. Small values of $\tilde{q}_\mu$ correspond to $L\left(\mu, \hat{\hat{\boldsymbol{\mu}}}_{\text{dom. bkg.}}, \hat{\hat{\boldsymbol{\theta}}}\left(\mu\right)\right)$ $\sim L\left(\hat{\mu}, \hat{\boldsymbol{\mu}}_{\text{dom. bkg.}}, \hat{\boldsymbol{\theta}}\right)$, where the theory with the specified μ value gives results similar to the data. Large values of $\tilde{q}_\mu$ correspond to $L\left(\mu, \hat{\hat{\boldsymbol{\mu}}}_{\text{dom. bkg.}}, \hat{\hat{\boldsymbol{\theta}}}\left(\mu\right)\right)$ $\ll L\left(\hat{\mu}, \hat{\boldsymbol{\mu}}_{\text{dom. bkg.}}, \hat{\boldsymbol{\theta}}\right)$, where the data disfavour the theory with the specified μ.

The f functions in Equation 9.9 are the probability distribution functions of $\tilde{q}_\mu$. The variable μ_t is the true value for μ in the f distribution. The probability distribution function $f\left(\tilde{q}_\mu | \mu_t = 0\right)$ is the probability distribution of $\tilde{q}_\mu$ where the background-only hypothesis is true.

To be able to integrate over the f functions as done in Equation 9.9, the shapes of the distributions are required. The f distributions are determined using toy Monte Carlo event distributions (or "pseudo-data") where the "observed" values for the region event counts are randomly generated from Poisson distributions as defined in the likelihood function. The procedure of randomly generating the number of events in each

region makes use of the number of background events and the number of signal events scaled by μ_t. Every pseudo-data sample leads to a different $\tilde{q}_\mu$. Since the true values of the nuisance paramters are not known the pseudo-data should ideally also randomly generate the values of the nuisance paramters as well, but for practical reasons `HistFitter` sets the nuisance parameters to their central values [144]. Every maximisation of a likelihood function is done numerically. When numerically calculating the unconditional maximium-likelihood $L\left(\hat{\mu}, \hat{\boldsymbol{\mu}}_{\text{dom. bkg.}}, \hat{\boldsymbol{\theta}}\right)$ the maximum-likelihood estimator $\hat{\mu}$ should converge towards μ_t.

Returning to the definition of CL_s, the numerator of Equation 9.8 quantifies the level of agreement between the data and the signal plus background with the signal cross-section scaling factor set to μ and for the observed value of the test statistic, $\tilde{q}_\mu^{\text{obs}}$. The quantity $P\left(\tilde{q}_\mu \geq \tilde{q}_\mu^{\text{obs}} | \mu_t = \mu\right)$ can by itself be used to exclude signal models (e.g. reject a model if $P\left(\tilde{q}_\mu \geq \tilde{q}_\mu^{\text{obs}} | \mu_t = \mu\right) < 0.05$) but it will occasionally exclude models to which the analysis has little to no sensitivity. An exclusion can happen when the observed number of events undergoes a large downward fluctuation such that $\int_{\tilde{q}_\mu^{\text{obs}}}^{\infty} f\left(\tilde{q}_\mu | \mu_t = \mu\right) \mathrm{d}\tilde{q}_\mu < 0.05$ and $\int_{\tilde{q}_\mu^{\text{obs}}}^{\infty} f\left(\tilde{q}_\mu | \mu_t = 0\right) \mathrm{d}\tilde{q}_\mu < 0.05$ (i.e. $\tilde{q}_\mu^{\text{obs}}$ is in the tail of both the $f\left(\tilde{q}_\mu | \mu_t = \mu\right)$ and $f\left(\tilde{q}_\mu | \mu_t = 0\right)$ distributions). The CL_s variable is protected against this because it is conservatively scaled to be larger than $P\left(\tilde{q}_\mu \geq \tilde{q}_\mu^{\text{obs}} | \mu_t = \mu\right)$ by using a measure of the compatibility of the data with the background-only hypothesis, $P\left(\tilde{q}_\mu \geq \tilde{q}_\mu^{\text{obs}} | \mu_t = 0\right)$. When the analysis has a strong separation between the signal and background then the $P\left(\tilde{q}_\mu \geq \tilde{q}_\mu^{\text{obs}} | \mu_t = 0\right)$ in the denominator will only create a small difference between CL_s and $P\left(\tilde{q}_\mu \geq \tilde{q}_\mu^{\text{obs}} | \mu_t = \mu\right)$. When the analysis has little sensitivity to the signal and a fluctuation occurs that could lead to incorrectly excluding the signal, then the denominator in the CL_s variable is small and penalises $P\left(\tilde{q}_\mu \geq \tilde{q}_\mu^{\text{obs}} | \mu_t = \mu\right)$.

9.2 Limit results

In this analysis, a CL_s value is calculated for every generated signal grid point in the stop-stau mass plane. The signal grid points are shown in the exclusion plot (Figure 9.6) shown later in this chapter. Whenever $\text{CL}_s\left(\mu = 1 | m_{\tilde{t}_1}, m_{\tilde{\tau}_1}\right) < 0.05$ then that signal point is excluded at the 95% confidence level. Since the signal grid is discrete, `ROOT` is used to interpolate the contour line between adjacent signal grid points. It is also possible to calculate an upper limit on the cross-section of the signal by finding the μ value for which $\text{CL}_s\left(\mu | m_{\tilde{t}_1}, m_{\tilde{\tau}_1}\right) < 0.05$. These are all model-

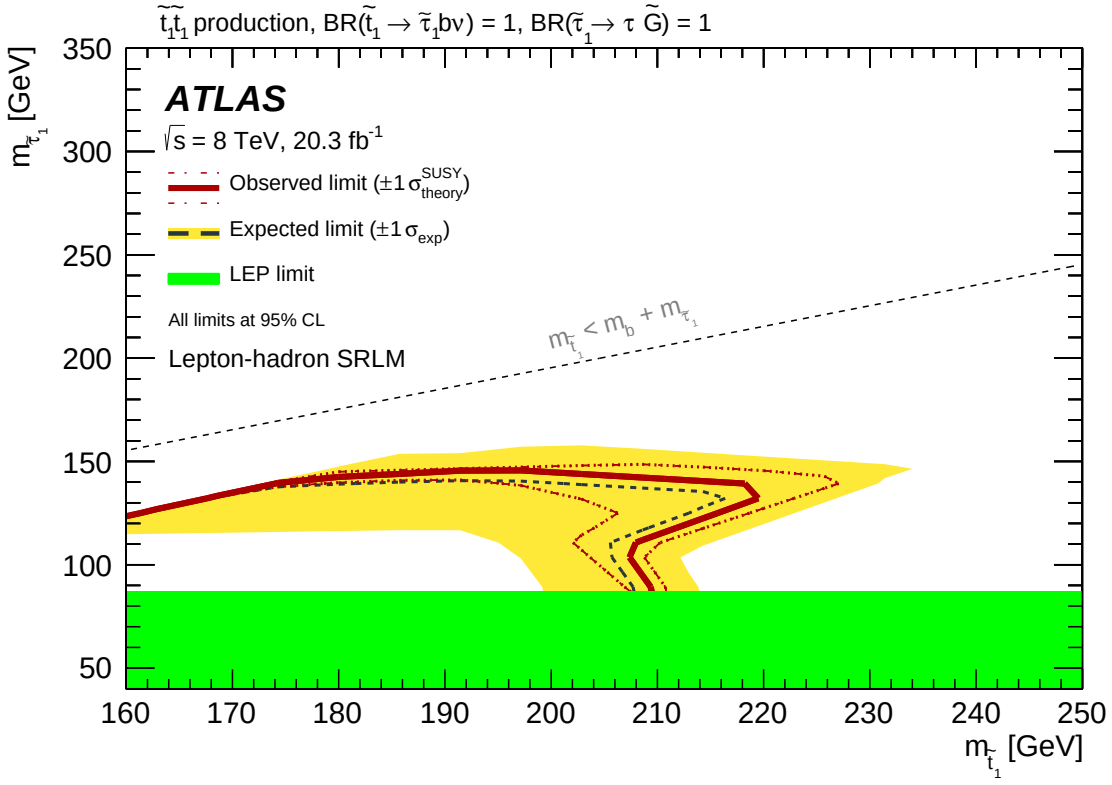

Figure 9.1: Observed and expected exclusion contours at 95% CL in the stop-stau mass plane from the lepton–hadron low-mass selection. The dashed and solid lines show the 95% CL expected and observed limits, respectively, including all uncertainties except for the theoretical signal cross-section uncertainty. The band around the expected limit shows the $\pm 1\sigma$ expectation. The dotted $\pm 1\sigma$ lines around the observed limit represent the results obtained when varying the nominal signal cross-section up or down by the theoretical uncertainty. The LEP limit on the mass of the scalar tau is also shown. This figure was taken from Reference [57].

dependent exclusions. Model-independent exclusions are also set using CL_s and will be described in Section 9.2.4. The exclusion limits are derived for the scalar top simplified model assuming 100% branching ratios for all the supersymmetric particle decays.

9.2.1 Lepton-hadron limits

The exclusion curves for the low-mass and high-mass signal regions of the lepton–hadron analysis are shown in Figures 9.1 and 9.2 respectively.

All the area within the solid red curve is the region of phase space that is excluded by the observed data. The systematic uncertainties for the signal are included in

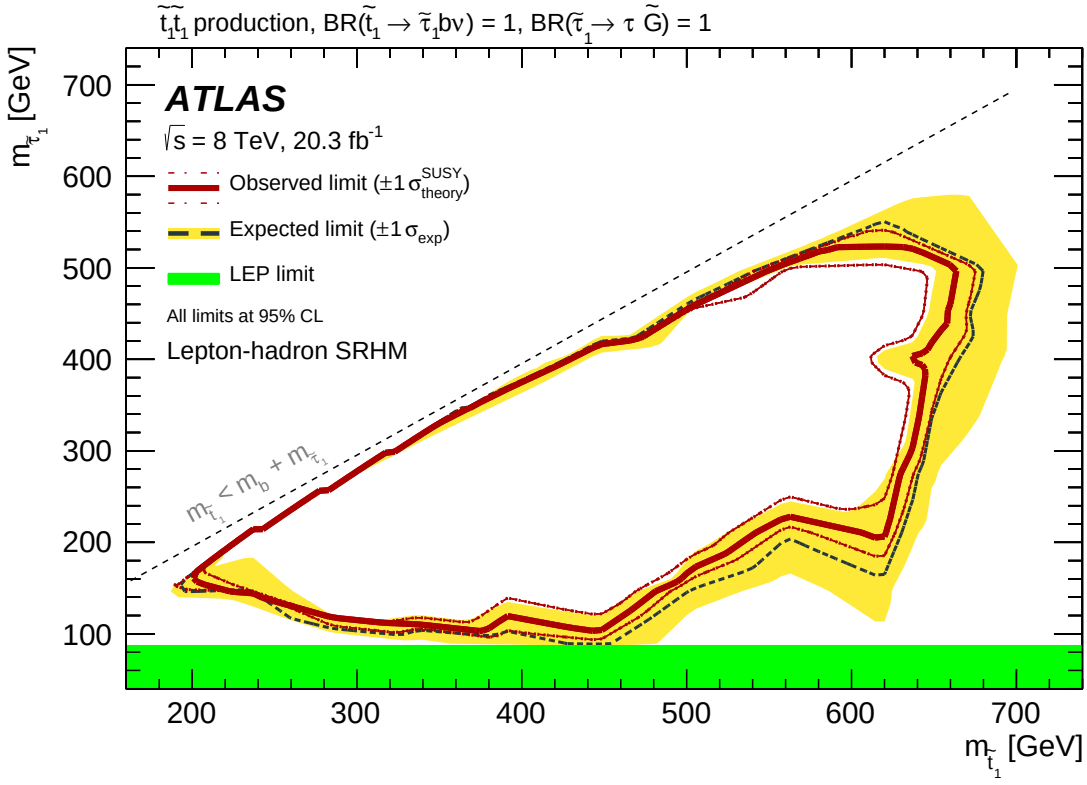

Figure 9.2: Observed and expected exclusion contours at 95% CL in the stop-stau mass plane from the lepton–hadron high-mass selection. The dashed and solid lines show the 95% CL expected and observed limits, respectively, including all uncertainties except for the theoretical signal cross-section uncertainty. The band around the expected limit shows the $\pm 1\sigma$ expectation. The dotted $\pm 1\sigma$ lines around the observed limit represent the results obtained when varying the nominal signal cross-section up or down by the theoretical uncertainty. The LEP limit on the mass of the scalar tau is also shown. This figure was taken from Reference [57].

the same way as the systematic uncertainties for the background processes, with the exception of the signal cross-section, which is included as $\pm 1\sigma$ variations to the observed limit and shown as separate dotted red curves. The area encompassed by the dotted black curve shows the expected exclusion region. The yellow bands around the expected exclusion contour line represent the $\pm 1\sigma$ expectations. The green area indicates the LEP exclusion of scalar tau masses below 87 GeV as discussed in Section 6.1. The LEP limit is based on direct searches for scalar tau pair production, and is valid for all scalar top masses. The dotted grey line shows the kinematic limit of the decay of a scalar top into a scalar tau: $m_{\tilde{t}_1} < m_b + m_{\tilde{\tau}_1}$.

In Figure 9.1 the exclusion curve excludes low scalar top and scalar tau masses,

which is approximately the region of phase space where the SRLM selection was designed to be sensitive. The exclusion curve does not get very close to the $m_{\tilde{t}_1} < m_b + m_{\tilde{\tau}_1}$ kinematic limit; the signal region was not designed to be sensitive to the signal in this part of phase space because it was covered by the lepton–lepton analysis. By design, the low mass signal region focuses on low mass scalar tops with cuts like $m_{\mathrm{T2}}(\mathrm{b}\ell, \mathrm{b}) < 100$ GeV and so there is also a maximum scalar top mass limit for the exclusion contour. The exact value of what the maximum value should be cannot easily be determined from either the $m_{\mathrm{T2}}(\mathrm{b}\ell, \mathrm{b}) < 100$ GeV cut or the $m_{\mathrm{T2}}(\mathrm{b}\ell, \mathrm{b}\tau_{\mathrm{had}}) < 60$ GeV cut because of the nature of these variables. This is partly because m_{T2} variables are kinematically limited from above, not below, by the mass of the parent particle, and because the $m_{\mathrm{T2}}(\mathrm{b}\ell, \mathrm{b})$ definition assumes a W boson mass in the decay chain while there are no W bosons in the signal process. The expected and observed exclusion limit contours have approximately the same complicated shape for scalar top masses in the range of roughly 200 GeV to 220 GeV, for example the point $(m_{\tilde{t}_1}, m_{\tilde{\tau}_1}) = (214, 130)$ GeV is within the expected and observed exclusion contours but $(m_{\tilde{t}_1}, m_{\tilde{\tau}_1}) = (214, 100)$ GeV is within neither contour. This is partly because the low-mass signal region becomes more sensitive to the signal as the scalar tau mass increases (until the kinematic limit effects come into play). This gain in sensitivity is partly the result of the $\left(p_{\mathrm{T}}^{\ell} + p_{\mathrm{T}}^{\tau_{\mathrm{had}}}\right)/m_{\mathrm{eff}} > 0.2$ cut. The gain in sensitivity of the signal region with increasing scalar tau masses counters the decrease in sensitivity of the SR to the signal with increasing scalar top masses.

The high-mass analysis expected and observed exclusion contours in Figure 9.2 also have shapes that are similar to each other and relatively complex. The contours do not get very close to the kinematic limit, just as was the case with the low-mass analysis and for the same reasons. The high-mass signal region was designed to be sensitive to higher scalar top masses with the cut $m_{\mathrm{T2}}(\mathrm{b}\ell, \mathrm{b}\tau_{\mathrm{had}}) > 180$ GeV and so the exclusion contours only extend to scalar top masses as low as approximately this cut value. The production cross-section of pair-produced scalar tops decreases as the mass of the scalar top increases and so there is also an upper limit to the mass of a scalar top that can be excluded, which gives the right edge of the expected and observed exclusion contours. The most powerful cut in the high-mass analysis is the $m_{\mathrm{T2}}(\ell, \tau_{\mathrm{had}}) > 120$ GeV cut, which accepts more signal events as the mass of the scalar tau increases. The result is similar to the situation in the low-mass analysis: the higher the scalar tau mass, the higher the mass of the scalar top that is excluded (expected and observed).

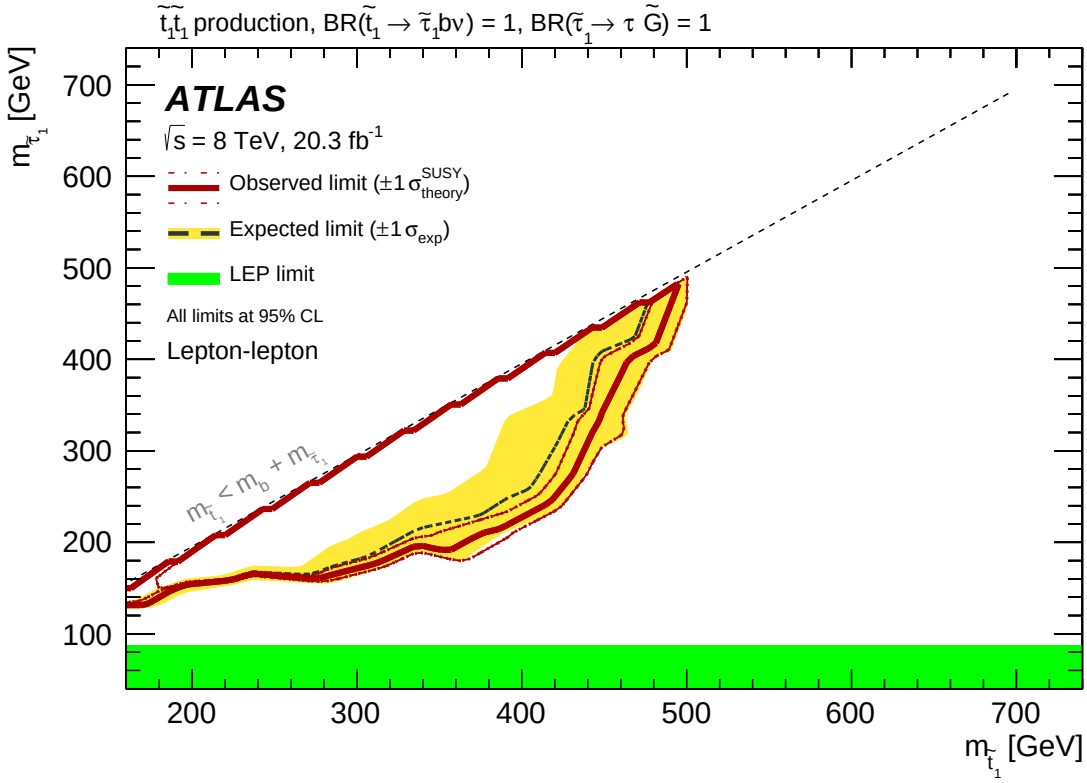

Figure 9.3: Observed and expected exclusion contours at 95% CL in the stop-stau mass plane from the lepton–lepton selections of Reference [133]. The dashed and solid lines show the 95% CL expected and observed limits, respectively, including all uncertainties except for the theoretical signal cross-section uncertainty. The band around the expected limit shows the $\pm 1\sigma$ expectation. The dotted $\pm 1\sigma$ lines around the observed limit represent the results obtained when varying the nominal signal cross-section up or down by the theoretical uncertainty. The LEP limit on the mass of the scalar tau is also shown. This figure was taken from Reference [57].

The shape of the exclusion contours will further discussed in Section 9.2.3 after the introduction of the exclusion contours from the other analysis channels.

9.2.2 Lepton-lepton and hadron-hadron limits

The exclusion limits for the lepton–lepton channel and the hadron–hadron channel are shown in Figures 9.3 and 9.4. These plots are taken from Reference [57]. As expected from the design of the lepton–lepton analysis, the exclusion contour extends very close to the kinematic limit line. The exclusion contour of the hadron–hadron analysis is also as expected because the signal region was designed to be sensitive to very low scalar tau masses for a wide range of scalar top masses.

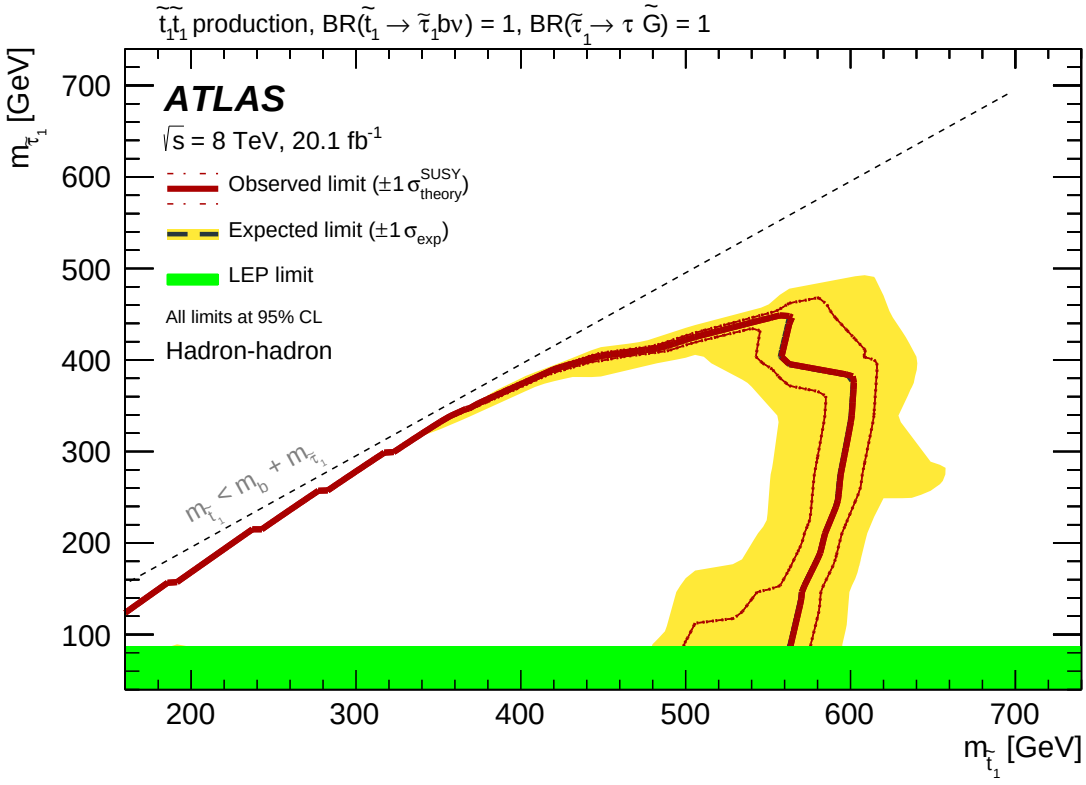

Figure 9.4: Observed and expected exclusion contours at 95% CL in the stop-stau mass plane from the hadron–hadron selection. The dashed and solid lines show the 95% CL expected and observed limits, respectively, including all uncertainties except for the theoretical signal cross-section uncertainty. The band around the expected limit shows the $\pm 1\sigma$ expectation. The dotted $\pm 1\sigma$ lines around the observed limit represent the results obtained when varying the nominal signal cross-section up or down by the theoretical uncertainty. The LEP limit on the mass of the scalar tau is also shown. This figure was taken from Reference [57].

9.2.3 Combined limits

For each point in the stop-stau mass plane an expected exclusion limit (CL_s) is calculated for both the lepton–hadron signal regions, the hadron–hadron signal region, and the lepton–lepton analysis. For the lepton–lepton analysis, several signal regions were statistically combined to calculate the exclusion limits (see [133] for details). Figure 9.5 shows the expected and observed exclusions from the combination of the three analysis channels. The combined exclusion plot uses at each individual grid point the selection that gives the best expected exclusion (the smallest expected CL_s value).

The same exclusion curve is also shown in Figure 9.6, which has an overlay identifying the analysis that produces the best expected exclusion for each grid point. Figure 9.7 has an overlay giving the expected 95% CL excluded cross-section times branching ratio values, where BR $\left(\tilde{t}_1 \rightarrow \tilde{\tau}_1 b\nu\right) = 1$ and BR $\left(\tilde{\tau}_1 \rightarrow \tau\tilde{G}\right) = 1$. These values are calculated by first determining the μ value that gives $CL_s = 0.05$, which is represented by $\mu^{95\%}$. This is performed using a scan of μ values. The excluded cross-section times branching ratio values in the figure overlay are calculated as $\mu^{95\%} \times \sigma_{signal}\left(m_{\tilde{t}_1}\right)$, where $\sigma_{signal}\left(m_{\tilde{t}_1}\right)$ is the production cross-section of the signal associated with the specific signal grid point.

The convention for quoting numerical values for the masses that are excluded by the data is based on the -1σ theoretical exclusion contours (the more conservative dotted red curve). As can be seen from Figure 9.5, the analyses together exclude models with a scalar top mass below approximately 490 GeV for all possible masses of the scalar tau. Depending on the mass of the scalar tau some models with a scalar top mass can be excluded up to approximately 640 GeV. The figure does not show scalar top masses below 150 GeV because if a scalar top did exist with a mass in this range it would have been detected by the ATLAS, CMS, and Tevatron measurements of the $t\bar{t}$ cross-section [162, 163, 164, 165, 166, 167]. The cross-section times branching ratio of the decay of a pair of scalar tops to two tau leptons for scalar top masses below 150 GeV could be approximately 25 times larger than that of the dominant $t\bar{t}$ background decaying into the same di-tau final state.

Some of the exclusion contour shape features are not the result of the physics but the result of the contour interpolation tools coupled with the fact that a discrete grid of signal points is used. The dependence of the contour shape on the discrete sampling of the stop-stau mass plane is most visible in Figure 9.6. The staircase

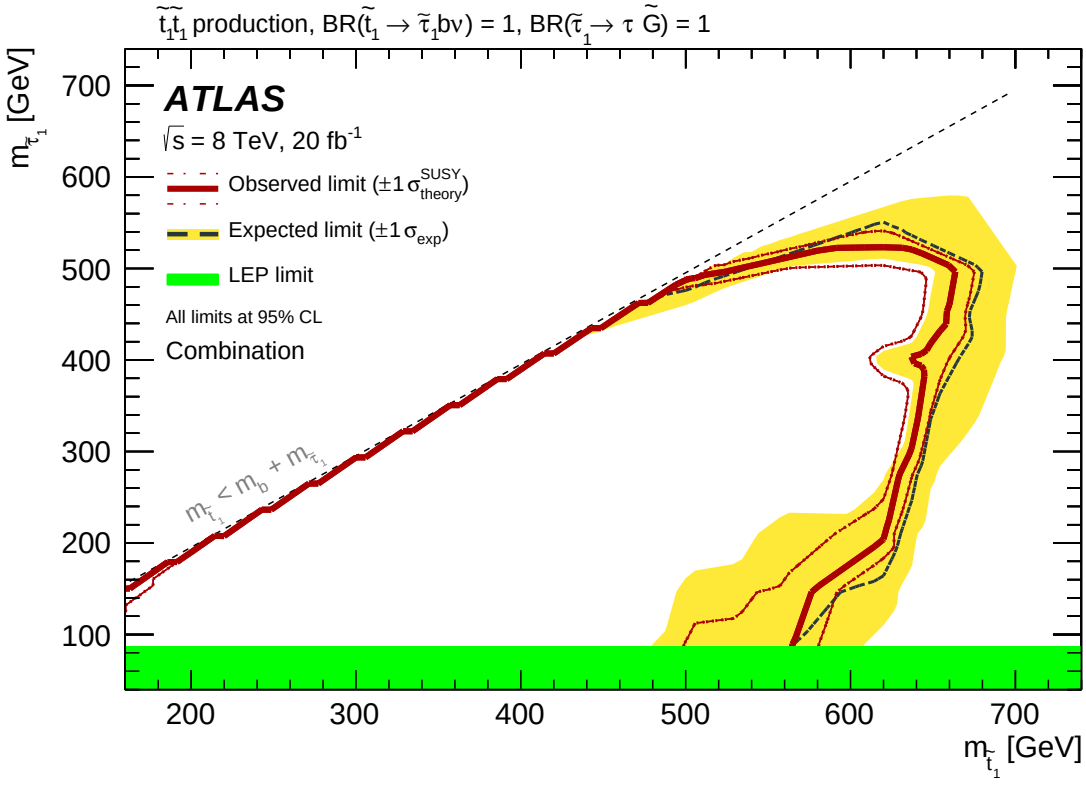

Figure 9.5: Observed and expected exclusion contours at 95% CL in the stop-stau mass plane from the combination of all selections. The dashed and solid lines show the 95% CL expected and observed limits, respectively, including all uncertainties except for the theoretical signal cross-section uncertainty. The band around the expected limit shows the $\pm 1\sigma$ expectation. The dotted $\pm 1\sigma$ lines around the observed limit represent the results obtained when varying the nominal signal cross-section up or down by the theoretical uncertainty. The LEP limit on the mass of the scalar tau is also shown. This figure was taken from Reference [57].

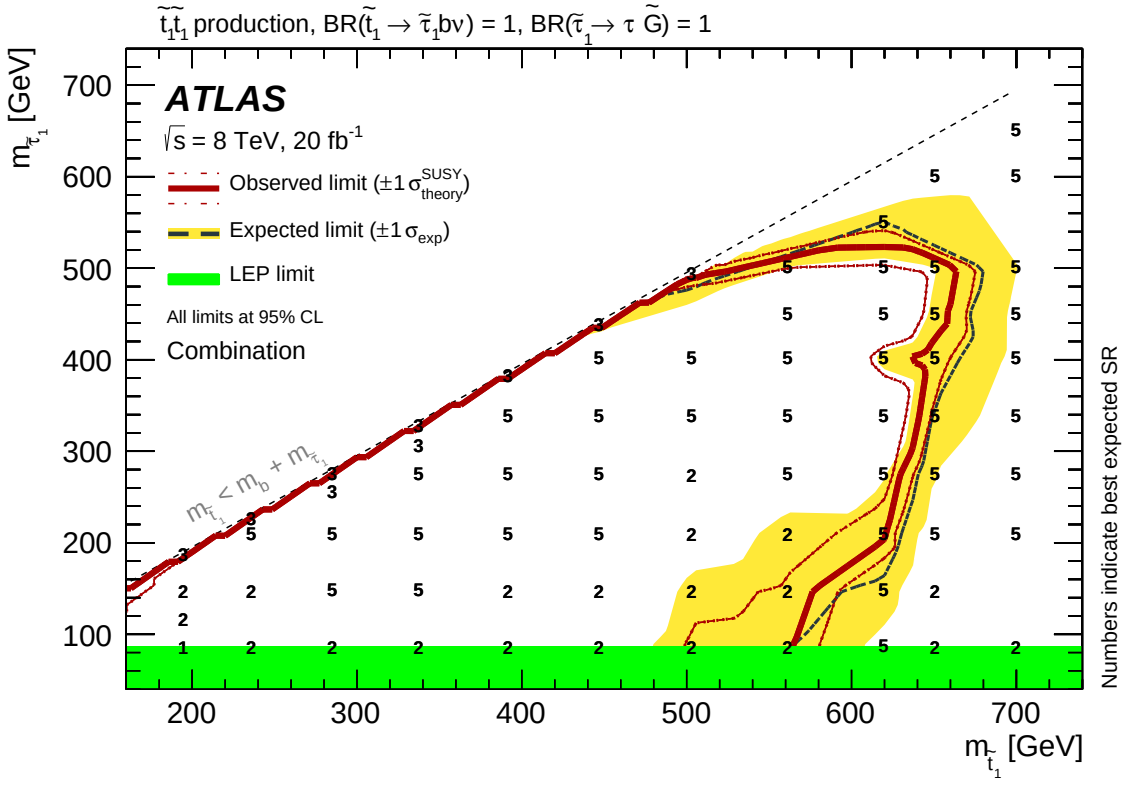

Figure 9.6: Observed and expected exclusion contours at 95% CL in the stop-stau mass plane from the combination of all selections. The dashed and solid lines show the 95% CL expected and observed limits, respectively, including all uncertainties except for the theoretical signal cross-section uncertainty. The band around the expected limit shows the $\pm 1\sigma$ expectation. The dotted $\pm 1\sigma$ lines around the observed limit represent the results obtained when varying the nominal signal cross-section up or down by the theoretical uncertainty. The numbers indicate which analysis gave the best exclusion for the combined: 1=lepton–hadron SRLM, 2=hadron–hadron, 3=lepton–lepton, 5=lepton–hadron SRHM. This figure was taken from Reference [57].

shape of the exclusion contours near the kinematic limit line is not physical but an artifact from the way that ROOT interpolates the contour line. Another artifact from the contour interpolation is around the signal point $\left(m_{\tilde{t}_1}, m_{\tilde{\tau}_1}\right) = (640, 400)$ GeV. The exclusion contour line should pass through this point based on the interpolation of the CL_s values between the grid points above and below this one; however, this point itself has a CL_s value that is slightly above the exclusion threshold and so the contour line takes a detour around the point. At some locations in the signal grid there are gaps and the interpolation of the expected, observed, and $\pm 1\sigma$ contour lines through these areas may be less accurate. This is the case around the points $\left(m_{\tilde{t}_1}, m_{\tilde{\tau}_1}\right) \sim (500, 460), (640, 550), (700, 550)$ GeV, and along the kinematic limit line for $m\left(\tilde{t}_1\right) \gtrsim 500$ GeV. The extrapolation function only uses adjacent points along the horizontal and vertical directions so the missing point at $\left(m_{\tilde{t}_1}, m_{\tilde{\tau}_1}\right) \sim (700, 140)$ GeV has no effect on the contour lines.

9.2.4 Model-independent limits

To make the results more useful (e.g. for theorists studying different signal models), limits are also set in a model-independent way. The procedure to calculate the model-independent limits is very similar to how the model-dependent $\mu^{95\%}$ limits are calculated but with a few modifications. In the model-independent calculation the number of expected events from a signal in the signal region is set to one ($N^{\text{exp.}}_{r,\text{sig.}} = 1$), and the signal contamination set to zero in the control regions. Again, a scan over μ is used to determine the value of μ that gives $\mathrm{CL}_s = 0.05$, which will be referred to as $\mu^{\text{ind.}}$. The expected and observed upper limits on the number of events from physics beyond the Standard Model at the 95% confidence level are represented by $S^{95}_{\text{exp.}}$, and $S^{95}_{\text{obs.}}$ respectively, and for each signal region can be calculated very simply as:

$$S^{95}_{\text{obs.(exp.)}} = \mu^{\text{ind.}}_{\text{obs.(exp.)}} N^{\text{exp.}}_{SR,\text{sig.}} \tag{9.13}$$

$$= \mu^{\text{ind.}}_{\text{obs.(exp.)}}. \tag{9.14}$$

With the total integrated luminosity, one can calculate an upper limit on the expected and observed "visible cross-sections", represented by $\sigma^{\text{exp.}}_{vis}$ and $\sigma^{\text{obs.}}_{vis}$ respectively. The calculation for the observed (expected) visible cross-section is simply

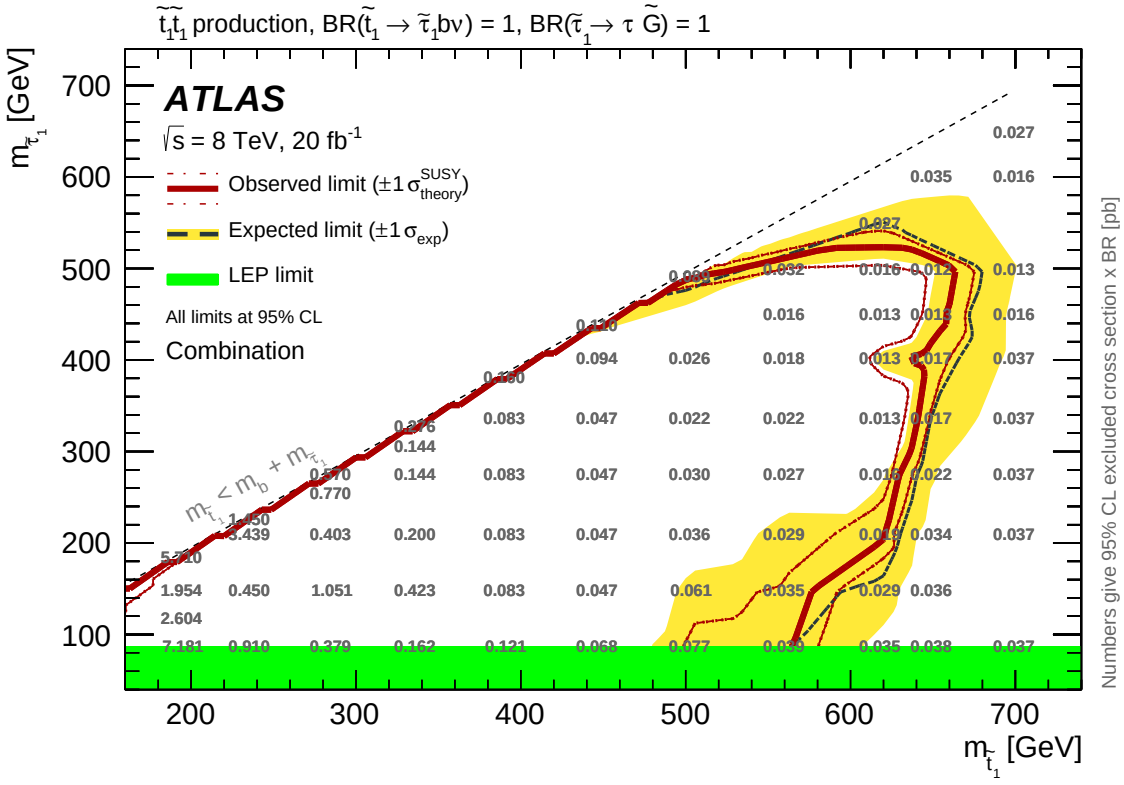

Figure 9.7: Observed and expected exclusion contours at 95% CL in the stop-stau mass plane from the combination of all selections. The dashed and solid lines show the 95% CL expected and observed limits, respectively, including all uncertainties except for the theoretical signal cross-section uncertainty. The band around the expected limit shows the $\pm 1\sigma$ expectation. The dotted $\pm 1\sigma$ lines around the observed limit represent the results obtained when varying the nominal signal cross-section up or down by the theoretical uncertainty. The numbers indicate the 95% CL excluded cross-section times branching ratio in picobarns. This figure was taken from Reference [57].

$$\sigma_{vis}^{\text{obs.(exp.)}} = \frac{S_{\text{obs.(exp.)}}^{95}}{\int L\mathrm{d}t}, \tag{9.15}$$

where $\int L dt$ is the integrated luminosity usable for the analysis channel. The observed (expected) visible cross-section is defined as

$$\sigma_{vis}^{\text{obs.(exp.)}} = \mathcal{A}\epsilon\sigma, \tag{9.16}$$

where $\mathcal{A}$ is the acceptance defined as the fraction of events passing the geometric and kinematic selections at particle level, ϵ is the detector reconstruction, identification and trigger efficiency, and σ is the production cross-section for a signal of physics beyond the Standard Model. The model-independent upper limits for the lepton–hadron channel are shown in Table 9.1.

Table 9.1: Left to right: Total constrained background yields, number of observed events, 95% CL observed (expected) upper limits on the number of BSM events, $S_{\text{obs.(exp.)}}^{95}$, and the visible cross-section, $\sigma_{vis}^{\text{obs.(exp.)}}$.

Signal Region	Background	Observation	$S_{\text{obs.(exp.)}}^{95}$	$\sigma_{vis}^{\text{obs.(exp.)}}$ [fb]
SRLM	22.1 ± 4.7	20	$12.4\ \left(13.2^{+4.9}_{-3.5}\right)$	$0.61\ \left(0.65^{+0.24}_{-0.17}\right)$
SRHM	2.1 ± 1.5	3	$6.4\ \left(5.2^{+2.6}_{-0.9}\right)$	$0.31\ \left(0.26^{+0.13}_{-0.04}\right)$

Chapter 10

Conclusions

A search for the pair production of scalar tops decaying to two tau leptons and large amounts of missing transverse momentum was conducted using 20 fb^{-1} of proton–proton collision data at $\sqrt{s} = 8$ TeV, collected by the ATLAS experiment at the LHC in 2012. The search was made using events with either two hadronically decaying taus, two light leptons, or one hadronically decaying tau and one light lepton.

The focus of this work was on the channel including one hadronically decaying tau and one leptonically decaying tau. Two signal regions were defined, one to search for scalar tops with masses similar to or smaller than the top-quark mass (SRLM) and a second one (SRHM) to search for scalar tops that are heavier than the top quark. Three control regions were also defined for each signal region to normalise the simulated dominant backgrounds with true or fake hadronically decaying taus to the data. The results of the normalisations were tested in the validation regions, of which there was one for each signal region. The selections defining the signal regions, control regions, and validation regions for the low-mass and high-mass lepton–hadron analyses were defined in Tables 6.1 and 6.2 respectively.

The results from the lepton–lepton, lepton–hadron, and hadron–hadron channels were in agreement with the Standard Model predictions and so limits were set at the 95% confidence level assuming the nominal production cross-section minus 1σ. For the specific model being studied, scalar tops with a mass below approximately 490 GeV were excluded for all masses of the scalar tau. Lower limits on the scalar top mass were set between 490 and 640 GeV for scalar tau masses between the LEP limit of 87 GeV and the kinematic limit of $m_{\tilde{t}_1} < m_b + m_{\tilde{\tau}_1}$. The excluded region of the stop-stau mass plane from the combination of all three channels is shown in Figure

9.5. Table 9.1 gives the model-independent upper limits on the visible cross-sections associated with the two lepton–hadron signal regions.

This research did not find any evidence for new physics, but the lower limits on the scalar top mass are eating away at the available phase space for the existence of a scalar top. As searches for the scalar top exclude the particle at higher and higher masses, the ability for supersymmetry to address the fine-tuning problem is weakened. Since supersymmetry has many free parameters it is very difficult for experiments to exclude the entire phase space of the theory; however, if the ability of the theory to address the open questions in particle physics is sufficiently weakened then the theory may be excluded in the relevant phase space. This work adds to the growing set of scalar top searches that are excluding scalar tops to higher and higher masses and may one day eventually lead to a discovery of new physics or a change in focus of searches for new physics.

Bibliography

[1] S. L. Glashow, *Partial Symmetries of Weak Interactions*, Nucl. Phys. **22** (1961) 579–588.

[2] S. Weinberg, *A Model of Leptons*, Phys. Rev. Lett. **19** (1967) 1264–1266.

[3] A. Salam, *Weak and Electromagnetic Interactions*, Conf. Proc. **C680519** (1968) 367–377.

[4] S. Raby, *Supersymmetric grand unified theories: from quarks to strings via SUSY GUTs*. Lecture notes in physics. Springer, Cham, 2017. https://cds.cern.ch/record/2267303.

[5] ATLAS Collaboration, *Observation of a new particle in the search for the Standard Model Higgs boson with the ATLAS detector at the LHC*, Physics Letters B **716** (2012) no. 1, 1 – 29. http://www.sciencedirect.com/science/article/pii/S037026931200857X.

[6] CMS Collaboration, *Observation of a new boson at a mass of 125 GeV with the CMS experiment at the LHC*, Physics Letters B **716** (2012) no. 1, 30 – 61. http://www.sciencedirect.com/science/article/pii/S0370269312008581.

[7] *Standard Model of Elementary Particles*, retrieved March, 2014. https://upload.wikimedia.org/wikipedia/commons/archive/0/00/20140219193253%21Standard_Model_of_Elementary_Particles.svg.

[8] *Elementary particle interactions*, retrieved March, 2014. https://upload.wikimedia.org/wikipedia/commons/4/4c/Elementary_particle_interactions.svg.

[9] I. J. R. Aitchison and A. J. G. Hey, *Gauge theories in particle physics: A practical introduction. Vol. 1: From relativistic quantum mechanics to QED*. CRC Press, Bristol, UK, 2012.

[10] C. Patrignani and others (Particle Data Group), *Review of Particle Physics*, Chin. Phys. **C40** (2016) no. 10, 100001.

[11] M. E. Peskin and D. V. Schroeder, *An Introduction to Quantum Field Theory; 1995 ed.* Westview, Boulder, CO, 1995.

[12] Super-Kamiokande Collaboration, Y. Fukuda et al., *Evidence for Oscillation of Atmospheric Neutrinos*, Phys. Rev. Lett. **81** (Aug, 1998) 1562–1567. http://link.aps.org/doi/10.1103/PhysRevLett.81.1562.

[13] SNO Collaboration, Q. R. Ahmad et al., *Measurement of the Rate of $\nu_e + d \to p + p + e^-$ Interactions Produced by ^8B Solar Neutrinos at the Sudbury Neutrino Observatory*, Phys. Rev. Lett. **87** (Jul, 2001) 071301. http://link.aps.org/doi/10.1103/PhysRevLett.87.071301.

[14] SNO Collaboration, Q. R. Ahmad et al., *Direct Evidence for Neutrino Flavor Transformation from Neutral-Current Interactions in the Sudbury Neutrino Observatory*, Phys. Rev. Lett. **89** (Jun, 2002) 011301. http://link.aps.org/doi/10.1103/PhysRevLett.89.011301.

[15] S. M. Bilenky and S. T. Petcov, *Massive neutrinos and neutrino oscillations*, Rev. Mod. Phys. **59** (Jul, 1987) 671–754. https://link.aps.org/doi/10.1103/RevModPhys.59.671.

[16] C. P. Burgess, *Quantum gravity in everyday life: General relativity as an effective field theory*, Living Rev. Rel. **7** (2004) 5–56, arXiv:gr-qc/0311082 [gr-qc].

[17] L. Canetti, M. Drewes, and M. Shaposhnikov, *Matter and Antimatter in the Universe*, New J. Phys. **14** (2012) 095012, arXiv:1204.4186 [hep-ph].

[18] O. Eberhardt, G. Herbert, H. Lacker, A. Lenz, A. Menzel, U. Nierste, and M. Wiebusch, *Impact of a Higgs Boson at a Mass of 126 GeV on the Standard Model with Three and Four Fermion Generations*, Phys. Rev. Lett. **109** (Dec, 2012) 241802. https://link.aps.org/doi/10.1103/PhysRevLett.109.241802.

[19] V. C. Rubin, N. Thonnard, and W. K. Ford, Jr., *Rotational properties of 21 SC galaxies with a large range of luminosities and radii, from NGC 4605 /R = 4kpc/ to UGC 2885 /R = 122 kpc/*, Astrophys. J. **238** (1980) 471.

[20] D. Clowe, M. Bradac, A. H. Gonzalez, M. Markevitch, S. W. Randall, C. Jones, and D. Zaritsky, *A direct empirical proof of the existence of dark matter*, Astrophys. J. **648** (2006) L109–L113, arXiv:astro-ph/0608407 [astro-ph].

[21] G. Hinshaw, D. Larson, E. Komatsu, D. N. Spergel, C. L. Bennett, J. Dunkley, M. R. Nolta, M. Halpern, R. S. Hill, N. Odegard, L. Page, K. M. Smith, J. L. Weiland, B. Gold, N. Jarosik, A. Kogut, M. Limon, S. S. Meyer, G. S. Tucker, E. Wollack, and E. L. Wright, *Nine-year Wilkinson Microwave Anisotropy Probe (WMAP) Observations: Cosmological Parameter Results*, APJS **208** (Oct., 2013) 19, arXiv:1212.5226.

[22] S. Weinberg, *Implications of Dynamical Symmetry Breaking*, Phys. Rev. **D13** (1976) 974–996.

[23] E. Gildener, *Gauge Symmetry Hierarchies*, Phys. Rev. **D14** (1976) 1667.

[24] S. Weinberg, *Implications of Dynamical Symmetry Breaking: An Addendum*, Phys. Rev. **D19** (1979) 1277–1280.

[25] L. Susskind, *Dynamics of Spontaneous Symmetry Breaking in the Weinberg-Salam Theory*, Phys. Rev. **D20** (1979) 2619–2625.

[26] Planck Collaboration, P. Ade et al., *Planck 2013 results. XVI. Cosmological parameters*, Astron. Astrophys. **571** (Mar, 2013) A16. 69 p. http://cds.cern.ch/record/1530686.

[27] Planck Collaboration, P. Ade et al., *Planck 2015 results. XIII. Cosmological parameters*, Astron. Astrophys. **594** (Feb, 2016) A13. http://cds.cern.ch/record/1987166.

[28] The ATLAS Collaboration and the CMS Collaboration, *Combined Measurement of the Higgs Boson Mass in pp Collisions at $\sqrt{s} = 7$ and 8 TeV with the ATLAS and CMS Experiments*, Phys. Rev. Lett. **114** (2015) 191803, arXiv:1503.07589 [hep-ex].

[29] G. F. Giudice, *Naturally Speaking: The Naturalness Criterion and Physics at the LHC*, arXiv:0801.2562 [hep-ph].

[30] S. P. Martin, *A Supersymmetry primer*, arXiv:hep-ph/9709356 [hep-ph].

[31] H. Miyazawa, *Baryon Number Changing Currents*, Prog. Theor. Phys. **36 (6)** (1966) 1266–1276.

[32] P. Ramond, *Dual Theory for Free Fermions*, Phys. Rev. **D3** (1971) 2415–2418.

[33] Y. Golfand and E. Likhtman, *Extension of the Algebra of Poincare Group Generators and Violation of p Invariance*, JETP Lett. **13** (1971) 323–326.

[34] A. Neveu and J. H. Schwarz, *Factorizable dual model of pions*, Nucl. Phys. **B31** (1971) 86–112.

[35] A. Neveu and J. H. Schwarz, *Quark Model of Dual Pions*, Phys. Rev. **D4** (1971) 1109–1111.

[36] J. Gervais and B. Sakita, *Field theory interpretation of supergauges in dual models*, Nucl. Phys. **B34** (1971) 632–639.

[37] D. Volkov and V. Akulov, *Is the Neutrino a Goldstone Particle?*, Phys. Lett. **B46** (1973) 109–110.

[38] J. Wess and B. Zumino, *A Lagrangian Model Invariant Under Supergauge Transformations*, Phys. Lett. **B49** (1974) 52.

[39] J. Wess and B. Zumino, *Supergauge Transformations in Four-Dimensions*, Nucl. Phys. **B70** (1974) 39–50.

[40] H. W. Baer and X. Tata, *Weak scale supersymmetry: from superfields to scattering events*. Cambridge Univ. Press, Cambridge, 2006. https://cds.cern.ch/record/988941.

[41] F. Englert and R. Brout, *Broken Symmetry and the Mass of Gauge Vector Mesons*, Phys. Rev. Lett. **13** (Aug, 1964) 321–323. https://link.aps.org/doi/10.1103/PhysRevLett.13.321.

[42] P. W. Higgs, *Broken Symmetries and the Masses of Gauge Bosons*, Phys. Rev. Lett. **13** (Oct, 1964) 508–509. https://link.aps.org/doi/10.1103/PhysRevLett.13.508.

[43] P. Higgs, *Broken symmetries, massless particles and gauge fields*, Physics Letters **12** (1964) no. 2, 132 – 133. http://www.sciencedirect.com/science/article/pii/0031916364911369.

[44] G. S. Guralnik, C. R. Hagen, and T. W. B. Kibble, *Global Conservation Laws and Massless Particles*, Phys. Rev. Lett. **13** (Nov, 1964) 585–587. https://link.aps.org/doi/10.1103/PhysRevLett.13.585.

[45] P. W. Higgs, *Spontaneous Symmetry Breakdown without Massless Bosons*, Phys. Rev. **145** (May, 1966) 1156–1163. https://link.aps.org/doi/10.1103/PhysRev.145.1156.

[46] T. W. B. Kibble, *Symmetry Breaking in Non-Abelian Gauge Theories*, Phys. Rev. **155** (Mar, 1967) 1554–1561. https://link.aps.org/doi/10.1103/PhysRev.155.1554.

[47] H. E. Logan, *TASI 2013 lectures on Higgs physics within and beyond the Standard Model*, arXiv:1406.1786 [hep-ph].

[48] M. Dine and W. Fischler, *A Phenomenological Model of Particle Physics Based on Supersymmetry*, Phys. Lett. **B110** (1982) 227.

[49] L. Alvarez-Gaume, M. Claudson, and M. B. Wise, *Low-Energy Supersymmetry*, Nucl. Phys. **B207** (1982) 96.

[50] C. R. Nappi and B. A. Ovrut, *Supersymmetric Extension of the SU(3) × SU(2) × U(1) Model*, Phys. Lett. **B113** (1982) 175.

[51] M. Dine and A. E. Nelson, *Dynamical supersymmetry breaking at low-energies*, Phys. Rev. **D48** (1993) 1277–1287, arXiv:hep-ph/9303230.

[52] M. Dine, A. E. Nelson, and Y. Shirman, *Low-energy dynamical supersymmetry breaking simplified*, Phys. Rev. **D51** (1995) 1362–1370, arXiv:hep-ph/9408384.

[53] M. Dine, A. E. Nelson, Y. Nir, and Y. Shirman, *New tools for low-energy dynamical supersymmetry breaking*, Phys. Rev. **D53** (1996) 2658–2669, arXiv:hep-ph/9507378.

[54] S. Ambrosanio, S. Heinemeyer, B. Mele, S. Petrarca, G. Polesello, A. Rimoldi, and G. Weiglein, *Aspects of GMSB phenomenology at TeV colliders*, in *1st Les Houches Workshop on Physics at TeV Colliders (PhysTeV 1999) Les Houches, France, June 7-18, 1999*. 2000. arXiv:hep-ph/0002191 [hep-ph]. http://weblib.cern.ch/abstract?CERN-TH-2000-054.

[55] J. F. Donoghue, *Introduction to the effective field theory description of gravity*, in *Advanced School on Effective Theories Almunecar, Spain, June 25-July 1, 1995*. 1995. arXiv:gr-qc/9512024 [gr-qc]. http://alice.cern.ch/format/showfull?sysnb=0214301.

[56] F. D. Steffen, *Dark Matter Candidates - Axions, Neutralinos, Gravitinos, and Axinos*, Eur. Phys. J. **C59** (2009) 557–588, arXiv:0811.3347 [hep-ph].

[57] ATLAS Collaboration, *Search for direct top squark pair production in final states with two tau leptons in pp collisions at* $\sqrt{s} = 8$ *TeV with the ATLAS detector*, Eur. Phys. J. C **76** (2016) 81, arXiv:1509.04976 [hep-ex].

[58] LHC New Physics Working Group Collaboration, *Simplified Models for LHC New Physics Searches*, J. Phys. G **39** (May, 2011) 105005. 40 p. https://cds.cern.ch/record/1351158.

[59] ATLAS Collaboration, *ATLAS Run 1 searches for direct pair production of third-generation squarks at the Large Hadron Collider*, Eur. Phys. J. C **75** (Jun, 2015) 510. 54 p. http://cds.cern.ch/record/2029476.

[60] CMS Collaboration, *Inclusive search for supersymmetry using the razor variables in pp collisions at* $\sqrt{s} = 7$ *TeV*, Phys. Rev. Lett. **111** (2013) 081802, arXiv:1212.6961 [hep-ex].

[61] CMS Collaboration, *Search for supersymmetry in hadronic final states with missing transverse energy using the variables* α_T *and b-quark multiplicity in pp collisions at 8 TeV*, Eur. Phys. J. **C73** (2013) 2568, arXiv:1303.2985 [hep-ex].

[62] CMS Collaboration, *Search for top-squark pair production in the single-lepton final state in pp collisions at* $\sqrt{s} = 8$ *TeV*, Eur. Phys. J. **C73** (2013) 2677, arXiv:1308.1586 [hep-ex].

[63] CMS Collaboration, *Search for supersymmetry using razor variables in events with b-tagged jets in pp collisions at* $\sqrt{s} = 8$ *TeV*, Phys. Rev. **D91** (2015) 052018, arXiv:1502.00300 [hep-ex].

[64] CMS Collaboration, *Searches for supersymmetry using the* M_{T2} *variable in hadronic events produced in pp collisions at 8 TeV*, JHEP **1505** (2015) 078, arXiv:1502.04358 [hep-ex].

[65] CMS Collaboration, *Searches for third-generation squark production in fully hadronic final states in proton-proton collisions at* $\sqrt{s} = 8$ *TeV*, JHEP **1506** (2015) 116, arXiv:1503.08037 [hep-ex].

[66] E. A. Baltz, *Dark matter candidates*, eConf **C040802** (2004) L002, arXiv:astro-ph/0412170 [astro-ph].

[67] O. S. Brüning, P. Collier, P. Lebrun, S. Myers, R. Ostojic, J. Poole, and P. Proudlock, *LHC Design Report*. CERN, Geneva, 2004. http://cdsweb.cern.ch/record/782076/.

[68] ATLAS Collaboration, *The ATLAS Experiment at the CERN Large Hadron Collider*, JINST **3** (2008) S08003.

[69] J. Pequenao and P. Schaffner, *A computer generated image representing how ATLAS detects particles*, Jan, 2013.

[70] *ATLAS central solenoid: Technical Design Report*. Technical Design Report ATLAS. CERN, Geneva, 1997. http://cdsweb.cern.ch/record/331067?ln=en.

[71] M. L. Andrieux et al., *Construction and test of the first two sectors of the ATLAS barrel liquid argon presampler*, Nucl. Instrum. Methods Phys. Res., A **479** (2002) no. 2-3, 316–33.

[72] *ATLAS Magnetic System*, retrieved January, 2017. http://atlas-ma.web.cern.ch/atlas-ma/.

[73] *ATLAS Magnetic Field*, retrieved January, 2017. https://twiki.cern.ch/twiki/pub/Atlas/MagneticField/magplot.jpg.

[74] ATLAS Collaboration, *Expected Performance of the ATLAS Experiment - Detector, Trigger and Physics*, CERN-OPEN-2008-020 (2009) , arXiv:0901.0512 [hep-ex].

[75] ATLAS Collaboration, *Performance of the ATLAS Trigger System in 2010*, Eur. Phys. J. C **72** (2012) 1849, arXiv:1110.1530 [hep-ex].

[76] M. Stockton, *The ATLAS Level-1 Central Trigger*, Journal of Instrumentation **6** (2011) no. 01, C01075. Presentation given at Topical Workshop on Electronics for Particle Physics 2010, Aachen, Germany. Also under no. ATL-DAQ-PROC-2010-036.

[77] T. Pauly, *The ATLAS Level-1 Central Trigger System in Operation*, Journal of Physics: Conference Series **219** (2010) no. 2, 022017. http://cdsweb.cern.ch/record/1176568.

[78] ATLAS Collaboration, *ATLAS level-1 trigger: Technical Design Report.* Technical Design Report ATLAS. CERN, Geneva, 1998. https://cds.cern.ch/record/381429.

[79] ATLAS Collaboration, *ATLAS high-level trigger, data-acquisition and controls: Technical Design Report.* Technical Design Report ATLAS. CERN, Geneva, 2003. https://cds.cern.ch/record/616089.

[80] R. Achenbach et al., *The ATLAS Level-1 Calorimeter Trigger*, Journal of Instrumentation **3** (2008) no. 03, P03001. http://stacks.iop.org/1748-0221/3/i=03/a=P03001.

[81] ATLAS Collaboration, *ATLAS detector and physics performance: Technical Design Report, 1.* Technical Design Report ATLAS. CERN, Geneva, 1999. https://cds.cern.ch/record/391176.

[82] S. Ask et al., *The ATLAS central level-1 trigger logic and TTC system.* No. ATL-COM-DAQ-2008-006. Geneva, Aug, 2008. JINST 3 (2008) P08002.

[83] ATLAS Collaboration, *Performance of the ATLAS muon trigger in pp collisions at* $\sqrt{s} = 8$ *TeV*, Eur. Phys. J. **C75** (2015) 120, arXiv:1408.3179 [hep-ex].

[84] ATLAS Collaboration, *Topological cell clustering in the ATLAS calorimeters and its performance in LHC Run 1.* No. arXiv:1603.02934. CERN-PH-EP-2015-304. Geneva, Mar, 2016. https://cds.cern.ch/record/2138166.

[85] ATLAS Collaboration, *Reconstruction of primary vertices at the ATLAS experiment in Run 1 proton–proton collisions at the LHC.* No. arXiv:1611.10235. CERN-EP-2016-150. Geneva, Nov, 2016. https://cds.cern.ch/record/2235651.

[86] M. Cacciari, G. P. Salam, and G. Soyez, *The Anti-k(t) jet clustering algorithm*, JHEP **0804** (2008) 063, arXiv:0802.1189 [hep-ph].

[87] ATLAS Collaboration, *Jet energy measurement with the ATLAS detector in proton-proton collisions at* $\sqrt{s} = 7$ *TeV*, Eur. Phys. J. **C73** (2013) 2304, arXiv:1112.6426 [hep-ex].

[88] ATLAS Collaboration, *Jet energy measurement and its systematic uncertainty in proton-proton collisions at* $\sqrt{s}$*=7 TeV with the ATLAS detector*, Eur. Phys. J. C **75** (May, 2014) 17. 100 p. https://cds.cern.ch/record/1705576.

[89] ATLAS Collaboration, *A measurement of the calorimeter response to single hadrons and determination of the jet energy scale uncertainty using LHC Run-1 pp-collision data with the ATLAS detector.* No. CERN-EP-2016-149. arXiv:1607.08842. 1. Geneva, Jul, 2016. https://cds.cern.ch/record/2202682.

[90] ATLAS Collaboration, *Calibration of b-tagging using dileptonic top pair events in a combinatorial likelihood approach with the ATLAS experiment*, ATLAS-CONF-2014-004 (2014) . https://cdsweb.cern.ch/record/1664335.

[91] ATLAS Collaboration, *Calibration of the performance of b-tagging for c and light-flavour jets in the 2012 ATLAS data*, ATLAS-CONF-2014-046 (2014) . http://cdsweb.cern.ch/record/1741020.

[92] ATLAS Collaboration, *Electron and photon energy calibration with the ATLAS detector using LHC Run 1 data*, Eur. Phys. J. C (Jul, 2014) 74. 51 p. https://cds.cern.ch/record/1744017.

[93] ATLAS Collaboration, *Electron reconstruction and identification efficiency measurements with the ATLAS detector using the 2011 LHC proton-proton collision data*, Eur. Phys. J. **C74** (2014) 2941, arXiv:1404.2240 [hep-ex].

[94] *Electron efficiency measurements with the ATLAS detector using the 2012 LHC proton-proton collision data*. No. ATLAS-CONF-2014-032. Geneva, Jun, 2014. https://cds.cern.ch/record/1706245.

[95] ATLAS Collaboration, *Measurement of the muon reconstruction performance of the ATLAS detector using 2011 and 2012 LHC proton-proton collision data*, Eur. Phys. J. **C74** (2014) 3130, arXiv:1407.3935 [hep-ex].

[96] ATLAS Collaboration, *Identification and energy calibration of hadronically decaying tau leptons with the ATLAS experiment in pp collisions at* $\sqrt{s} = 8$ *TeV*, Eur. Phys. J. **C75** (2015) 303, arXiv:1412.7086 [hep-ex].

[97] ATLAS Collaboration, *Performance of the Reconstruction and Identification of Hadronic Tau Decays in ATLAS with 2011 Data*. No. ATLAS-CONF-2012-142. Geneva, Oct, 2012. https://cds.cern.ch/record/1485531.

[98] L. Breiman, J. Friedman, C. Stone, and R. Olshen, *Classification and Regression Trees*. The Wadsworth and Brooks-Cole statistics-probability series. Taylor & Francis, 1984.

[99] Y. Freund and R. E. Schapire, *A Decision-Theoretic Generalization of On-Line Learning and an Application to Boosting*, Journal of Computer and System Sciences **55** (1997) no. 1, 119 – 139. http://www.sciencedirect.com/science/article/pii/S002200009791504X.

[100] ATLAS Collaboration, *Performance of Missing Transverse Momentum Reconstruction in Proton-Proton Collisions at 7 TeV with ATLAS*, Eur. Phys. J. **C72** (2012) 1844, arXiv:1108.5602 [hep-ex].

[101] *Luminosity Public Results*, September, 2013. https://twiki.cern.ch/twiki/bin/view/AtlasPublic/LuminosityPublicResults.

[102] ATLAS Collaboration, *Improved luminosity determination in pp collisions at* $\sqrt{s} = 7$ *TeV using the ATLAS detector at the LHC*, Eur. Phys. J. **C73** (2013) 2518, arXiv:1302.4393 [hep-ex].

[103] M. Dobbs and J. B. Hansen, *The HepMC C++ Monte Carlo Event Record for High Energy Physics*. No. ATL-SOFT-2000-001. Geneva, Jun, 2000. https://cds.cern.ch/record/684090. revised version number 1 submitted on 2001-02-27 09:54:32.

[104] S. Alioli, P. Nason, C. Oleari, and E. Re, *A general framework for implementing NLO calculations in shower Monte Carlo programs: the POWHEG BOX*, JHEP **1006** (2010) 043, arXiv:1002.2581 [hep-ph].

[105] J. M. Campbell, R. K. Ellis, P. Nason, and E. Re, *Top-pair production and decay at NLO matched with parton showers*, JHEP **1504** (2015) 114, arXiv:1412.1828 [hep-ph].

[106] T. Sjöstrand, S. Mrenna, and P. Z. Skands, *A Brief Introduction to PYTHIA 8.1*, Comput. Phys. Common. **178** (2008) 852–867, arXiv:0710.3820 [hep-ph].

[107] M. Cacciari, M. Czakon, M. Mangano, A. Mitov, and P. Nason, *Top-pair production at hadron colliders with next-to-next-to-leading logarithmic soft-gluon resummation*, Phys. Lett. **B710** (2012) 612–622, arXiv:1111.5869 [hep-ph].

[108] P. Bärnreuther, M. Czakon, and A. Mitov, *Percent Level Precision Physics at the Tevatron: First Genuine NNLO QCD Corrections to $q\bar{q} \to t\bar{t} + X$*, Phys. Rev. Lett. **109** (2012) 132001, arXiv:1204.5201 [hep-ph].

[109] M. Czakon and A. Mitov, *NNLO corrections to top-pair production at hadron colliders: the all-fermionic scattering channels*, JHEP **1212** (2012) 054, arXiv:1207.0236 [hep-ph].

[110] M. Czakon and A. Mitov, *NNLO corrections to top pair production at hadron colliders: the quark-gluon reaction*, JHEP **1301** (2013) 080, arXiv:1210.6832 [hep-ph].

[111] M. Czakon, P. Fiedler, and A. Mitov, *The total top quark pair production cross-section at hadron colliders through $O(\alpha_S^4)$*, Phys. Rev. Lett. **110** (2013) 252004, arXiv:1303.6254 [hep-ph].

[112] M. Czakon and A. Mitov, *Top++: A Program for the Calculation of the Top-Pair Cross-Section at Hadron Colliders*, arXiv:1112.5675 [hep-ph].

[113] J. Gao, M. Guzzi, J. Huston, H.-L. Lai, Z. Li, et al., *The CT10 NNLO Global Analysis of QCD*, arXiv:1302.6246 [hep-ph].

[114] B. Cooper, J. Katzy, M. Mangano, A. Messina, L. Mijovic, et al., *Importance of a consistent choice of alpha(s) in the matching of AlpGen and Pythia*, Eur. Phys. J. **C72** (2012) 2078, arXiv:1109.5295 [hep-ph].

[115] T. Gleisberg et al., *Event generation with SHERPA 1.1*, JHEP **0902** (2009) 007, arXiv:0811.4622 [hep-ph].

[116] S. Catani et al., *Vector boson production at hadron colliders: A Fully exclusive QCD calculation at NNLO*, Phys. Rev. Lett. **103** (2009) 082001, arXiv:0903.2120 [hep-ph].

[117] M. Bähr et al., *Herwig++ Physics and Manual*, Eur. Phys. J. **C58** (2008) 639–707, arXiv:0803.0883 [hep-ph]. 143 pages, program and additional information available from http://projects.hepforge.org/herwig.

[118] W. Beenakker, M. Krämer, T. Plehn, M. Spira, and P. M. Zerwas, *Stop production at hadron colliders*, Nucl. Phys. **B515** (1998) 3–14, arXiv:hep-ph/9710451 [hep-ph].

[119] W. Beenakker et al., *Supersymmetric top and bottom squark production at hadron colliders*, JHEP **1008** (2010) 098, arXiv:1006.4771 [hep-ph].

[120] W. Beenakker et al., *Squark and gluino hadroproduction*, Int. J. Mod. Phys. **A26** (2011) 2637–2664, arXiv:1105.1110 [hep-ph].

[121] P. M. Nadolsky, H.-L. Lai, Q.-H. Cao, J. Huston, J. Pumplin, D. Stump, W.-K. Tung, and C. P. Yuan, *Implications of CTEQ global analysis for collider observables*, Phys. Rev. **D78** (2008) 013004, arXiv:0802.0007 [hep-ph].

[122] S. Gieseke, C. Rohr, and A. Siodmok, *Colour reconnections in Herwig++*, Eur. Phys. J. **C72** (2012) 2225, arXiv:1206.0041 [hep-ph].

[123] S. Frixione and B. R. Webber, *Matching NLO QCD computations and parton shower simulations*, JHEP **06** (2002) 029, arXiv:hep-ph/0204244 [hep-ph].

[124] J. Butterworth, J. R. Forshaw, and M. Seymour, *Multiparton interactions in photoproduction at HERA*, Z. Phys. **C72** (1996) 637–646, arXiv:hep-ph/9601371 [hep-ph].

[125] B. P. Kersevan and E. Richter-Was, *The Monte Carlo event generator AcerMC version 2.0 with interfaces to PYTHIA 6.2 and HERWIG 6.5*, arXiv:hep-ph/0405247 [hep-ph].

[126] ATLAS Collaboration, *The ATLAS Simulation Infrastructure*, Eur. Phys. J. **C70** (2010) 823–874, arXiv:1005.4568 [physics.ins-det].

[127] GEANT4 Collaboration, S. Agostinelli et al., *GEANT4: A Simulation toolkit*, Nucl. Instrum. Meth. **A506** (2003) 250–303.

[128] ATLAS Collaboration, *The simulation principle and performance of the ATLAS fast calorimeter simulation FastCaloSim*, ATL-PHYS-PUB-2010-013 (2010) . https://cdsweb.cern.ch/record/1300517.

[129] G. Pasztor, R. White, F. Monticelli, M. Wielers, T. Kono, F. Zhang, F. Wang, and K. Behr, *Electron trigger performance in 2012 ATLAS data.* No. ATL-COM-DAQ-2015-091. Geneva, Jul, 2015. https://cds.cern.ch/record/2032463.

[130] ATLAS Collaboration, *Performance of the ATLAS Electron and Photon Trigger in p-p Collisions at sqrt{s} = 7 TeV in 2011.* No. ATLAS-CONF-2012-048. Geneva, May, 2012. https://cds.cern.ch/record/1450089.

[131] ATLAS Collaboration, *Measurements of normalized differential cross-sections for $t\bar{t}$ production in pp collisions at $\sqrt{s}$=7 TeV using the ATLAS detector*, Phys. Rev. D **90** (Jul, 2014) 072004. 48 p. https://cds.cern.ch/record/1712966.

[132] ATLAS Collaboration, *Search for the direct pair production of top squarks decaying to b quarks, a tau lepton, and weakly interacting particles in $\sqrt{s} = 8$ TeV pp collisions using $20fb^{-1}$ of ATLAS data.* No. ATL-CONF-2014-014. 2014.

[133] ATLAS Collaboration, *Search for direct top-squark pair production in final states with two leptons in pp collisions at $\sqrt{s} = 8$ TeV with the ATLAS detector*, JHEP **1406** (2014) 124, arXiv:1403.4853 [hep-ex].

[134] The LEP SUSY Working Group and ALEPH, DELPHI, L3, OPAL experiments, *Combined LEP selectron/smuon/stau results, 183-208 GeV*, LEPSUSYWG/04-01.1. http://lepsusy.web.cern.ch/lepsusy/www/sleptons_summer04/slep_final.html.

[135] OPAL Collaboration, G. Abbiendi et al., *Searches for gauge-mediated supersymmetry breaking topologies in e+ e- collisions at LEP2*, Eur. Phys. J. **C46** (2006) 307–341, arXiv:hep-ex/0507048 [hep-ex].

[136] ALEPH Collaboration, A. Heister et al., *Search for scalar leptons in e+ e- collisions at center-of-mass energies up to 209 GeV*, Phys. Lett. **B526** (2002) 206–220, arXiv:hep-ex/0112011 [hep-ex].

[137] DELPHI Collaboration, J. Abdallah et al., *Searches for supersymmetric particles in e+ e- collisions up to 208 GeV and interpretation of the results within the MSSM*, Eur. Phys. J. **C31** (2003) 421–479, arXiv:hep-ex/0311019 [hep-ex].

[138] L3 Collaboration, P. Achard et al., *Search for scalar leptons and scalar quarks at LEP*, Phys. Lett. **B580** (2004) 37–49, arXiv:hep-ex/0310007 [hep-ex].

[139] ATLAS Collaboration, *Search for the direct production of charginos, neutralinos and staus in final states with at least two hadronically decaying taus and missing transverse momentum in pp collisions at $\sqrt{s}$ = 8 TeV with the ATLAS detector*, J. High Energy Phys. **10** (Jul, 2014) 096. 35 p. https://cds.cern.ch/record/1712968.

[140] ATLAS Collaboration, *Search for direct top squark pair production in events with a Z boson, b-jets and missing transverse momentum in $\sqrt{s} = 8$ TeV pp collisions with the ATLAS detector*, Eur. Phys. J. **C74** (2014) 2883, arXiv:1403.5222 [hep-ex].

[141] CMS Collaboration, *Search for top squark and higgsino production using diphoton Higgs boson decays*, Phys. Rev. Lett. **112** (2014) 161802, arXiv:1312.3310 [hep-ex].

[142] CMS Collaboration, *Search for top-squark pairs decaying into Higgs or Z bosons in pp collisions at $\sqrt{s} = 8$ TeV*, Phys. Lett. **B736** (2014) 371, arXiv:1405.3886 [hep-ex].

[143] R. Brun and F. Rademakers, *ROOT - An object oriented data analysis framework*, Nucl. Inst. & Meth. in Phys. Res. A **389** (1997) no. 1-2, 81 – 86. Proceedings AIHENP'96 Workshop, Lausanne, Sep, 1996. See also http://root.cern.ch/.

[144] M. Baak, G.-I. Besjes, D. Cote, A. Koutsman, J. Lorenz, and D. Short, *HistFitter software framework for statistical data analysis*, Eur. Phys. J. **C75** (2015) 153, arXiv:1410.1280 [hep-ph].

[145] C. G. Lester and D. J. Summers, *Measuring masses of semi-invisibly decaying particles pair produced at hadron colliders*, Phys. Lett. **B463** (1999) 99–103, arXiv:hep-ph/9906349.

[146] A. Barr, C. Lester, and P. Stephens, *m(T2) : The Truth behind the glamour*, J. Phys. **G29** (2003) 2343–2363, arXiv:hep-ph/0304226.

[147] *Monte Carlo Calibration and Combination of In-situ Measurements of Jet Energy Scale, Jet Energy Resolution and Jet Mass in ATLAS.* No. ATLAS-CONF-2015-037. Geneva, Aug, 2015. https://cds.cern.ch/record/2044941.

[148] ATLAS Collaboration, *Muon reconstruction efficiency and momentum resolution of the ATLAS experiment in proton–proton collisions at* $\sqrt{s} = 7$ *TeV in 2010*, Eur. Phys. J. C **74** (Apr, 2014) 3034. 22 p. http://cds.cern.ch/record/1695792.

[149] ATLAS Collaboration, *Luminosity determination in pp collisions at* $\sqrt{s} = 8$ *TeV using the ATLAS detector at the LHC*, Eur. Phys. J. C **76** (Aug, 2016) 653. 71 p. http://cds.cern.ch/record/2208146.

[150] I. Fleck, *Signal modelling systematics at ATLAS.* No. ATL-PHYS-PROC-2013-058. Geneva, Feb, 2013. https://cds.cern.ch/record/1518738.

[151] S. Frixione, E. Laenen, P. Motylinski, B. R. Webber, and C. D. White, *Single-top hadroproduction in association with a W boson*, JHEP **0807** (2008) 029, arXiv:0805.3067 [hep-ph].

[152] T. M. P. Tait, *The* tW^- *mode of single top production*, Phys. Rev. **D61** (1999) 034001, arXiv:hep-ph/9909352 [hep-ph].

[153] ATLAS Collaboration, *Search for squarks and gluinos with the ATLAS detector in final states with jets and missing transverse momentum using $\sqrt{s} = 8$ TeV proton-proton collision data*, J. High Energy Phys. **09** (May, 2014) 176. 52 p. https://cds.cern.ch/record/1705530.

[154] ATLAS Collaboration, *Search for squarks and gluinos using final states with jets and missing transverse momentum with the ATLAS experiment in 5.8 fb^{-1} of $\sqrt{s} = 8$ TeV proton-proton collisions: support documentation.* No. ATL-PHYS-INT-2012-063. 2012. ATLAS internal report.

[155] ATLAS Collaboration, *Measurement of the cross-section for W boson production in association with b-jets in pp collisions at $\sqrt{s} = 7$ TeV with the ATLAS detector*, J. High Energy Phys. **06** (Feb, 2013) 084. 53 p. https://cds.cern.ch/record/1516003.

[156] ROOT Collaboration, K. Cranmer et al., *HistFactory: A tool for creating statistical models for use with RooFit and RooStats.* No. CERN-OPEN-2012-016. New York, Jan, 2012. https://cds.cern.ch/record/1456844.

[157] L. Moneta, K. Belasco, K. Cranmer, A. Lazzaro, D. Piparo, G. Schott, W. Verkerke, M. Wolf, K. Belasco, K. Cranmer, A. Lazzaro, D. Piparo, G. Schott, W. Verkerke, and M. Wolf, *The RooStats Project*, PoS **ACAT2010** (Sep, 2010) 057. https://cds.cern.ch/record/1289965.

[158] F. James, *Statistical Methods in Experimental Physics.* World Scientific, 2nd ed., 2006.

[159] G. Cowan, K. Cranmer, E. Gross, and O. Vitells, *Asymptotic formulae for likelihood-based tests of new physics*, Eur. Phys. J. **C71** (2011) 1554, arXiv:1007.1727 [physics.data-an].

[160] A. L. Read, *Presentation of search results: The CL(s) technique*, J. Phys. **G28** (2002) 2693–2704.

[161] The ATLAS Collaboration, The CMS Collaboration, The LHC Higgs Combination Group, *Procedure for the LHC Higgs boson search combination in Summer 2011.* No. CMS-NOTE-2011-005. ATL-PHYS-PUB-2011-11. Geneva, Aug, 2011. https://cds.cern.ch/record/1379837.

[162] ATLAS Collaboration, *Measurement of the top quark pair cross section with ATLAS in pp collisions at $\sqrt{s} = 7$ TeV using final states with an electron or a muon and a hadronically decaying τ lepton*, Phys. Lett. **B717** (2012) 89, arXiv:1205.2067 [hep-ex].

[163] CMS Collaboration, *Measurement of the $t\bar{t}$ production cross section in pp collisions at $\sqrt{s} = 8$ TeV in dilepton final states containing one τ lepton*, Phys. Lett. **B739** (2014) 23–43.

[164] ATLAS Collaboration, *Measurement of the $t\bar{t}$ production cross section in the tau+jets channel using the ATLAS detector*, Eur. Phys. J. **C73** (2013) 2328, arXiv:1211.7205 [hep-ex].

[165] CMS Collaboration, *Measurement of the top-antitop production cross section in the tau+jets channel in pp collisions at $\sqrt{s} = 7$ TeV*, Eur. Phys. J. **C73** (2013) 2386, arXiv:1301.5755 [hep-ex].

[166] D0 Collaboration, V. M. Abazov et al., *Measurement of the inclusive $t\bar{t}$ production cross section in $p\bar{p}$ collisions at $\sqrt{s} = 1.96$ TeV and determination of the top quark pole mass*, Tech. Rep. FERMILAB-PUB-16-180-E. FERMILAB-PUB-16-180-E, May, 2016. http://cds.cern.ch/record/2154713.

[167] CDF Collaboration, T. Aaltonen et al., *Measurement of the top-quark pair production cross-section in events with two leptons and bottom-quark jets using the full CDF data set*, Phys. Rev. D **88** (May, 2013) 091103. 7 p. http://cds.cern.ch/record/1545112.